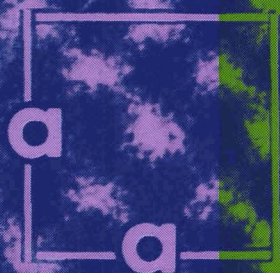# Journal of the CERAMIC SOCIETY of Japan,
International Edition
Vol.99 Mar.1991

■ 12 Papers from Nippon Seramikkusu Kyokai Gakujutsu Ronbunshi, Vol. 99 No.3 1991

Journal of Ceramic Society of Japan, *International Edition*

Vol.99 No.3
Mar. 1991

CONTENTS

Information & Communications

Papers, Letters and Notes

High resolution electron microscope photograph of the modulation doped structure of $Bi_2Sr_2CaCu_2O_y$ ($T_c=80K$) in the [100] direction. Figures at right side indicate number of copper layers, symbol B indicates bismuth rich region.
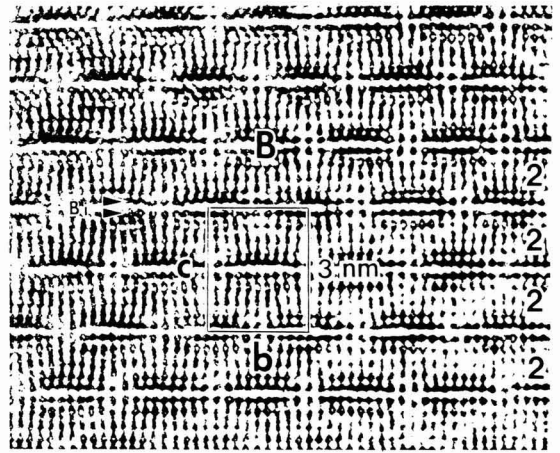
Forming of Silicon Carbide Powder by Cyclic CIP

Yohtaro Matsuo, Toshiyuki Nishimura, Kouichi Yasuda, Katsuhisa Jinbo* and Shiushichi Kimura

Department of Inorganic Materials, Faculty of Engineering, Tokyo Institute of Technology,
2-12-1 O-okayama, Meguro-ku, Tokyo 152, Japan
*Department of Mechanical Engineering for Production, Faculty of Engineering, Tokyo Institute of Technology,
2-12-1 O-okayama, Meguro-ku, Tokyo 152, Japan

Using the newly developed "Cyclic Cold Isostatic Pressing (C-CIP)" method, dry powder forming of a silicon carbide powder was studied by varying the number of cycles of pressure and maximum pressure. Green density of compacts increased as the number of cycles increased. The bending strength of pressureless-sintered SiC after C-CIP was measured. The apparent density of sintered body was independent of the number of cycles. On the other hand, the average value of the bending strength and the shape parameter of the Weibull distribution function increased.

1. Introduction

Considerable study has been done on the practical use of ceramics as a high strength material at high temperature. In these studies, the forming process is highly important in ceramic production because it has great effect on the properties of a sintered body. The most popular powder-forming process is dry uni-axial pressing. A compact made by this method is apt to have inhomogeneous packing zones as a result of friction between the die-wall and powders. Therefore, many methods have been developed to make a dense and homogeneous compact.

Boch et al. performed vibratory uni-axial pressing at 20kHz. They formed many types of ceramic powders by this method and measured the biaxial flexural strength of the sintered body. They reported that applying vibration in a low pressure range improved the structural reliability of the biaxial strength.[1]

Abe et al. formed silicon carbide powder by high pressure CIP, sintered it under a normal pressure and measured the 3 point bending strength. They reported that high pressure CIP had a positive effect in improving the shape parameter of the bending strength.[2]

The authors have developed a new powder forming technique called "Cyclic-Cold Isostatic Pressing (C-CIP)". In this procedure, hydraulic pressure is applied cyclically (see **Fig.1**). Alumina powders were formed by this method and the green density of compact increased remarkably at comparatively low pressure.[3] It was also found that the structural reliability of sintered alumina after C-CIP considerably increased.[4]

At present, silicon carbide is one candidate for a structural material feasible for practical use under high temperature. However, low sinterability originating from its tight covalent bond hinders the formation of a dense product with high structural reliability. Usually silicon carbide is made by hot pressing (HP) or hot isostatic pressing (HIP) to make a dense sintered body.[5,6] However, pressureless sintering technique by which dense sintered silicon carbide is obtained must be modified because the product shape is restricted in the HP process and large-scale machinery is needed for the HIP process. In the pressureless sintering method used, we must add sintering aids of B, C or alumina, the latter causing the decrement of high temperature strength. Also, the sintering temperature and sintering aid conditions under which dense SiC can be obtained are strictly restricted, and the structural reliability of sintered SiC is not high enough.[7-9] Therefore, if a dense and homogeneous green body can be formed, the sintering conditions will be relaxed and the structural reliability improved.

In this study silicon carbide powder, as the typical material of low sinterability, was formed by C-CIP and sintered under normal pressure. The effect of this method was discussed on the structural reliability of bending strength.

2. Experimental Procedure

2.1. SiC Powder

The silicon carbide powder used in this experiment is produced by Misui Toatsu Chemicals, Inc. This powder contains B_4C and C as sintering aids and acrylic acid ester as binder. **Figure 2** shows the SEM micrograph of the powder. **Table 1** shows the properties of powder used in this experiment.

2.2. Evaluation of Green Density

Cylindrical test pieces were used for evaluation of green density. The dimensions of the samples were $\phi 30 \times 7.5mm^3$ for C-CIP. Each sample was pre-formed by uni-axial press-
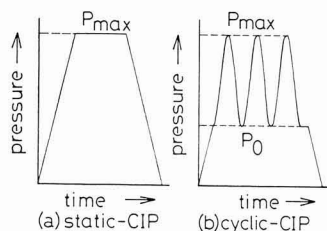

Fig. 1. Pressurizing pattern of static-CIP and C-CIP.

(a) static-CIP — P_{max}, pressure, time
(b) cyclic-CIP — P_{max}, P_0, pressure, time

ing at 10 MPa for 30 sec.

The condition of C-CIP used in the experiment was as follows:

    *Maximum pressure (P_{max}): 200 and 300 MPa
    *Bias pressure (P_O): 40% of maximum pressure
    *Frequency: 1 Hz
    *Number of cycles: 10, 100 and 1000 cycles

For comparison, static CIP was performed by following conditions.

    *Maximum pressure: 50, 100, 150, 200, 250, 300, 350
             and 400 MPa
    *Holding time at each pressure: 2 minutes

Bulk density was calculated from the weight and geometry.

2.3. Evaluation of Bending Strength

2.3.1. Forming

Test pieces were preformed by uni-axial pressing under a pressure of 10 MPa using a die which has a cross sectional area of $6 \times 50mm^2$ and then formed by C-CIP. The condition of C-CIP was as follows:

    *Maximum pressure (P_{max}): 300 MPa
    *Bias pressure (P_O): 120 MPa
    *Frequency: 1 Hz
    *Number of cycles: 1, 10, 100 and 1000 cycles

2.3.2. Sintering

After forming by C-CIP, specimens were dewaxed at 1273K for 1 hour in an argon flow. The specimens were sintered by carbon heater, making reference to the work of Tanaka et al.[8] The sintering conditions were as follows:

    *Maximum temperature: 2393 K
    *Heating speed: 10 K/min.
    *Cooling speed: 5 K/min.
    *Holding time: 1 hr. at 1673 K, 30 min. at 2393 K
    *Atmosphere: argon (over 1673 K)

2.3.3. Measurement of Bending Strength

Sintered bodies were ground by diamond wheels of #170, 400, 600 and 1000 grit size and shaped into rectangular bars of $3 \times 4 \times 40mm^3$ according to JIS 1601 standard.[10] The tensile plane was polished by diamond grit of 4μm. Apparent density was measured by the Archimedes method. Identification of crystalline phase was performed by X-ray diffractometry.

Bending strength of the above specimens was measured according to JIS 1601 standard.[10] The conditions were as follows:

    *Type of bending: 3 points
    *Span: 30mm
    *Cross head speed: 0.2mm/min.

After the bending test, the fractured surface was observed by stereoscopic microscope and SEM in order to detect the fracture origin.

2.4. Observation of Microstructure

After the specimens were polished and etched chemically, the microstructure was observed by SEM.

3. Results

3.1. Green Density

Relative green density of pre-formed compact (uni-axially pressed at 10 MPa) was about 47%.

Figure 3 shows the effect of the number of cycles on green density. The density increased as the number of cycles increased. The ratio of increment at 200 MPa decreased with the increment in the number of cycles, and that at 300 MPa was constant to the logarithm of the number of cycles.

The comparison of C-CIP with static-CIP in the relation between CIP pressure and density is shown in **Fig.4**. The data of C-CIP was at 1000 cycles. The density of statically formed compacts reached 60% at 300 MPa and did not increase any more beyond that pressure. On the other hand, the density of cyclically formed compacts reached 62% at 300 MPa. Compared at the same CIP-pressure, the density of cyclically pressed compact is 4% higher than that of
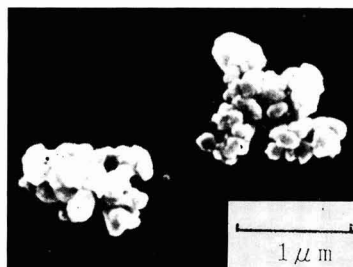
Fig. 2. SEM micrograph of SiC powder.

Table 1. Properties of powders.

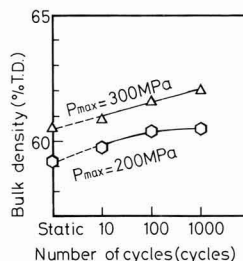|	Silicon carbide
crystal type	β
average partcle(μm) size	0.15
additives	B_4C : 0.64wt% C : 2.0wt% binder: 2.0wt%
impurities	$F-SiO_2$: 0.15% $F-C$: 0.01% Fe : 120ppm Al : 48ppm

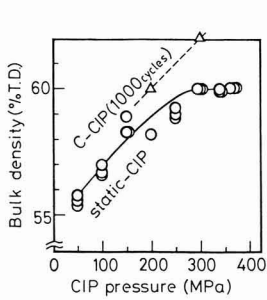**Fig. 3.** Increase in bulk density of silicon carbide compacts by C-CIP.

Fig. 4. Comparison between static-CIP and C-CIP in bulk density of silicon carbide compact.
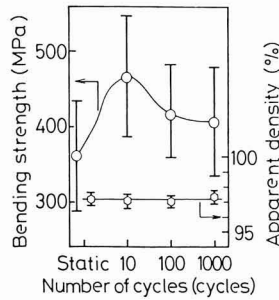
Fig. 5. Effect of the number of cycles on apparent density ( ) and bending strength (○.
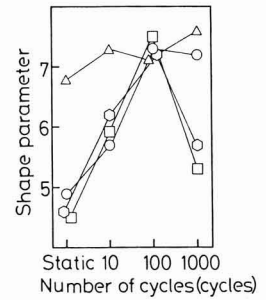
Fig. 6. Effect of the number of cycles on shape parameter.

Table 2. Physical properties of sintered silicon carbide.

Number of cycles	Type of crystal		Average apparent density (g/cm^3)
static	β	& α	3.130 ± 0.015
10	β	& α	3.125 ± 0.015
100	β	& α	3.126 ± 0.014
1000	β	& α	3.134 ± 0.014

Table 3. Result of fractography.

Number of cycles	Number of specimen			
	inner	surface	edge	total
static	14	14	1	31
10	10	15	4	31
100	11	10	6	28
1000	10	13	4	29

statically pressed compact.

3.2. Bending Strength

Physical properties of sintered specimens are shown in **Table 2**. The main phase was β-type and α-type was slightly included. At each number of cycles, the apparent density of sintered bodies was about 3.13g/cm^3, which was the typical value of the apparent density of pressureless sintered silicon carbide.

Figure 5 shows the effect of the number of cycles on the apparent density and the average value of the bending strength. The density was almost constant in each number of cycles. However, the average value of bending strength increased as the number of cycles increased, reached the maximum value at 10 cycles and then decreased slightly.

Table 3 shows the results of fractography. About 10 samples each were broken from inner defects and surface defects, and those broken from edge defects were fewer than those broken from other defects. These data were analyzed statistically by assuming that fracture occurs in accordance with 3-modal Weibull distribution function.[11,12]

Figure 6 shows the effect of the number of cycles on the shape parameter of each type of fracture origin including single mode. The shape parameter of edge defects, which were mainly induced extrinsically, did not depend on the number of cycles. The shape parameter of surface defects increased as the number of cycles increased, reached the maximum value at 100 cycles, and then decreased at 1000 cycles. In the case of inner defects, which were caused by the inhomogeneity of the compact, the effect of the number of cycles on the shape parameter indicated almost the same tendency of surface defects except that the former kept the constant value even after 100 cycles. At 100 and 1000 cycles, the shape parameter of C-CIP was 60% higher than that of static-CIP.
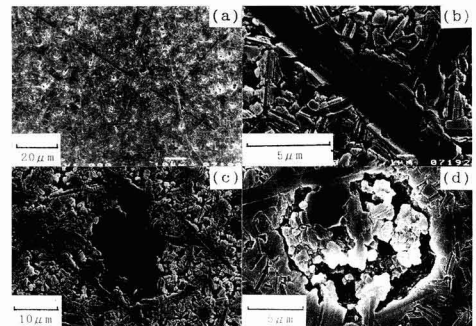
Fig. 7. Microstructures of sintered SiC.
(a). Typical microstructure of normal sintered SiC.
(b). High magnification SEM micrograph of needle-like crystal of SiC.
(c). Coalesced grain in the microstructure of SiC.
(d). Large pore in the microstructure of SiC.

3.3. Microstructure

Figures 7(a) and **(b)** show the typical microstructure of the sintered body. Intertwined needle-like crystallines almost 100µm long were observed. These needle-like crystallines were observed in each specimen.

Figure 7(c) shows the exaggerated grain growth. The coarse region where equiaxial grains are packed were observed around the exaggerated grown grain. Pores of about 10µm in diameter were also observed, and there was insufficiently sintered coarse structure in the pores (**Fig.7(d)**). This structure was observed in each specimen.

4. Discussion

4.1. Green Density

From Figs.3 and 4, we found that C-CIP has a great effect on increasing the density of SiC. In the previous work using alumina powders, no additives for forming were used. In this study, binder was added to silicon carbide powder. The density of silicon carbide compacts increased as the same manner of alumina. Thus the C-CIP has sufficient effect even with powder including binder such as in the experiment.

4.2. Bending Strength

As Fig.7 shows, the microstructure of sintered body was inhomogeneous. Needle-like crystalline and exaggerated-growth grains were observed, as were fine grains that were not sintered enough. From these observations, we cannot conclude that the silicon carbide ceramics has a well-controlled microstructure. The inhomogeneous microstructure decreased the average value of the bending strength. However, the reason why the bending strength took the maximum value at 10 cycles is not yet known.

The shape parameter of inner defect increased as shown in Fig.6. This was a result of selective removal of large pores, which were fracture origins and had a diameter of a few hundred micrometers. In the case of alumina,[4] the size of fracture origin (a pore) decreased as the number of cycles increased. The same phenomena might have occured in this experiment.

The shape parameter of surface defects increased at first and then decreased after 100 cycles. The reason for this decrement was not found because the grinding conditions were the same for all specimens.

We thus confirmed that the C-CIP procedure has a great effect on the increment of structural reliability on pressureless sintered silicon carbide. However, the average density and strength for a sintered body attained in this study were not high enough. Higher density and higher strength pressureless-sintered silicon carbide could be obtained if the conditions of C-CIP and sintering are improved.

5. Summary

Using the cyclic-cold isostatic pressing procedure, silicon carbide powder was formed. The green density increased as the number of cycles increased. The effect of the number of cycles on green density was remarkable, as the maximum pressure increased up to 300 MPa. After C-CIP, the bending strength of pressureless sintered silicon carbide was measured. The average value of bending strength and the shape parameter, which is the index of reliability, increased as the number of cycles increased.

References:
1) P. Boch and B. Rogeaux, Brit. Ceram. Proc. 38, 91-100 (1986).
2) O. Abe, S. Aoki, S. Kanzaki and H. Tabata Seramikkusu Ronbunshi 97[4] 432-38 (1989).
3) Y. Matsuo, T. Nishimura, K. Jinbo, K. Yasuda and S. Kimura, Yogyo-Kyokai-Shi 95[12] 1226-31 (1987).
4) Y. Matsuo, T. Nishimura, K. Yasuda, K. Jinbo and S. Kimura, Proceeding of MRS'88 Vol.5, 151-57 (1989).
5) H. Tanaka, Y. Inomata and H. Kawabata, Yogyo-Kyokai-Shi 88[9] 570-74 (1980).
6) Y. Takeda, T. Kosugi, S. Iijima and K. Nakayama, Proc. of International Symposium on Ceramics for Engine, Japan 529-37 (1983).
7) H. Tanaka, Y. Inomata, H. Tsukuda and A. Hagimura, Yogyo-Kyokai-Shi 92[8] 461-65 (1984).
8) H. Tanaka, Y. Inomata, K. Hara and H. Hasegawa, Journal of Material Science Letters 4 315-17 (1984).
9) N. Ohtsuka, Z. Nakagawa and K. Okada, "Seramikkusu-no-Bikohzo (Microstructure of Ceramics)" Uchida Rokakuho Publishing Co., Ltd. 94-96 (1988).
10) JIS R 1601
11) Y. Matsuo and H. Murata, Journal of the Society of Material Science Japan 33[375] 1545-51 (1984).
12) H. Murata, Y. Matsuo, M. Miyakawa and K. Kitakami, Transactions of the Japan Society of Mechanical Engineers 52[473] 27-34 (1986).

ห้องสมุดกรมวิทยาศาสตร์บริการ

Stability under Hydrothermal Conditions and Fracture Strength of Yttria- and Ceria-Doped Tetragonal Zirconia/Alumina Composites Prepared by HIP

Masanori Hirano*, Tatsuo Matsuyama*, Hiroshi Inada*, Kazutaka Suzuki** and Haruo Yoshida** and Michihide Machida**

*Noritake Co., Ltd., Noritake, Nishi-ku, Nagoya-shi, Aichi-Pref., 451 Japan
**Government Industrial Research Institute, Nagoya

Yttria- and ceria- doped tetragonal zirconia ((Y, Ce)-TZP)/Al_2O_3 composites were fabricated by HIPping at 1400°C to 1600°C and 147MPa for 0.5h in Ar, and their bending strength, microstructure and stability under hydrothermal conditions at 180°C and 1MPa were studied. The bending strength of (4Y, 4Ce)-TZP/25wt% Al_2O_3 composites HIPped at 1400°C was 1600MPa. The thermal stability of (Y, Ce)-TZP/Al_2O_3 composites increased with decreasing HIP temperature, since it depends on the HIP temperature. (4Y, 4Ce)-TZP/25wt%Al_2O_3 composites HIPped at 1400°C showed improved stability under hydrothermal conditions at 180°C and 1MPa. The composites treated at 1600°C showed marked grain growth as compared with 3Y-TZP/Al_2O_3 composites, and their bending strength was greatly reduced to less than that of normal sintered bodies. HIPping below 1500°C in Ar was useful to densify the composites and to improve the fracture strength.
[Received July 2, 1990; Accepted October 26, 1990]

1. Introduction

It is known that sintered zirconia, in which the tetragonal phase is quasi-stably maintained at room temperature, will exhibit markedly increased strength and toughness, when treated with a phase transformation reinforcement. In particular, polycrystalline tetragonal zirconia containing dissolved Y_2O_3 (Y-TZP)[1,2] can exhibit a strength of 1000MPa or more;[3] is sinterable at low temperatures; and thus is being extensively commercialized as a new structural material. On the other hand, high-pressure sintering, such as hot pressing and hot isostatic pressing (HIP), can effectively remove the residual pores and control the growth of grains formed during the low-temperature sintering process. The bending strength of 3Y-TZP increased up to 1800 to 1900MPa, when HIP-treated in studies to improve the strength of the zirconia ceramics.[4,5] A Y-TZP/Al_2O_3 composite material has exhibited a strength above 2000MPa, when HIP-treated.[6,7] It should be noted, however, that tetragonal zirconia containing Y_2O_3 as the stabilizing agent may lose its strength, when exposed in air to low temperatures between 200° to 400°C over a long period of time, due to a phase transformation from the tetragonal into the monoclinic phase.[8,9] This phase transformation is notably accelerated in the presence of steam or water,[9,12] and a variety of attempts have been made to control it.[13] The CeO_2-TZP (Ce-TZP) system has been extensively studied, based on its wider tetragonal region at high temperatures when compared to the Y_2O_3-TZP (Y-TZP) system,[14] as indicated by the phase diagram. Moreover, CeO_2 has been added to the Y-TZP system to develop a new, thermally stable composite (Y, Ce)-TZP.[15-17] These new composite systems, while exhibiting sufficient thermal stability, are lower in strength than Y-TZP. The composite of (Y, Ce)-TZP/Al_2O_3, on the other hand, has a sufficient stability under heat and hydrothermal conditions, and exhibits a strength similar to that of Y-TZP.[18]

In this study, the (Y, Ce)-TZP/ Al_2O_3 composite containing Y_2O_3 and CeO_2 as stabilizing agents was treated by HIP, to improve its strength and thermal stability. The primary focus of this study was on the preliminary sintering conditions, the relationship between the HIP temperature and the sinter strength, and the stability of the tetragonal phase under hydrothermal conditions.

2. Experimental Procedure

2.1. Specimen Preparation

Table 1 presents the specimen compositions. The composites were mixtures of powdered zirconia containing Y_2O_3 or Y_2O_3 and CeO_2 as stabilizing agents, synthesized by the hydrolysis process, and powdered α-alumina (99.99% pure, Taimei Chemical Industry Co., Ltd., TM-D), mixed in the presence of a solvent. The starting mixture was formed hydrostatically under 196MPa, after having been preformed under 19.6MPa. The compact thus prepared was presintered at 1350° to 1600°C for 2hr in air.

2.2. HIP Treatment

The presintered body, placed in a graphite crucible, was sintered in high-purity Ar gas using a test HIP apparatus

Table 1. Composition of specimens.

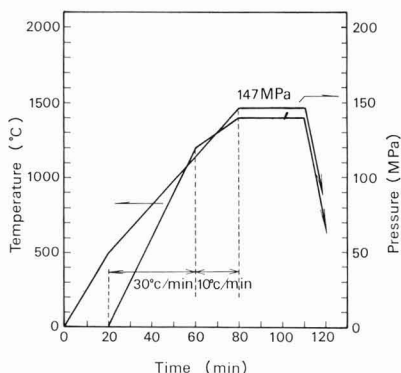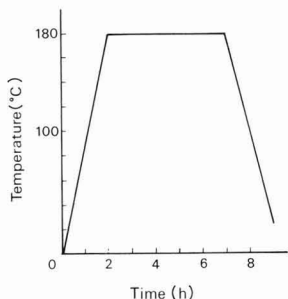| Material	Specimen	Composition		
		Co-precipitated zirconia powder		Al_2O_3 (wt%)
		Composition(mol%)	(wt%)	
Y-TZP	Y	$3Y_2O_3$, $97ZrO_2$	100	0
Y-TZP/Al_2O_3	Y25A	$3Y_2O_3$, $97ZrO_2$	75	25
(Y,Ce)-TZP/Al_2O_3	C25A	$4YO_{1.5}$, $4CeO_2$, $92ZrO_2$	75	25

Fig. 1. HIP treating schedule.

Fig. 2. Autoclave cycle.

equipped with a graphite heater. The HIP conditions were 1400°, 1500° or 1600°C, for 30 min. Each sample was heated at 30°C/min to 1200°C, and then at 10°C/min to the specified temperature. The HIP treatment schedule is given in **Fig.1**.

2.3. Analytical Procedure

The sinter density was determined by the Archimedean method. For mechanical strength measurements, each specimen was polished with a #140 diamond grindstone into a 3×4×40mm shape, which was tested by the 3-point bending method (JIS R1601) under the conditions of span: 30mm and cross-head speed: 0.5mm/min. The fracture faces of the sinter were analyzed by a scanning electron microscope (SEM, Hitachi S450) to observe the microstructures. Stability under hydrothermal conditions was determined with the specimen polished with a #140 diamond grindstone. **Figure 2** shows the test schedule; each specimen was placed in an autoclave and exposed to cycles of 180°C, 1MPa and 5hr. The autoclave processing time was the total time during which the specimen was exposed to 180°C and 1MPa. The hydrothermally treated specimen was analyzed by X-ray diffraction analysis to identify the surface phases and to analyze quantitatively the monoclinic phase using the method proposed by Garvie et al.[19]

3. Results and Discussion

3.1. Changes in Density

Figure 3 shows a parity plot of densities before and after HIP treatment, where the relative density is based on the arithmetic average of intrinsic densities of the components (3Y-TZP: 6.10g/cm³, (4Y, 4Ce)-TZP: 6.12g/cm³, and alumina: 3.98g/cm³). The presintered bodies with relative densities below 95% could not be densified to a very high extent by the HIP treatment due to the presence of residual open pores. On the other hand, those having relative densities of 95% or more were densified almost to the theoretical density level.

Figure 4 shows the effects of HIP temperature on bulk density of the Y-TZP/Al₂O₃ and (Y, Ce)-TZP/Al₂O₃ samples, each containing 25wt% of alumina. Relative densities were 96.2% and 98.5%, respectively, before the HIP treatment, and both samples were densified almost completely to the theoretical density level by treatment at 1400°C. Samples treated at 1500°C were slightly higher in density than those treated at 1400°C. The density of the HIP-treated Y-TZP/Al₂O₃ sample was relatively insensitive to HIP temperature in a range from 1400° to 1600°C. By contrast, the density of the (Y, Ce)-TZP/Al₂O₃ sample treated at 1600°C was lower than the density before treatment. The
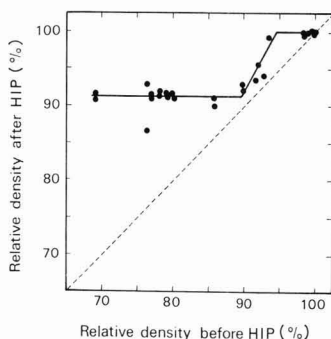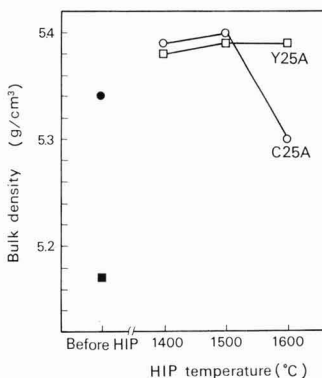

Fig. 3. Density before and after HIPping.

Fig. 4. Bulk density of TZP/Al₂O₃ composites presintered at 1400°C for 2hr, then HIPped at various temperatures for 0.5hr.

9

X-ray diffraction analysis detected the monoclinic zirconia phase in the (Y, Ce)-TZP/Al₂O₃ sample, indicating that the decreased density resulted from the formation of the monoclinic phase.

3.2. Mechanical Strength and Microstructures

Figure 5 shows the effects of HIP temperature on bending strength for the (Y, Ce)-TZP/Al₂O₃ composite containing 25wt% of Al₂O₃. The composite sintered at 1500°C in air had an average bending strength of 1050MPa. The composite HIP-treated at 1400°C, on the other hand, had a much higher strength of 1600MPa. Increasing the HIP temperature further, however, tended to decrease bending strength to 1500MPa at 1500°C and down to 600MPa at 1600°C. The sample treated at 1600°C had microcracks on its surface. Thus, increasing the HIP temperature beyond 1400°C had adverse effects on the bending strength of the (Y, Ce)-TZP/Al₂O₃ composite. This trend was not observed in the Y-TZP/Al₂O₃ composite. **Figure 6** presents the SEM photographs of the fracture surfaces of the Y-TZP/Al₂O₃ and (Y, Ce)-TZP/Al₂O₃ samples, HIP-treated at 1400°C and 1600°C. Each of these samples was pre-sintered at 1400°C. Both samples treated at 1400°C consisted of fine zirconia grains of approximately 0.5μm or less, with those of the Y-TZP/Al₂O₃ sample being slightly finer. The grains, in particular those of the (Y, Ce)-TZP/Al₂O₃ composite, grew notably when treated at 1600°C. **Figure 7** shows the effects of the pre-sintering temperature on the bending strength of the HIP-treated (Y, Ce)-TZP/Al₂O₃ composite. For the samples HIP-treated at 1400°C, the one presintered at 1400°C had widely scattered bending strengths, and those pre-sintered at 1450° to 1500°C showed the highest strength. Those composites HIP-treated at 1400° or 1500°C exhibited sufficiently high bending strengths of approximately 1500MPa, even when the pre-sintering temperature was higher than the HIP temperature. Thus, the bending strength of the HIP-treated sinter was approximately 1500MPa, when HIP-treated at 1500°C or less, and was relatively insensitive to the pre-sintering temperature in the range from 1400° to 1600°C. The bending strength was very low, around 600MPa, when the HIP temperature was 1600°C, irrespective of the pre-sintering temperature.

Each HIP-treated sinter was colored differently from the

Fig. 6. SEM photographs of the fracture surface of TZP/Al₂O3 composites.
(a) (4Y, 4Ce)-TZP/25wt%Al2O3 composites HIPped at 1400°C.
(b) (4Y, 4Ce)-TZP/25wt%Al2O3 composites HIPped at 1600C.
(c) 3Y-TZP/25wt%Al2O3 composites HIPped at 1400C.
(d) 3Y-TZP/25wt%Al2O3 composites HIPped at 1600C.
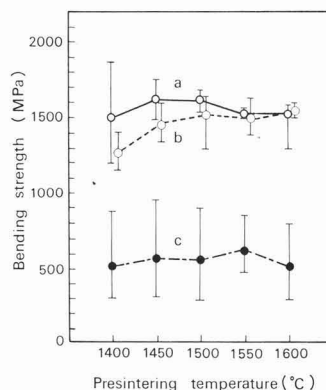
Fig. 7. Relation between bending strength and presintering temperature of (4Y, 4Ce)-TZP/25wt%Al2O3 composites fabricated by HIPping at (a) 1400C, (b) 1500C and (c) 1600C.

one sintered pressurelessly in air; gray versus white for the Y-TZP/Al₂O₃, and brown versus yellowish white for the (Y, Ce)-TZP/Al₂O₃. Masaki reported that a Y-TZP sinter prepared using an HIP apparatus equipped with a graphite heater contained a small quantity of carbon, which was oxidized when the sinter was exposed to a high temperature around 1000°C in air for a long period of time, reducing the strength.[20] The composite samples prepared in this study were HIP-treated under similar conditions; they were heated by a graphite heater while placed in a graphite crucible in an Ar gas atmosphere. One of the reasons for the color of the samples could be the contamination by small quantities of carbon as a result of the HIP treatment in a mixed (CO + Ar) atmosphere. In addition, CeO₂ used as the stabilizing agent for TZP, when exposed to high temperatures in a non-oxidative (CO + Ar) atmosphere will be gradually reduced to Ce₂O₃,[21] which would be another possible reason for the sample color. It was also observed that color of the
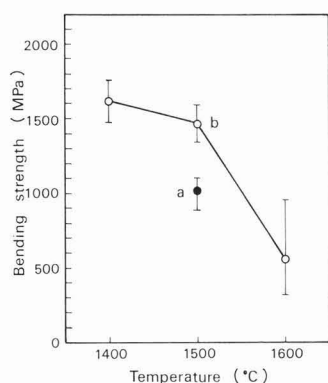

Fig. 5. Relation between bending strength and sintering temperature of (4Y, 4Ce)-TZP/25wt%Al₂O₃ composites (a) normally sintered in air and (b) presintered at 1450°C for 2hr, then HIPped for 0.5hr.
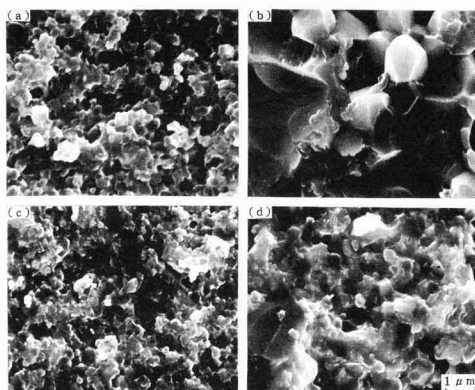
HIP-treated sinters tended to be deeper as the HIP temperature was increased. It is conceivable, judging from the extent of the coloring, that the CeO_2 contained in the (Y, Ce)-TZP/Al_2O_3 composites was reduced more quickly at 1600°C than at 1400°C.

To summarize the above experimental results, the following reasons are cited for the decreases in density and strength of the (Y, Ce)-TZP/Al_2O_3 accompanying an increase in HIP treatment temperature, as shown in Fig.5 and 7. The HIP treatment at levels as high as 1600°C in a (CO + Ar) atmosphere with a graphite heater as the heat source would (1) cause part of the CeO_2 (added as a stabilizer for TZP) to be reduced into Ce_2O_3, and (2) cause the tetragonal to monoclinic phase transformation of zirconia to be accelerated by a) the reduction of CeO_2 and by b) the grain growth, to form microcracks in the sinter.

3.3. Stability under Hydrothermal Conditions

Figure 8 presents the results of the stability tests, where each sample was exposed to the hydrothermal conditions of 180°C and 1MPa in an autoclave. The HIP-treated sintered samples containing 25wt% of Al_2O_3, prepared at 1400°C, were generally more stable under the hydrothermal conditions, with smaller quantities of the monoclinic phase produced, as compared to the Y-TZP sample pressurelessly sintered at 1500°C. Comparing Y-TZP/Al_2O_3 to (Y, Ce)-TZP/Al_2O_3, the latter was more stable, having a transformed monoclinic phase of 10% or less, when exposed to the hydrothermal conditions for 20hr. In particular, the latter was much more stable than the former after an elapse of 5hr from the time that the treatment was started. The tetragonal phase on the Y-TZP sample was almost completely transformed into the monoclinic phase, when treated in the autoclave under the hydrothermal conditions for 5 to 10hr, and it is suspected that the phase transformation spread towards the inside after 10hr, which gradually degraded the sample.

Figure 9 shows the stability, in terms of the monoclinic ZrO_2 content, of the Y-TZP/Al_2O_3 and the (Y, Ce)-TZP/Al_2O_3 samples HIP-treated at 1400°C and 1500°C and exposed to the hydrothermal conditions. The (Y, Ce)-TZP/Al_2O_3 composition was more stable than the Y-TZP/Al_2O_3, and each sample was more stable when treated at 1400°C than at 1500°C. These results indicated that the (Y, Ce)-TZP/Al_2O_3 composition had enhanced phase stability, when HIP-treated at a relatively low temperature around 1400°C.

4. Conclusions

The (4Y, 4Ce)-TZP/25wt%Al_2O_3 composite was HIP-treated at 1400° to 1500°C and 147MPa for 0.5hr, to investigate the effects of presintering and HIP conditions on the mechanical strength and stability of the sinters under hydrothermal conditions.

1) The HIP treatment produced a high-strength sinter of (Y, Ce)-TZP/Al_2O_3, exhibiting a bending strength of 1600MPa.
2) The (Y, Ce)-TZP/Al_2O_3 sample HIP-treated at 1400°C had a widely varying bending strength, when presintered at 1400°C. It had the highest average strength, when presintered at 1450° to 1500°C.
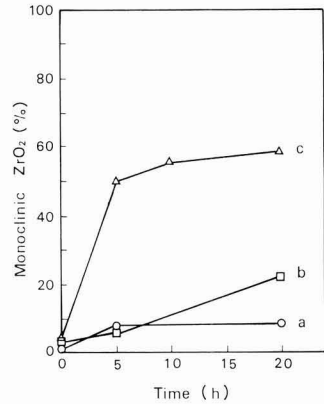
Fig. 8. Results of hydrothermal aging at 180°C and 1MP for (a) (4Y, 4Ce)-TZP/25wt%Al_2O_3 and (b) 3Y-TZP/25wt%Al_2O_3 composites fabricated by HIPping at 1400°C and (c) 3Y-TZP fabricated by normal sintering at 1500°C.
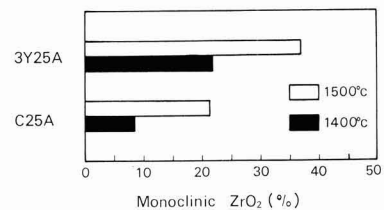
Fig. 9. Tetragonal-to-monoclinic phase transformation resulting from hydrothermal aging at 180C and 1MPa for 20hr for 3Y-TZP/25wt%Al_2O_3 and (4Y, 4Ce)-TZP/25wt%Al_2O_3 composites fabricated by HIPping at 1400°C and 1500°C.

3) The samples HIP-treated at 1400°C were more stable under the hydrothermal conditions than those prepared at a higher temperature, and the (Y, Ce)-TZP/Al_2O_3 composite HIP-treated at 1400°C showed little tetragonal to monoclinic phase transformation.
4) The (Y, Ce)-TZP/Al_2O_3 composite HIP-treated at 1600°C had a greatly reduced bending strength of 600MPa, and its grains were notably large as compared with those of the Y-TZP/Al_2O_3 composite HIP-treated under the same conditions.

References:
1) T. K. Guputa, J. H. Bechtold, R. C. Kuznicki, L. H. Cadoff, and B. R. Rossing, J. Mater. Sci., 12, 2421-26 (1977).
2) T. K. Guputa, F. F. Lange, and J. H. Bechtold, J. Mater. Sci., 13, 1464-70 (1978).
3) K. Tsukuma, Y. Kubota, and T. Tsukidate, Yogyo Kyokai-shi, 92, 11-19 (1984).
4) K. Tsukuma and M. Shimada, Am. Ceram. Soc. Bull., 64, 310-13 (1985).
5) T. Tatsuno and K. Honma, "Zirconia Ceramics, Part 5 " Uchida Rokaku-ho, (1985) pp.27-30.
6) K. Tsukuma, K. Ueda and M. Shimada, J. Am. Ceram. Soc., 68, c-5 (1985).
7) R. Shiho, Y. Urata, T. Shiono, and T. Nishikawa, Powder and Powder

Metallurgy, 37, 357-61 (1990).

8) K. Kobayashi, H. Kuwajima, and T. Masaki, Solid State Ion., 3-4, 489 (1981).

9) T. Sato, S. Ohtaki, and M. Shimada, J. Mater. Sci., 20, 1466-70 (1985).

10) T. Sato and M. Shimada, J. Am. Ceram. Soc., 68, 356-59 (1985).

11) M. Yoshimura, T. Noma, K. Kawabata, and S. Somiya, Seramikkusu Ronbunshi, 96, 265-70 (1988).

12) T. Shigematsu and N. Nakanishi, "Zirconia Ceramics, Part 9" Uchida Rokaku-ho, (1987) pp. 63-71.

13) T. Sato and M. Shimada, Hyomen Kagaku, 10, 11-17 (1989).

14) K. Tsukuma, Am. Ceram. Soc. Bull., 65, 1386-89 (1986).

15) T. Watanabe, K. Urabe, H. Igawa, and S. Utagawa, Ceramic Society of Japan Annual Meeting Proceedings, (1984), pp.463-64.

16) T. Sato, S. Ohtaki, T. Endoh, and M. Shimada, "Zirconia Ceramics,

Part 5," Uchida Rokaku-ho, (1985) pp.75-85.

17) M. Hirano and H. Inada, Seramikkusu Ronbun-shi, 99, 23-29 (1981).

18) M. Hirano and H. Inada, Seramikkusu Ronbun-shi 99, 124-130 (1991).

19) R. C. Garvie, and P. S. Nickolson, J. Am. Ceram. Soc., 55, 303 (1972).

20) T. Masaki, J. Am. Ceram. Soc., 69, 519-22 (1986).

21) K. H. Heussner and N. Claussen, J. Am. Ceram. Soc., 72, 1044-46 (1989).

Hydroxyapatite Ceramics with Tetragonal Zirconia Particle Dispersion Prepared by HIP Post-sintering

Koji Ioku*, Shigeyuki Somiya** and Masahiro Yoshimura

Research Laboratory of Engineering Materials, Tokyo Institute of Technology
4259, Nagatsuta, Midori-ku, Yokohama-shi 227, Japan,
* Now with Kochi University, ** Now with the Nishi Tokyo University

Hydroxyapatite (HAp) powders with dispersed tetragonal zirconia particles were synthesized hydrothermally at 200°C under 2MPa for 10h. Transmission electron microscopy (TEM) demonstrated that the homogeneous mixture of ultra-fine HAp single crystals and zirconia particles could be obtained by the hydrothermal technique. The mixture with the volume ratio of HAp: zirconia=90:10 was hot-pressed at 1050°C under 30MPa for 1h in Ar, then post-sintered by HIP at the same temperature under 200MPa of Ar for 1h. The product had almost pore free microstructures consisting of HAp matrix and tetragonal zirconia particles. Its fracture toughness was 2.5 times as large as that of the transparent pure HAp ceramics. This ceramic was toughened by the crack deflection toughening mechanism and probably by the transformation toughening mechanism due to tetragonal zirconia particles dispersed in the matrix. Furthermore, the reactivity between HAp and zirconia was examined. The decomposition of HAp to β-tricalcium phosphate (β-TCP) was accelerated by zirconia, and CaO was not detected in every temperature. Thus the decomposition was taken place by dissolution of Ca components in zirconia in the first step, then HAp decomposed to β-TCP subsequently.
[Received July 16, 1990; Accepted December 14, 1990]

1. Introduction

Hydroxyapatite ($Ca_{10}(PO_4)_6(OH)_2$, HAp) has been rigorously investigated for possible use as dental roots and as a substitute material for bones because of its excellent compatibility with human tissue. Although HAp ceramics have a sufficient compressive strength for use as artificial bone materials,[1] the sintered bodies compacted to transparency[2] only have fracture toughness values K_{IC} around 1.1MPa·m$^{1/2}$,[3] which restricts their use as biomaterials. It is therefore necessary to enhance the mechanical properties, especially the fracture toughness, of HAp ceramics. It has been shown that complexing the HAp ceramic with metastable tetragonal zirconia particles or the like is effective in enhancing the fracture toughness,[4-10] with numerous efforts having been reported with respect to the ZrO_2-HAp composite systems.[11-18]

As described in these studies, tetragonal ZrO_2 particles react with HAp in the sintering process to yield cubic ZrO_2, with the HAp decomposing to tricalcium phosphate ($Ca_3(PO_4)_2$, TCP). For this reason, HAp ceramics with dispersed tetragonal ZrO_2 particles have yet to produce the decomposition product, TCP. Furthermore, a volume ratio of ZrO_2 particles as high as 30 to 50vol% has been added in most of the previous studies, which considerably reduces the bioactivity of the complex as compared to pure HAp.

To increase the toughness of the ceramics in this system without decreasing the bioactivity, it is necessary (1) to keep the addition of ZrO_2 particles to a minimum, (2) to prevent the decomposition of HAp by lowering the sintering temperature, and (3) to produce dense composite ceramics. In addition, ZrO_2 particles must be homogeneously dispersed into the HAp matrix, thus heterogeneous dispersions produced by the mechanical mixing of ZrO_2 and HAp powders are not suitable.

In this experiment, a method to hydrothermally synthesize ultra-fine HAp single crystals was explored,[19] and a process to prepare homogeneous mixtures of tetragonal ZrO_2 particles and HAp particle, was studied in an attempt to prepare ZrO_2-HAp composite ceramics with high toughness and without the decomposition of HAp. Two sizes of ZrO_2 particles were used to investigate the effects of ZrO_2 particle size on the change in crystalline phase during heating.

2. Experimental Method

2.1. Tetragonal ZrO_2 Particles

Zirconia containing 3mol% Y_2O_3[20] was selected as the zirconia particles to be dispersed into the matrix of HAp in our attempts to achieve high toughness. Small-size ZrO_2 particles were hydrothermally synthesized by the following method: a mixed solution of $ZrOCl_2$ and $Y(NO_3)_3$ was added to excess ammonia water, and the coprecipitated gel thus obtained was hydrothermally crystallized at 200°C under 2MPa for 24 hours to form ZrO_2 particles[21] (hereinafter called 3YZ). For large-size ZrO_2 particles, commercially available zirconia containing 3mol% Y_2O_3 was used (hereinafter called TZ3Y, manufactured by Tosoh Corporation).

2.2. Hydrothermal Synthesis of ZrO_2-HAp Composite Powders

Mixed powders with HAp:ZrO_2 volume ratios of 90:10 were added to an aqueous solution of 0.167M $Ca(NO_3)_2$ (guaranteed reagent, Wako Pure Chemical Industries, Ltd.) suspended. The pH of solution was adjusted to pH10 with ammonia water, and an aqueous solution of 0.1M $(NH_4)_2HPO_4$ (guaranteed reagent, Wako Pure Chemical In-

dustries, Ltd.) adjusted to pH10 with ammonia water was added to yield a ZrO_2-HAp precipitate. This precipitate was agitated in pH10 ammonia water and hydrothermally crystallized at 200°C under 2MPa for 10 hours in an autoclave. A flow chart of the synthetic process is shown in Fig.1. The obtained composite powders (3YZ + HAp and TZ3Y + HAp) were rinsed with Nessler's reagent until ammonia water was no longer detected, and then dried at 60°C in air.

2.3. Compacting and Sintering

The composite powders were compacted by hand into a bakelite mold. The pellet was gassed by placing it in a rubber bag, and then pressing by CIP under 200MPa for 5 minutes. The pellet was allowed to dry at 60°C for 24 hours, and then heated at a rate of 10°C/min to 800° to 1300°C and sintered in air for a specified period of time.

In the HA sintering experiment, a 1g sample was placed into a graphite mold (10mm inside diameter, 30mm high), and subjected to pressure of 30MPa before being heated to 900° to 1200°C at a heating rate of about 5°C/min in an Ar gas atmosphere for 1 hour. After sintering at a prescribed temperature, the pressure was reduced to zero, and the sample was allowed to cool in the furnace. To increase the compactness of the sintered body, post-sintering by HIP (Dr. HIP manufactured by Kobe Steel, Ltd.)[2] was performed on the HP sintered bodies at 1050°C under 200MPa pressure for 1 hour in an Ar atmosphere.

2.4. Evaluation of Characteristics of Powders and Sintered Compacts

The shape and mixing conditions of particles were observed with a transmission electron microscope (H-800, Hitachi, Ltd.) at an acceleration voltage of 200kV. The particle size was determined from TEM photographs by averaging 250 particles. Powder X-ray diffractometry (XRD) (RU-200, Rigaku Corporation) was employed to identify the phases and to determine the lattice constants and apparent crystal size, using CuKα rays and a carbon monochrometer at an applied voltage of 40kV and a tube current of 80mA. Lattice constants and apparent crystallite sizes were determined using the method of least squares at a 1/4°/min scanning rate and a 5 second time constant, and

the angle of diffraction line was corrected based on the Si lattice constant, a=5.4301, using Si metal (Metal Science Research Institute, 99.99%) as the internal standard. The apparent crystal size was calculated from the diffraction line width at half-maximum using Scherrer's equation.[22] The change in the crystalline phase due to heating was determined from the integrated intensity of typical diffraction lines of HAp:2θ=31.8°, α-TCP:2θ=30.7°, β-TCP:2θ=31.0°, and ZrO_2:2θ=30.5° (cubic and tetragonal). The sinterability of the starting material was determined at a heating rate of 10°C/min in air by using a thermal expansion meter (high-temperature type TMA, Rigaku Corporation).

The bulk density of the sintered compact was measured by the Archimedean method using mercury as a solvent. The relative density was calculated based on a sinter density $(3.45g/cm^3)$ determined from the theoretical densities of ZrO_2 containing 3mol% Y_2O_3 $(6.05g/cm^3)$ and HAp $(3.16g/cm^3)$, and the volume ratio $(ZrO_2:HAp = 10:90)$. The crystalline phase of ZrO_2 particles in the sintered compact was identified by measuring the Raman spectrum (U-1000, Ramanor) from the excitation wavelength of 4880Å of an argon ion (Ar^+) laser. The microstructure of the sintered compact was observed with a scanning electron microscope (SEM) (JSM-T200, JEOL Ltd.). The sample surface was also observed after the thermal etching of the polished sinter at a temperature 10°C below the sintering temperature for 10 minutes. The mechanical properties of the sintered compact were evaluated by measuring the Vickers hardness (Hv) and the fracture toughness (K_{IC}). The Vickers hardness was determined by measuring the size of the indentation made by placing the indenter onto the mirror polished surface of a sintered compact and applying a 2.94N load for 30 seconds. The fracture toughness was determined by the microindentation fracture method (IM) using Niihara's equation.[23] A 2.94N load was applied for 30 seconds, producing a median crack (mc).

3. Results and Discussion

3.1. Properties of ZrO_2-HAp Composite Powders

The TEM observation revealed that 3YZ particles were microcrystalline polyhedra with an average particle size of 7nm, with almost no aggregation found between the particles. The TZ3Y particles were also polyhedric, but had an average particle size of 70nm; furthermore, the neck that seemed to form during calcination was not found between these particles. The secondary particles formed as a result of aggregation were about 1μm across. The precise measurement by XRD showed that the lattice volumes of 3YZ and TZ3Y were 134.28±0.08Å³ and 134.38±0.08Å³, respectively; in addition the Y_2O_3 concentrations[24] determined from the lattice volumes were 2.9±0.3mol% and 3.3±0.3mol%. The XRD of 3YZ+HAp powders and TZ3Y+HAp powders contained the diffraction lines for ZrO_2 and HAp, with no other compounds detected. A comparison of the lattice constants of pure 3YZ and pure HAp[19] with those in the 3YZ+HAp powder showed that the 3YZ and the HAp did not react. It was similarly confirmed that the TZ3Y and the HAp did not react in the TZ3Y+HAp powder. The properties of the powders are listed in Table 1. The TEM observation revealed that independent of the particle size, the polyhedral ZrO_2 particles and the
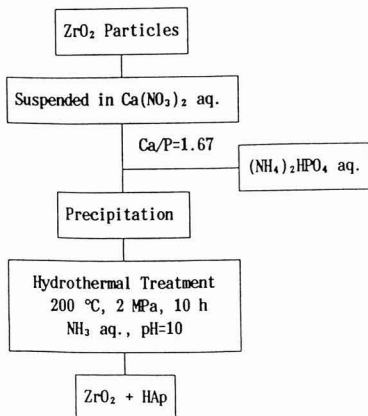

Fig. 1. Hydrothermal preparation of hydroxyapatite powders with zirconia particles dispersion.

Table 1. Lattice parameters and crystallite sizes of hydroxyapatite powders with dispersed zirconia particles synthesized hydrothermally at 200°C, under 2 MPa for 10 h.

| | Lattice Parameters $(10^{-1} nm)$ | | Crystallite Sizes from XRD (nm) | | |
| | | | ZrO_2 | HAp | |
	ZrO_2	HAp	D_{111}	D_{002}	D_{300}
3YZ +HAp	$a=5.121\pm0.003$ (Pseudo-Cubic)	$a=9.419\pm0.002$ $c=6.880\pm0.001$ (Hexagonal)	8.6 ± 2.0	25.3 ± 2.5	80.9 ± 10.0
TZ3Y +HAp	$a=5.095\pm0.002$ $c=5.177\pm0.001$ (Tetragonal)	$a=9.418\pm0.002$ $c=6.879\pm0.001$ (Hexagonal)	117.5 ± 15.0	26.1 ± 3.0	81.5 ± 10.5
Pure HAp[9]	——	$a=9.420\pm0.001$ $c=6.880\pm0.001$ (Hexagonal)	——	——	——

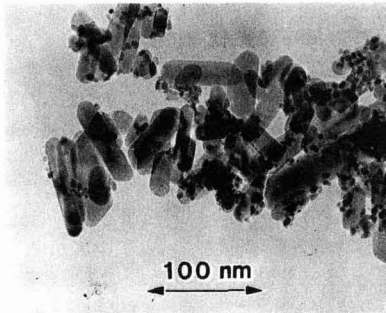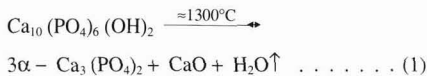Chemical formula of HAp: $Ca_{10}(PO_4)_6(OH)_2$

Fig. 2. TEM observation of 3YZ+HAp powders synthesized hydrothermally at 200°C under 2.0MPa for 10h.

hexagonal ultra-fine HAp crystals were homogeneously dispersed when hydrothermally prepared (**Fig.2** and **Fig.3-(a)**). For powders prepared by the mechanical mixing of TZ3Y and HAp for 3 hours in methanol using an agate mortar, the TEM observation (**Fig.3-(b)**) revealed that the TZ3Y particles clearly aggregated; thus the agitation during the hydrothermal technique was more effective in producing a homogeneous dispersion.

3.2. Phase Change of ZrO₂-HAp Composite Powders Due to Heating

Changes in the crystalline phase due to heating were investigated to understand the sintering behavior of the composite powders. It is known that pure HAp generally decomposes to α-TCP, CaO, and H₂O when heated to about 1300°C.[25]

$$Ca_{10}(PO_4)_6(OH)_2 \xrightarrow{\approx 1300°C}$$
$$3\alpha - Ca_3(PO_4)_2 + CaO + H_2O\uparrow \quad \ldots \ldots (1)$$

In 3YZ+HAp powders, HAp begins to decompose into β-TCP at a lower temperature around 800°C, and the yield of TCP increases with an increase in the heating temperature (Fig.4-(a)). This fact suggests that the decomposition of HAp is accelerated by ZrO₂. Since the XRD results did not detect any CaO in the heated 3YZ+HAp powder, a decomposition reaction different from Eq.(1) may take place. The lattice volume of ZrO₂ in the heated sample slightly in-
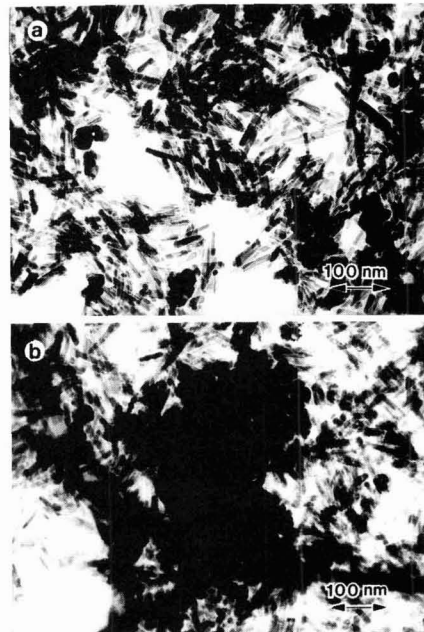
Fig. 3. TEM photographs of TZ3Y+HAp powders synthesized hydrothermally at 200°C under 2.0MPa for 10h (a), and TZ3Y+HAp powders prepared by solid-solid mixing (b).

creased at 800°C and significantly increased above 900°C (**Fig.5**). The lack of CaO formation also suggested that Ca components in the HAp particles were first transferred to ZrO₂ particles, which prevented the HAp from attaining an apatite structure (hexagonal, $P6_3/m$),[26] and instead yielded β-TCP (trigonal, $R3_c$)[27] by partial dehydration. In fact, cubic ZrO₂ increased while tetragonal ZrO₂ decreased when the sample was heated to 800°C or above, and only tetragonal ZrO₂ existed when the sample was heated to 1100°C or above. The lattice constant of tetragonal ZrO₂ was a=5.133±0.001Å at 1100°C. This system consisted of Y₂O₃-CaO-ZrO₂ as expected. Based on the lattice constant of CaO stabilized ZrO₂,[28,29] the content of CaO was calculated as 7.8mol%, but the actual value may have been less
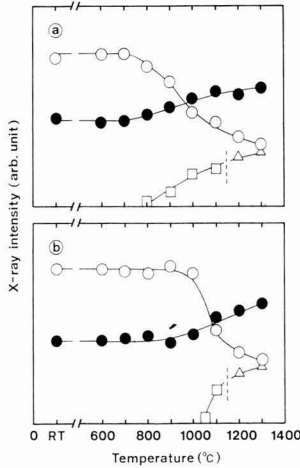
Fig. 4. Phase changes of 3YZ+HAp powders (a), and TZ3Y+HAp powders (b) heated at indicated temperatures for 3h.○ HAp, ● ZrO₂, ☐β-TCP, △α-TCP.

Fig. 5. Unit cell volume of zirconia in 3YZ+HAp powder compacts (○) and TZ3Y+HAp powder compacts (●) heated at indicated temperatures for 3h in air.

since the sample contained 3mol% Y_2O_3. The β-TCP produced by the decomposition of HAp was transformed into α-TCP (monoclinic, P2₁/a), having a stable phase at 1180° to 1430°C, by heating at 1200°C for 3 hours.[30] Based upon the above discussion, the decomposition of 3YZ+HAp powders by heating and the transformation of TCP can be expressed by Eqs. (2) and (3), respectively.

$$Y - ZrO_2 \text{ (Tet.)} + Ca_{10}(PO_4)_6(OH)_2 \xrightarrow{\approx 800°C}$$

$$Ca - Y - \text{doped } ZrO_2 \text{ (Cubic)} + 3\beta - Ca_3(PO_4)_2 + H_2O\uparrow$$

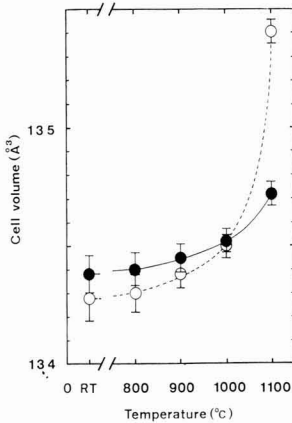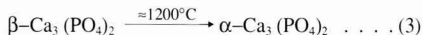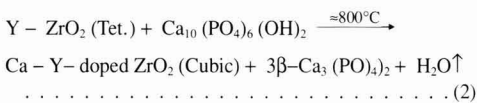$$\cdots\cdots\cdots\cdots\cdots\cdots\cdots\cdots\cdots (2)$$

$$\beta - Ca_3(PO_4)_2 \xrightarrow{\approx 1200°C} \alpha - Ca_3(PO_4)_2 \quad \cdots (3)$$

For the TZ3Y+HAp powder, it was verified that the reaction between TZ3Y and HAp began at 800°C as with the 3YZ+HAp powder, since the lattice volume increased at a calcining temperature of 800°C or above. The lattice volume of ZrO_2, however, increased more slowly compared to the ZrO_2 in the 3YZ+HAp powder (Fig.5). Therefore, the reaction proceeded slowly and the formation of β-TCP due to the decomposition of HAp was not evident at 800°C (**Fig.4-(b)**). Based on the X-ray diffraction results, β-TCP was first evident in the sample heated for 3 hours at 1050°C, about 250°C higher than the temperature at which the ZrO_2+HAp reaction took place. The fact that TCP was not formed at 800°C when the ZrO_2+HAp reaction began can be explained as follows: Since HPa can have an apatite structure even if the Ca content is below the stoichiometric quantity (Ca deficient apatite), the decomposition product TCP will only be formed when a certain amount of Ca components are released from the HAp and transferred to the ZrO_2 particles. The more contact points that exist between the ZrO_2 particles and the HAp particles, the larger the amount of Ca components that are transferred from HAp to ZrO_2, and TCP can be formed at a lower temperature (≥800°C). Conversely, when there are only a few contact points, a higher temperature or a longer period of time is needed to form TCP. Since TZ3Y+HAp powders, like 3YZ+HAp powders, contain homogeneously mixed ZrO_2 particles and ultra-fine HAp crystals, the difference in temperatures at which TCP is formed will depend upon the size of ZrO_2 particles and the reactivity of the particle surface. If the volume ratio of ZrO_2 particles to ultra-fine HAp crystals is equal to 1, the number of HAp contact points (reaction start points) increased as the particle size of ZrO_2 decreases (as in the 3YZ+HPa powders in **Fig.6-(a)**), and the temperature at which TCP is formed decreases because the reactivity on the ZrO_2 particle surface is enhanced. Conversely, as the particle size of ZrO_2 increases, the number of contact points with HAp decreases (as in the TZ3Y+HAp powders in **Fig.6-(b)**), and the reactivity of the ZrO_2 particle surface is lowered. Therefore, the temperature at which TCP is formed should rise. For this reason, the yield of TCP is thought to be proportional to the transferred amount of Ca components, and the increase in lattice volume of ZrO_2 can be estimated from Eq.(4) and its relationship to the yield of β-TCP can be determined.

$$\Delta V = V_{HT} - V_{RT} \quad \cdots\cdots\cdots\cdots\cdots (4)$$
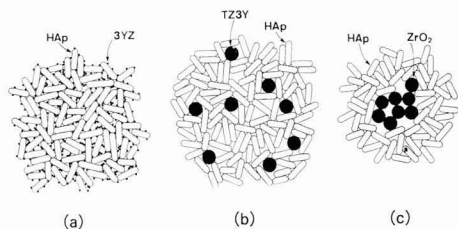
Fig. 6. Schematic illustration of several types of ZrO₂+HAp powders. (a) homogeneous dispersion between smaller zirconia particles and hydroxyapatite particles (corresponding to 3YZ+HAp powders prepared hydrothermally), (b) homogeneous dispersion between larger zirconia particles and hydroxyapatite particles (corresponding to TZ3Y+HAp powders prepared hydrothermally), and (c) inhomogeneous dispersion between larger zirconia particles and hydroxyapatite particles (corresponding to TZ3Y+HAp powders prepared by solid-solid mixing).
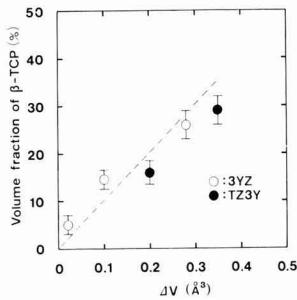
Fig. 7. Relationship between volume fraction of β-TCP and increments of cell volume for zirconia as ΔV in the reaction during sintering of ZrO_2+HAp

where, ΔV is the increase in the lattice volume; V_{HT} is the lattice volume at the heating temperature, and V_{RT} is the lattice volume at room temperature prior to the reaction (V_{RT} = 134.28Å^3 for 3YZ, and V_{RT} = 134.38Å^3 for TZ3Y). A linear relationship was observed between the change in the lattice volume of ZrO_2 (ΔV) obtained from Eq.(4) and the yield of β-TCP for the 3YZ+HAp and TZ3Y+HAp samples (**Fig.7**). Although β-TCP was only formed at temperatures above 800°C, it was observed that the yield depended on the transfer amount of Ca components, not on the temperature. It can be concluded that the β-TCP yield depends on (1) the volume ratio of ZrO_2 particles, (2) the particle size of ZrO_2, (3) the particle size of HAp, and (4) the mixing conditions of ZrO_2 and HAp particles.

According to published reports,[11-15] a change in the crystalline phase due to heating of the ZrO_2-HAp system takes place as follows. First, the HAp decomposes into TCP, CaO, and H_2O, and then the CaO dissolves into the ZrO_2, forming cubic ZrO_2. However, CaO, which should exist as a decomposition product, was not at all detected in the heated samples in this study. It is therefore reasonable to believe that the decomposition of this system takes place as follows. First, the mass transfer of Ca components from HAp to ZrO_2 takes place as described above, and as a result TCP is formed from Hap. The decomposition of HAp (the formation of TCP) has been reported to take place first at a temperature above 1150°C, though not strictly the same temperature, and this temperature is regarded as the temperature at which the reaction starts.[11-15] In the previous study, the reaction between ZrO_2 and HAp started at 800°C by the above-described reaction mechanism. However, in this study, it was thought that the temperature at which TCP was formed was 1150°C, about 350°C higher than the temperature at which the reaction started. The reason why the formation temperature of β-TCP in the current study was higher than that observed for the 3YZ+HAp and TZ3Y+HAp powders (800°C and 1050°C respectively) in the previous studies, is perhaps explained by the following. The transfer amount of Ca components was small as compared with the 3YZ+HAp or TZ3Y+HAp powders at the same temperature and for the same period of time because the particle size of ZrO_2, the starting material, was considerably larger than that of 3YZ and reduced the number of contact points with HAp to decrease the reactivity of particles. Moreover, the ZrO_2-HAp powders in the published reports[11-15] were prepared by mechanical mixing, which might have produced an aggregation of ZrO_2 particles. In

that case, the number of contacts between the ZrO_2 particles and the HAp particles would further decrease (**Fig.6-(c)**). Therefore, the formation temperature of TCP may have increased.

From the above discussion, it can be concluded that the temperature at which the reaction between ZrO_2 and HAp starts should be distinguished from the temperature at which TCP is formed; furthermore, the reaction does not take place at a temperature as high as 1150°C, but at about 800°C, a temperature lower than the formation temperature of β-TCP. Also, it is reasonable to assume that the formation temperature of TCP depends on the volume ratio of ZrO_2 particles to HAp crystals, on the particle size of ZrO_2 and HAp particles, and on the mixing conditions.

3.3. Sinterability of ZrO_2-HAp Composite Powders and Mechanical Properties of Composite Ceramics

As described earlier, 3YZ+HAp powders exhibit a high level of reactivity between 3YZ and HAp; tetragonal ZrO_2 becomes cubic in the sintering process, and part of the HAp decomposes to form β-TCP. On the other hand, TZ3Y+HAp powders exhibit a lower level of reactivity than the 3YZ+HAp powders. In both cases, ZrO_2 particles can be dispersed into the HAp matrix since it is cubic.

Measurements with a thermal expansion meter showed that the TZ3Y+HAp powders have a lower sinterability than HAp alone (**Fig.8**). The temperature at which contraction starts in TZ3Y+HAp was about 100°C higher than that for HAp alone, and the coefficient of contraction at 1300°C was as low as 10%. Since the sintering start temperature of TZ3Y is higher than that of HAp, the degree of densification depends mainly on the gap between HAp particles. TZ3Y particles disturb the contacts between HAp particles; thus, large voids remain between the TZ3Y and HAp particles even though the densification of the HAp particles proceeds. It is therefore assumed that the bulk densification of TZ3Y+HAp begins at a higher temperature than that for Hap alone, and the amount of contraction due to the temperature increase is small. The reaction between TZ3Y and HAp described in the preceding section may disturb the densification. In fact, the measurement of bulk density of compacts sintered under normal pressure at 900° to 1300°C for 3 hours showed that TZ3Y+HAp had been densified only to a relative density of about 70% (**Fig.9**).

Because TZ3Y+HAp powders were densified only to a relative density of about 70% by sintering under normal pressure, hot pressing (HP) was performed and the densified
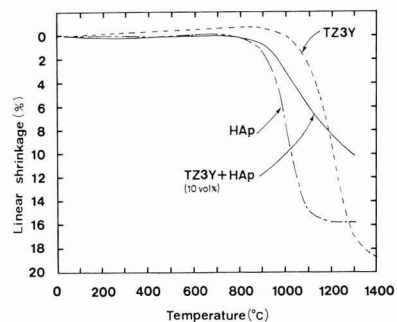

Fig. 8. Densification of TZ3Y+HAp compact CIP'ed under 200MPa (heating rate: 10°C/min).
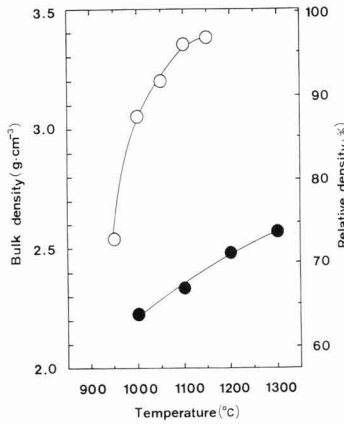
Fig. 9. Density of hydroxyapatite ceramics with TZ3Y particles dispersion; ○ sintered by HP at indicated temperatures under 30MPa for 1h in Ar, and ● sintered normally at indicated temperatures for 3h.
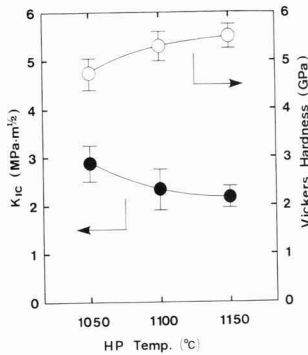

Fig. 10. Mechanical properties of the hot-pressed TZ3Y+HAp ceramics at indicated temperatures under 30MPa for 1h in Ar. ○ Vickers hardness, and ● fracture toughness $K_{I}C$.

sample was post-sintered. HP was proven to be effective in densifying TZ3Y+HAp powders (Fig.9); TZ3Y+HAp powders were densified to 3.20g/cm³ (92.8%) at 1050°C. If hot pressed for 3 hours, the reaction between TZ3Y and HAp began at 1050°C; however, after only 1 hour of HP, β-TCP could not be detected by XRD, and the ZrO₂ particles remained tetragonal. By HP at 1150°C, TZ3Y+HAp reached a maximum bulk density of 3.35g/cm³ (97.1%); β-TCP was found in the sample, and the formation of cubic ZrO₂ particles was noted. At HP temperatures between 1050° to 1150°C, an increase in the Vickers hardness due to densification was observed with an increase in sintering temperature, but K_{IC} decreased with an increase in sintering temperature (**Fig.10**). The decrease in K_{IC} may have been caused by an increase in the quantity of tetragonal ZrO₂; that is, a decrease in the amount of cubic ZrO₂ contributed to increased transformation toughness. Therefore, it is ex-

pected that HAp ceramics with dispersed tetragonal ZrO₂ particles prepared at a temperature at which tetragonal ZrO₂ is not changed to cubic by the reaction between ZrO₂ and HAp have the highest toughness values.

To prepare HAp ceramics with dispersed tetragonal ZrO₂ particles, post-sintering was performed on compacts hot-pressed at 1050°C under 30MPa for 1 hour; the reaction between ZrO₂ and HAp was not observed. Post-sintering, HIP at 1050°C under 200MPa for 1 hour, provided high densification with the bulk density reaching 3.40g/cm³ (98.6%). SEM observation detected almost no pores, and the reflection electron image (**Fig.11**) indicated ZrO₂ as white particles measuring 0.5μm to 5μm across. In the XRD measurement of the polished surface of the sintered compact, only tetragonal ZrO₂ and HAp were observed, cubic ZrO₂ and β-TCP were not found. Regarding the mechanical properties of this sintered compact, the Vickers hardness (Hv) was 5.5GPa, and its fracture toughness (K_{IC}) was 2.8MPa·m$^{1/2}$ (**Table 2**). The Vickers hardness was nearly the same as that of dense sintered compacts of HAp alone, but the K_{IC} was about 2.5 times that for HAp dense sintered compacts, and about 2.3 to 4 times the K_{IC} value of dense compacts of HAp from published reports.[31,32] The comparison of K_{IC} values, however, should be made carefully because the fracture toughness is sensitive to the method and condition of measurement. Since the SEM observations revealed crack deflection from Vickers indentations (**Fig.11**), the crack deflection toughening mechanism may be regarded as a source of the high toughness. Also, laser Raman spectroscopy revealed the presence of tetragonal ZrO₂ (**Fig.12**), thus the mechanism of high toughness may consist of not only crack deflection toughening due to dispersed ZrO₂ particles and branching of cracks, but also of transformation toughening of ZrO₂ particles from tetragonal to monoclinic. However, since laser Raman spectroscopy indicated a slightly higher intensity of the band near 610cm^{-1}, there is a possibility that small amounts of tetragonal ZrO₂ were contained in the sintered compact. In the Raman spectrum of the matrix containing ZrO₂ particles, a small sub-peak was observed at 947cm^{-1} in addition to the peak at 961cm^{-1} corresponding to P-O stretching vibration of HAp. This sub-peak may correspond to a shift due to the distortion of the HAp lattice caused by the reaction with tetragonal
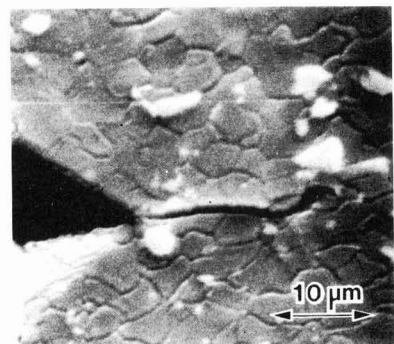

Fig. 11. SEM observation of an indent and surface crack on TZ3Y+HAp ceramics post-sintered by HIP at 1050°C under 200MPa of Ar for 1h, after hot-pressing at 1050°C under 30MPa for 3h in Ar. Crack deflection is clearly observed.

Table 2. Mechanical properties of several hydroxyapatite ceramics.

| Sample Name | Treatment Conditions | | | Crystalline Phase | Relative Density % | H_v* GPa | K_{1c}* MPa·m$^{1/2}$ |
	Normal Sintering	Hot Pressing	HIP Post-.sintering				
TZ3Y+HAp	——	1050°C, 30MPa, 1h	——	T-ZrO₂, HAp	92.8	4.8	2.6
	——	1050°C, 30MPa, 1h	1050°C, 200MPa, 1h	T-ZrO₂, HAp	98.6	5.5	2.8
	——	1150°C, 30MPa, 1h	——	C-ZrO₂, HAp, TCP	>97.1	5.5	2.2
Pure HAp	1050°C, 3h	——	——	HAp	90.0	4.1	1.2
	1050°C, 3h	——	1000°C, 200MPa, 1h	HAp	99.9	6.3	1.1
	1100°C, 3h	——	——	HAp	97.2	5.4	1.1

*   Vickers: Load 2.94 N

ZrO_2. In the matrix containing no ZrO_2, however, a spectrum nearly identical to that of HAp was observed. From the measurement results of XRD and laser Raman spectroscopy, it is suggested that a low degree of reaction which could not be detected by XRD took place between HAp and tetragonal ZrO_2.

Tamari et al.[33] reported that the addition of CaF_2 was effective in densifying powders that had been prepared by mixing 50vol% tetragonal ZrO_2 (2mol% Y_2O_3-containing ZrO_2) with HAp, and showed that hot pressing at 1300°C provided a relative density of 94%, while hot pressing at 1400°C provided a relative density of 99.5%. In that system, however, there were two major problems: the bioactivity decreased compared with that of HAp alone because the HAp reacted with CaF_2 to yield fluorine apatite, and the transformation toughening due to ZrO_2 particles could not be realized because tetragonal ZrO_2 changed into the cubic phase. In addition, problems of high sintering temperatures and coarse particles arose because the starting material was a poorly dispersed powder prepared by mechanical mixing. In fact, the compact hot pressed at 1400°C showing the highest density only had a K_{IC} value of about 3MPa·m$^{1/2}$, even though large amounts of ZrO_2 particles (up to 50vol%) were added. By contrast, the series of processes from preparation of powders to sintering used in the present study can produce composite ceramics of this system at temperatures as low as 1050°C without a change of tetragonal ZrO_2 into the cubic phase and without the discomposition of HAp. Moreover, the addition of only 10vol% of a toughening agent increases the fracture toughness of HAp by about 2.5 times. If the optimum condition can be found by further studying the content and particle size of ZrO_2, then the mechanical properties of the ceramics of this system can be improved further.

4. Conclusions

ZrO_2-HAp composite powders, consisting of homogeneous mixtures of ZrO_2 particles and ultra-fine HAp single crystals, were synthesized hydrothermally. Starting materials were 3mol% Y_2O_3-containing ZrO_2 particles with two different particle sizes (TZ3Y having large particle size and 3YZ having small particle size). In the composite powders of this system, the individual powders were dispersed homogeneously as compared with the powders mixed mechanically, irrespective of the particle size of ZrO_2.

The relative density of TZ3Y-HAp composite powders reached about 99% when the powders were hot-pressed at
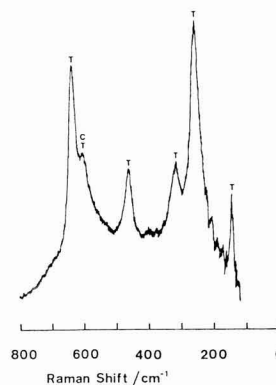

Fig. 12. Raman spectra of zirconia particles of the post-sintered TZ3Y+HAp ceramics.

T: tetragonal and C: cubic.

1050°C under 30MPa for 1 hour and then post-sintered by HIP at 1050°C under 200MPa of Ar for 1 hour. In this sintered compact, tetragonal ZrO_2 particles were dispersed with no discomposition product, TCP, observed. This sintered compact had nearly the same hardness as a dense body of HAp alone, and a fracture toughness K_{IC} (2.8MPa·m$^{1/2}$) about 2.5 times that of the dense body of HAp alone. This compact was toughened by the toughening mechanism of crack deflection and branching, and probably by the toughening mechanism of transformation from tetragonal to monoclinic ZrO_2 particles.

In the 3YZ+HAp system, ZrO_2 changed into the cubic phase due to the reaction between ZrO_2 and HAp, and HAp ceramics with dispersed tetragonal ZrO_2 particles were not prepared.

References:
1) M. Akao, H. Aoki and K. Kato, J. Mater. Sci., 16, 809-12 (1981).
2) K. Ioku, M. Yoshimura and S. Somiya, Seramikkusu Ronbunshi (J. Ceram. Soc. Jpn.), 96, 109-10 (1988).
3) K. Ioku, M. Yoshimura and S. Somiya, "Bioceramics," Vol.1, Ed. by H. Oonishi, H. Aoki and K. Sawai, Ishiyaku Euro-Amerca, Tokyo and St. Louis (1989) pp.62-67.

4) N. Claussen. J. Am. Ceram. Soc., 59, 49-51 (1976).

5) N. Claussen, J. Am. Ceram. Soc. 61, 85-86 (1978).

6) P.F. Becher, J. Am. Ceram. Soc., 64, 37-39 (1981).

7) A.G. Evans, "Advances in Ceramics 12, Science and Technology of Zirconia II," The Am. Ceram. Soc., Columbus, OH (1984) pp.193-212.

8) N. Claussen, ibid., pp.325-51.

9) M. Yoshikawa and S. Somiya, Ceramics Japan, 21, 126-34 (1986).

10) T. Sato and M. Shimada, Ceramics, Japan 21, 613-20 (1986).

11) N. Miura, M. Akao, H. Aoki and K. Kato, Report of the Institute for Medical & Dental Engineering, 17, 21-27 (1982).

12) N. Tamari, M. Mouri and I. Kondo, Yogyo-Kyokai-shi, 95, 806-09 (1987).

13) K. Yamashita, T. Kobayashi, T. Umegaki and T. Kanazawa, "Sintering '87," Vol.2, Ed. by S. Somiya, M. Shimada, M. Yoshimura and R. Watanabe, Elsevier applied Science, London, New York and Tokyo (1988) pp.1320-25.

14) H. Kojima, S. Komatsudani, I. Tanaka and I. Ishijima, Proc. Fall Meeting, The Ceram. Soc. Jpn., Sept. 28-30, 4-1D06 (1988) pp. 367-68.

15) J-M. Wu and T-S Yen, J. Mater. Sci., 23, 3771-77 (1988).

16) S. Somiya, K. Ioku and M. Yoshimura, "Materials Science Forum," Vol.34-36, Ed. by C.C. Sorrell and B. Ben-Nissan, Trans Tech Publications Ltd., Switzerland (1988) pp.371-78.

17) K. Ioku, M. Yoshimura and S. Somiya, "Mat. Res. Soc. Symp. Proc. Vol.110, Biomedical Materials and Devices," Ed. by J.S. Hanker and B.L. Giammara, Mater. Res. Soc., Pennsylvania (1989) pp.445-50.

18) K. Ioku, M. Yoshimura and S. Somiya, Biomaterials, 11, 57-61 (1990).

19) K. Ioku, M. Yoshimura and S. Somiya, Nippon Kagaku Kaishi (J. Chem. Soc. Jpn.), 1988, 1565-70.

20) S. Somiya, "Advanced Ceramics", Kodansha Scientific, Tokyo, (1984) pp.31-32.

21) S. Somiya, M. Yoshimura, Z. Nakai, K. Hishinuma and T. Kumaki, "Advances in Ceramics 21, Ceramic Powder Science," The Am. Ceram. Soc., Columbus, OH (187) pp.48-55.

22) H.P. Klug and L.E. Alexander, "X-ray Diffraction procedures," John Wiley and Sons, New York, London, Sydney and Toronto (1974) pp.618-708.

23) K. Niihara, Ceramics Japan, 20, 12-18 (1985).

24) T. Noma, M. Yoshikawa, M. Kato, M. Shibata, H. Seto and S. Somiya, "Zirconia Ceramics 6", Uchida Rokakuho, Tokyo, (1986) pp.1-7.

25) Y. Makijima and H. Aoki, "Ceramic Science Series 7; Bioceramics", Gihodo, Tokyo (1984) pp.6-9.

26) JCPDS Card 9-432.

27) T. Kanazawa, "Inorganic Phosphorus Chemistry", Kodansha Scientific Tokyo (1985) p.58.

28) JCPDS Card 26-341.

29) JCPDS Card 27-997.

30) M. Mathew, L.W. Schroeder, B.Dickens and W.E. Brown, Acta Cryst., B33, 1325-33 (1977).

31) T. Kanazawa, T. Umegaki, H. Nonma and K. Yamashita, Gypsum&Lime, [210] 261-73 (1987).

32) H. Aoki and S. Niwa, "Bioceramics; Development and Clinical Applications", Quintessencex, Tokyo, Berlin, Chicago, London, Sao Paulo, Hong Kong (1987) p.10.

33) N. Tamari, I. Kondo, M. Mori and M. Kinoshita, Seramikkusu Ronbunshi (J. Ceram. Soc. Jpn.) 96, 1200-02 (1988).

Inclusion Removal in a Green Ceramic Body by Acid Treatment-Zirconia Ceramic Capillaries for Optical-Fiber Connectors

Koichi Hayashi and Kenji Morinaga[*]

R&D Division, TOTO Ltd., 2-1-1, Nakashima, Kokurakita-ku, Fukuoka 802

*Department of Materials science and technology, Graduate School of Engineering Science, Kyushu University,

6-1, Kasugakouen, kasuga-shi, Fukuoka 816

The removal of metallic and/or oxide inclusions in green bodies for PSZ ceramic capillary contaminated in the forming process by nitric acid treatment was investigated. The main inclusions contaminated in the forming process was Fe, and it changed to Fe_2O_3 and/or Fe_3O_4 by oxidation in the calcining process. For infiltration of the acid and handling, the specimen with relative density below 70% having open pores and bending strength above 70MPa was desired. For the ease of removing of inclusions, it was desired that inclusions remained as metallic state. These conditions were achieved by calcining specimens in the temperature range from 600 to 800°C for 1hr. PSZ ceramic capillaries for optical-fiber connector with Weibull modulus of 10.24 and bending strength of 925MPa were fabricated by sintering at 1450°C in air for 12hr and HIPing at 1400°C and 1000atm in an Ar atmosphere for 2hr after the acid treatment.

1. Introduction

Inclusions in ceramic products are generally caused by contaminants from the equipment used in the production process; specifically, the inclusions consist mainly of metals or metal oxides arising from wear of the kneader or molder during injection molding.[1] For example, commercially available partially stabilized zirconia (PSZ) powders containing small amounts of Cl contaminants due to the formation method[2] tend to deteriorate when they come into direct contact with the metallic parts (blade, jacket, cylinder, and screw) of the kneader and the injection molder. Because of these contaminants, the powders tend to contain more inclusions of foreign matter ceramic green bodies than do

alumina powders.

Many studies on formation processes, including the improvement of kneading and molding methods, have been conducted to prevent inclusions.[1,3] However, as yet, no concrete, cost-effective solutions have been reported. The inclusions in ceramic green bodies are too small in quantity and in size to be identified by the naked eye. Their presence is usually determined in an optical inspection process after sintering. Since a low yield of products and a lack of stability of physical properties result from the inclusions, if they can be removed without damage to the green bodies prior to sintering, improvements in yield and quality will result without requiring any changes in the formation process.

This report discusses the possibility of and the effects due to a nitric acid treatment removal of metallic and oxide inclusions in PSZ ceramic green bodies formed by the injection molding method.

2. Experimental Methods

2.1. Materials

A TZ-3Y PSZ powder (Tosoh Corporation) and nitric acid (guaranteed reagent,Wako Pure Chemical Industries, Ltd.,) were used as starting materials. **Table 1** gives the chemical composition of the PSZ powder (analysis provided by the manufacturer). The 61% nitric acid was used for removing inclusions without being diluted.

2.2. Experimental

Figure 1 is a flow chart of the fabrication process for the PSZ ceramic capillaries. The PSZ powder and an organic binder were weighed to a specified proportion and wet mixed in a nylon ball mill with benzene as the solvent. After the benzene was removed with a distiller, the mixture was kneaded in an alumina roll mill and a ceramic stamp mill. Ceramic capillaries for use as optical-fiber connectors were prepared from the kneaded compound via an injection

Table 1. Chemical content and characteristics of starting PSZ powder.

TZ-3Y (TOSOH Co.)	Chemical Content (wt%)	Y_2O_3	4.980
		Al_2O_3	0.005
		SiO_2	0.002
		Fe_2O_3	0.003
		Na_2O	0.019
		ZrO_2	94.991
	Powder characteristics	BET (m²/g)	15.400
		T-phase (%)	82.000

molding method,[4-6] and calcined after debinding. The calcination was performed in air in a temperature range of from 600°C to 1450°C for 1 hour. The PSZ ceramic capillaries were acid treated and then sintered at 1450°C in air for 12 hours, followed by HIP at 1400°C and 1000atm in an Ar atmosphere for 2 hours. The debinding conditions are as shown in Fig.1. The conditions for acid treatment will be described in Section 2.4.

2.3. Measurement

The relative density of the specimen was measured by the Archimedean method using distilled water. For the identification of inclusions and their oxidation during the

Fig. 1. Flow sheet for fabrication of ceramic capillaries.

Fig. 2. Schematic drawing of an acid treatment apparatus.

1. Hot plate 2. Vacuum desiccator 3. Sample 4. Vacuum pump
5. Condenser

heating process, a high-temperature X-ray diffractometer (Mac Science MXP18) was used. The rate of elution of inclusions in the green body by the acid treatment was measured with an atomic absorption photometer, (Hitachi Z-600). The microstructure of the specimen was observed with an SEM (Hitachi S-800), and the elemental analysis was performed with an EPMA (Horiba EMAX-3000). The bending strength of ceramic capillaries, 2500mm OD and 0.130mm ID, was measured with a three-point bending tester (Shimazu OSS-5000), using a 10mm span and a 0.5mm/min crosshead speed.

2.4. Acid Treatment

Figure 2 shows the apparatus employed in the acid treatment. Nitric acid was the acid of choice; if it is quickly removed from the product after acid treatment, it has little effect on the product during sintering. Other acids such as sulfuric acid, hydrochloric acid, or aqua regia could have been used, but were less suitable because the main inclusions in the PSZ ceramic green bodies were Fe and its oxides; in addition, SO_4^{2-} and Cl^- are not be easily removed by mere washing and could form sulfides or chlorides, such as $CrCl_3$, which is stable up to high temperatures.[7]

The acid treatment was performed as follows: the specimen was placed in a desiccator which was evacuated to about 10^{-1} Torr using a rotary pump. The nitric acid was then admitted into the desiccator and the pressure was further reduced. The dessicator was allowed to return to atmospheric pressure via a slow leak, and was then heated to a specified temperature on a heating plate; the temperature was maintained for a specified period of time, and then allowed to cool. After acid treatment, the specimen was removed from the desiccator, washed, and then placed in another desiccator. After a vacuum was produced in the second desiccator, distilled water was admitted for washing. After this washing operation was performed two times, the specimen was placed in a drier and heated at 100°C for 12 hours.

3. Results and Discussion

Figure 3 shows the appearance of ceramic capillaries (a), the SEM photograph of inclusions in the product (b), the EDX analysis results (c), and the result of an FeK surface analysis (d). The inclusions in the green bodies could not be identified by the unaided eye, but inclusions in the sintered products appeared as brown spots (see in Fig.3(a)). Figures 3(c) and 3(d) indicate that the inclusions in the products were mainly Fe or its oxides. As shown in the flow chart of Fig.1, the compound does not come into contact with any metal parts until it is kneaded. Moreover, the PSZ powder itself contained almost no metal. Therefore, the metallic inclusions most likely entered from the screw and the cylinder of the injection molder that came into contact with the compound during injection molding.

Figure 4 shows the relationship between the relative intensity and firing temperature for Fe and its oxides. Metallic powder samples were taken off the screw and cylinder of the injection molder, ground to 100 mesh or below, and then heated in air for X-ray analysis. The relative intensity was calculated from the heights of the principal peaks of Fe(110), Fe_2O_3(311) and Fe_3O_4(104) faces in the high-
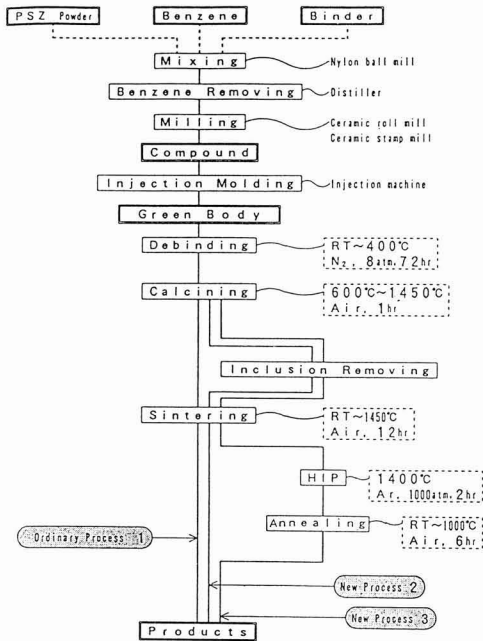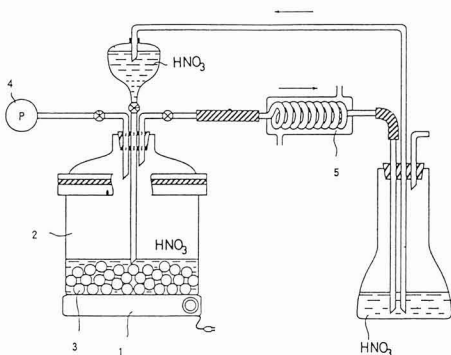
Fig. 3. Ceramic capillaries and metallic inclusions.
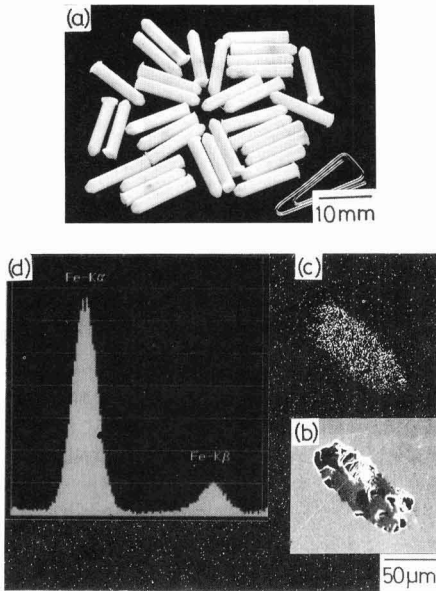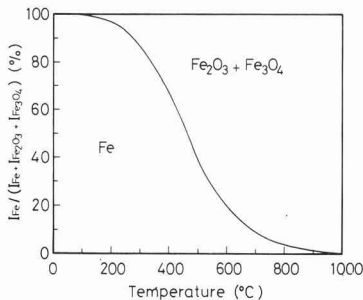(a) Photograph of ceramic capillaries, (b) SEM photograph of metallic inclusions, (c) EDX spectrum, (d)FeKα

Fig. 4. Relationship between the relative intensity of X-ray diffraction pattern, $I_{Fe}/(I_{Fe}+I_{Fe2O3}+I_{Fe3O4})$ and firing temperature of the metallic powder sampled from a injection molding machine.

temperature X-ray diffraction pattern at each temperature. As seen from Fig.4, the formation of oxides was not observed until the firing temperature reached 300°C. Above 400°C, the formation of Fe_2O_3 and Fe_3O_4 was observed. With an increase in firing temperature, the relative intensity of Fe_2O_3 and Fe_3O_4 increased, while that of Fe decreased. Above 800°C, Fe disappeared, and only Fe_2O_3 and Fe3O4 remained. This fact indicates that the inclusions are Fe when the green body is calcined below 300°C; Fe and its oxides are formed in the temperature range from 400°C to 800°C, and only Fe_2O_3 and Fe_3O_4 are formed above 800°C. The elements Cr, Ni, and Mo which were components of the screw and cylinder of the injection molder[1,8] were not detected by high-temperature X-ray diffraction because their amounts were too small.

3.2. Dissolution of Inclusions by Acid Treatment

Figure 5 shows the dissolution time as a function of the dissolution temperature. The dissolution time is the time required to completely dissolve in nitric acid the metallic powder sampled from the screw and cylinder of the injection molder as well as the oxide produced by heating the metallic powder in air at 1200°C for 5 hours. The acid treatment was performed by the procedure described in Section 2.4 by placing 1 mg of metallic powder and 1 mg of oxidized metallic powder into 100ml of nitric acid. Figure 5 indicates that the higher the temperature, the shorter the dissolution time, and that the metal dissolves more rapidly at lower temperatures than does the oxide. This suggests that inclusions are more easily dissolved by acid treatment when they are in the metallic state.

3.3. Optical conditions of Specimen for Acid Treatment

Figure 6 shows the relationships between the relative density and bending strength versus the calcining temperature for specimens calcined for 1 hour. The SEM photographs in the figure represent the specimens acid-treated at 102°C for 30 hours after being calcined at 550°C[a] and 600°C[b] for 1 hour. The figure indicates that the relative density and bending strength increased, i.e., densification proceeded, with a rise in the calcining temperature. The specimens calcined at 550°C were fractured by acid treat-
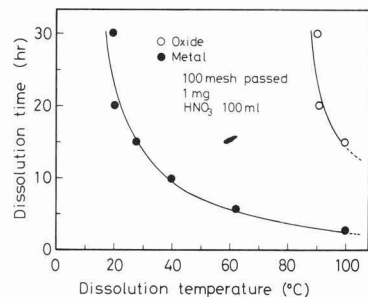

Fig. 5. Dissolution time of the metal and oxide powder as a function of dissolution temperature.
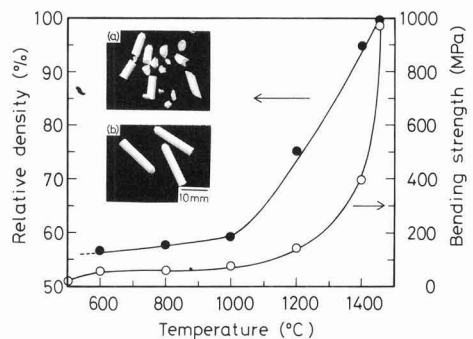

Fig. 6. Relationship between relative density or bending strength and calcining temperature for the PSZ ceramic capillaries and SEM photographs of PSZ ceramic capillaries after the acid treatment. (a) Calcined at 550°C, (b) Calcined at 600°C
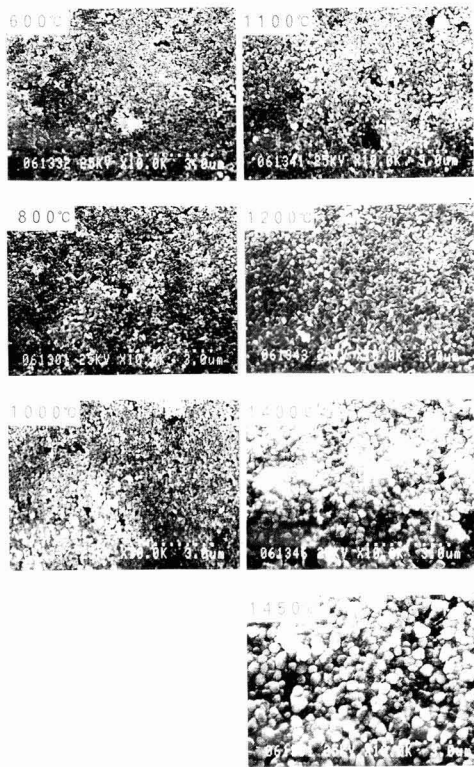
ment as shown in (a), while those calcined at 600°C were not fractured as shown in (b), and exhibited a bending strength of 70MPa.

Figure 7 shows the SEM photographs of the surfaces of the specimens calcined at different temperatures for 1 hour. As seen from these photographs, only homogeneous open pores were observed on the surface of the specimens calcined in the temperature range of from 600 to 1000°C; some closed pores, however, are found in addition to the open pores on the surface of the specimens calcined at 1100°C and 1200°C. On the surface of the specimens calcined above 1400°C, no pores were observed at all.

To dissolve the inclusions in ceramic green bodies by acid treatment, it is necessary for the acid to permeate through the entire body to fully react with the inclusions as well as to be easily removed after reaction. **Figure 8** shows schematic diagrams of a green body specimen and specimens calcined at the specified temperatures. The inclusions in the green body are surrounded by the organic binder as shown in Fig.8(A). The organic binder prevents acid from infiltrating, making the direct reaction between the inclusions and the acid difficult. In addition, heating the specimen to the acid treatment temperature softens the organic binder, so that the specimen shape cannot be maintained. Therefore, the acid treatment under these conditions is undesirable.

As shown in Fig.8(B), the organic binder is no longer present, leaving only open pores in the specimens calcined

at 600°, 800°, or 1000°C. Therefore, the acid infiltrates easily into the interior of the specimen when a vacuum is produced in the desiccator as previously described in Section 2.4, and results in a rapid reaction between the inclusions and the acid. Above 1100°C, however, closed pores are formed as shown in Fig.8(C), making it very difficult to dissolve the inclusions in the specimen. For the specimens calcined at 1400° or 1450°C, the densification has already been completed as shown in Fig.8(D); for example, a solid solution of Fe_3O_4 and ZrO_2 is formed between the inclusions and the ceramic body,[10,11] which makes the acid permeation and the dissolution of the inclusions impossible.

As shown in Fig.4, most of the inclusions are Fe, and the proportion of Fe_2O_3 and Fe_3O_4 increases with an increase in the calcining temperature. According to Inoue,[12] Fe dissolves more easily in acid than Fe_2O_3 and Fe_3O_4. Analogous results in this study were obtained (see Fig.5), indicating that metals dissolved more easily than oxides.

Based on the above results, it is desirable to have a specimen with a relative density below 70%, such that all pores consist of open pores for effective acid treatment, and with a bending strength above 70MPa such that the specimen does not break in handling.[9] Furthermore, a specimen with a high proportion of metallic inclusions is desirable in order to improve the effectiveness of the reaction between the inclusions and the acid. It has been found in these experiments that a specimen calcined in the temperature range of from 600°C to 800°C for 1 hour meets the above conditions.

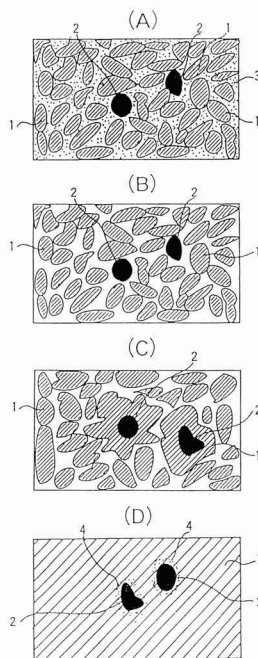**Fig. 8.** Schematic drawing of the inclusions in the PSZ ceramic capillaries.
1. PSZ 2. Contamination 3. Organic binder 4. Fe$_3$O$_4$ss-ZrO$_2$ss
(A) Green body (B) Calcined below 1000°C
(C) Calcined at 1200°C (D) Calcined at 1400° and 1450°C

Figure 9 shows the effect of acid treatment in the surface roughness for specimens calcined at 600°C in air for 1 hour. The sintering was performed at 1450°C for 12 hours. A, B, and C represent the specimens sintered after acid treatment, those sintered without acid treatment, and the metal mold, respectively. The figure indicates that the surface roughness was unchanged and that the particles did not come off, irrespective of acid treatment. The surface condition of the ceramic green body depended generally on the organic binder. Although some particles may have come off during acid treatment or when the organic binder was removed after calcination, no deformations large enough to change the shape were observed. The surface roughness after sintering depended mainly on the finished condition of the metal mold, the formation pressure, and the organic binder filling condition, and not on the acid treatment after calcination.

3.5. Evaluation of Ceramic Capillaries as Optical-Fiber Connectors

To investigate the acid treatment removal of inclusions in actual ceramic capillaries, the dissolution rate of metal and oxide powders shown in Fig.5 under different conditions of calcining and acid treatment was evaluated. The results are shown in **Fig.10**. The conditions of calcining and acid treatment for each sample in Fig.10 are summarized in **Table 2**.

The specimens calcined at 600°C for 1 hour, acid-treated at 102°C for 30 hours, and then sintered at 1450°C for 12 hours, appeared to lack inclusions as was earlier shown in Fig.3(a). Using this concentration inclusion as a basis, the rate of dissolution of inclusions under each condition of acid

treatment was determined. As seen from the results of Specimens 1 and 2, a vacuum produced in the desiccator before acid treatment accelerates the permeation of the acid into the green body, facilitating the reaction between the inclusions and the acid; this was also observed for the metal powders, resulting in the dissolution of inclusions at a low temperature in a short period of time. When Specimen 1 was acid-treated at a higher dissolution temperature for a longer period of time, the inclusions completely dissolved as shown in the results for Specimen 1′. For Specimens 3 and 4, densification proceeded further than for Specimen 1, and closed pores were formed as shown in Figs.6 and 7. Therefore, it was difficult to achieve acid penetration the green body even though a vacuum was produced in the desiccator, and this resulted in a decrease in the rate of dissolution of inclusions.

Figure 11 shows the relationship between the fracture probability (P_f) and the bending strength (σ) via a Weibull plot; in addition SEM photographs of the fracture and mirror surfaces of Specimens 1 through 3 are shown. Specimen 1 was sintered without acid treatment, Specimen 2 was sintered after acid treatment, and Specimen 3 was sintered after acid treatment and then HIP-treated. In the figure, the bending strength as well as the Weibull modulus is indicated for each specimen. The calcining was performed at 600°C for 1 hour-the optimal condition for acid treatment. The acid treatment was performed at 1020°C for 30 hours. The sintering and HIP were performed under the conditions shown in Fig.1. The linear relationship between P_f and σ for each specimen, as shown in Fig.11, indicates that the Weibull distribution holds.[13] Photos 1 and 2 indicate that inclusions about 50μm across exist within Specimen 1, which was not acid-treated, and that the inclusions are the starting points of fracture. In Specimen 2, which was acid-treated, no inclusions were found, but minute pores of about 10μm across were observed which were the starting points
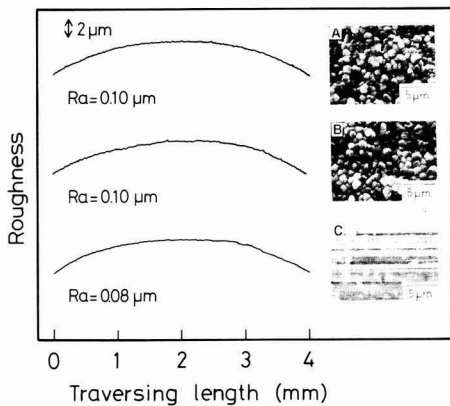
Fig. 9. Surface roughness of PSZ ceramic capillary and metal mold.

(A) Acid treatment (B) Without acid treatment (C) Metal mold
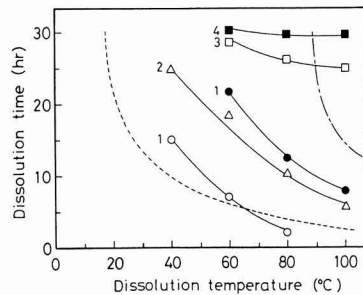
Fig. 10 Dissolution time of inclusions as a function of dissolution temperature for PSZ ceramic capillaries corresponding to Table 2.

Table 2. Conditions of calcining and acid treatment, relative density and dissolved proportion of inclusions.

Sample No.	Calcining temperature (°C)	Calcinig time (hr)	Acid treatment	Relative density (%)	Dissolved proportion of inclusions (%)
1	600	1	Vacuum	58.3	50
1′	600	1	Vacuum	58.3	100
2	600	1	—	58.3	50
3	1200	1	Vacuum	73.1	50
4	1450	1	Vacuum	99.8	10

Fig. 11. Weibull distribution of bending strength and SEM photographs of surfaces for PSZ ceramic capillaries.
1. Sintered without the acid treatment, 2. Sintered after the acid treatment, 3. HIPped after the acid treatment and sintered,
(a) Fractured surface (b) Mirror surface.

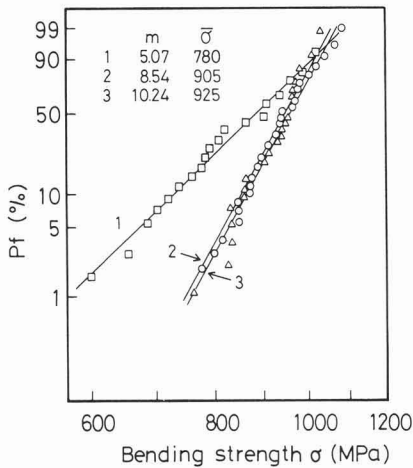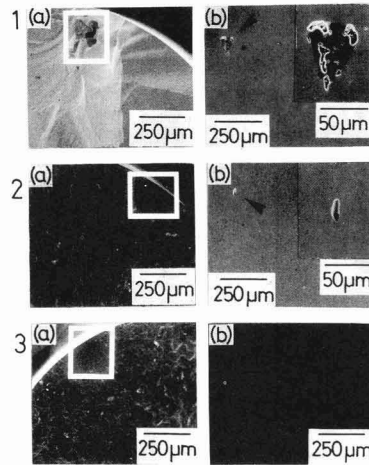of fracture. These pores may have been formed when the voids produced after the removal of inclusions by the acid treatment shrunk during sintering, and may explain why the Weibull modulus for Specimen 2 of 8.54 was higher than the value of 5.04 for Specimen 1.

Specimen 3 exhibited a Weibull modulus of 10.24 and a bending strength of 925MPa; both of these values were higher than those of Specimens 1 and 2. The reason for this may be explained in photograph 3 of Fig.11; the voids produced after the acid treatment removal of all the inclusions, which were mainly Fe, were changed into pores by sintering, and the pores disappeared completely during HIPing. Therefore, neither inclusions or pores existed which could act as fracture starting points, and the fracture started from the surface of the specimen.

It has been reported that the mechanical properties required by a ceramic capillary to be used as an optical-fiber connector are generally a Weibull modulus above 8.00 and an average strength above 800MPa for PSZ ceramics.[14] According to Tanaka,[15] an improvement in the reliability, such as the Weibull modulus, by HIP cannot be expected unless all inclusions are removed since the fracture of ceramics often starts from an inclusion, and since the segregation of metallic inclusions, like Fe, occurs at the fracture starting points.[16] This also means that Specimens 2 and 3, from which inclusions were removed by acid treatment, meet the requirement for ceramic capillaries for use as optical-fiber connector, and Specimen 3, which was HIP-treated, will be the best for this application.

Although Cr, Ni, and Mo, were also detected as inclusions minute in amounts in the green bodies as described above, it was shown that they may be removed, like Fe, by acid treatment, according to the results in Fig. 11.

4. Conclusions

The nitric acid treatment removal of metallic and oxide inclusions in green bodies of PSZ ceramic capillaries formed by the injection molding method was investigated. The main inclusions entering the green bodies during the formation process were Fe, changing to Fe_2O_3 and Fe_3O_4 by oxidation in the calcining process. The most effective removal of these inclusions by acid treatment, was for a specimen exhibiting a relative density below 70% having only open pores and a bending strength above 70MPa. It was also desirable to have inclusions that remained in the metallic state. These conditions were achieved by calcining specimens in air at temperatures ranging from 600° to 800°C for 1 hour.

The voids produced after the removal of inclusions by acid treatment shrunk during sintering and remained in the specimen. After sintering, these pores disappeared completely by HIP. The specimen undergoing acid treatment and HIP had a Weibull modulus of 10.24 and a bending strength of 925MPa; these values were considered sufficient for acceptable ceramic capillaries to be used as optical-fiber connectors.

References:
1) M.Inoue, "Injection Molding Technology for Fine Ceramics", The Daily Industrial News (1987) pp.127-42
2) K.Ri, Yogyo-Kyokai-Shi, 95, 736-40 (1987)
3) O.Kobayashi, Patent Gazette 1989-234172
4) K.Hayashi, Patent Pending
5) K.Hayashi, O.Kobayashi, and K.Morinaga, Report of General Science and Engineering Research Faculty, Postgraduate Research Institute, Kyushu University, 12, 9-15 (1990)
6) M.Inoue, Technical Report of the Japan Steel Works, Ltd., 42, 1-6 (1986).
7) F. Tamamushi et al., ed., "Iwanami's Dictionary of Physics and Chemistry, 4th Edition", Iwanami Shoten (1987) pp.152-153.
8) M.Inoue, Technical Report of the Japan Steel Works, Ltd., 42,151-52

(1986).

9) R.L. Coble and W.D. Kingery, J. Am. Ceram. Soc.,39 377 (1956).

10) M. Yanagisawa, Japan Ceramics Association 1990 Annual Proceedings, 540 (1990).

11) E.M. Levin, C.R. Robbins and H.F. McMurdie, "Phase Diagrams for Ceramists, 1969 Supplement" Ed. by M.K. Reser, Am. Ceram. Soc., Inc. (1969) p45.

12) K. Inoue, Yogyo-Kyokai-Shi, 92, 520-24 (1984).

13) The Ceramic Society of Japan, ed., "Mechanical Properties of Ceramics" (1979) pp.21-24.

14) E. Sugita, Journal of the Institute of Electronics and Communication Engineers of Japan, CS12-85 (1985).

15) M. Tanaka, Materials, 37, 1197-203 (1987).

16) M. Oyishi, Japan Ceramics Association 1990 Annual Proceedings, 163 (1990).

Tricalcium Phosphate Coating on Zirconia Using Calcium Metaphosphate and Tetracalcium Phosphate

Yoshiyuki Yokogawa, Yukari Kawamoto, Motohiro Toriyama, Takahiro Suzuki and Sukezo Kawamura

Government Industrial Research Institute, 1-chome, Hirate-cho, Kitaku, Nagoya City, Aichi-ken 462 Japan

β-tricalcium phosphate (β-TCP) coating on yttria partially stabilized zirconia plate was studied. Firstly, calcium metaphosphate (CaP_2O_6) layer was coated on yttria partially stabilized zirconia as an interlayer by heating at 1000°C for 40 min. Then, a mixed slurry of calcium metaphosphate and tetracalcium phosphate ($Ca_4(PO_4)_2O$) was brought into reaction on the zirconia plate by heating at 1200°C for 40 min. The coated layer was found to be β-tricalcium phosphate with a thickness of about 100μm.

1. Introduction

Ceramics of β-tricalcium phosphate, β-TCP, (β-$Ca_3(PO_4)_2$) are expected to have practical applications as substitute materials for hard biological structures (e.g. artificial bone) due to their high biological affinity. However, high-strength β-TCP ceramics produced to date have only exhibited bending strengths equal to or lower than the bending strength of human dense bone (about $2000kgf/cm^2$).[1,2] To develop adequate substitute materials for hard structures with both biological affinity and mechanical strength, material complexes have been studied. One complexing method providing ceramics with high mechanical strength is via particle dispersion. It has been reported that the dispersion of stabilized zirconia particles in β-TCP yields sintered bodies with a bending strength of 199MPa ($2030kgf/cm^2$);[3] moreover, hot-pressing provides sintered bodies with a bending strength of 440MPa ($4490kgf/cm^2$).[4] However, in order to achieve these strength levels, more than 50wt% of zirconia, which has a low biological affinity, must be added; in addition, zirconia in living bodies containing water tends to deteriorate due to a phase transformation. Another method which might further increase the mechanical strength is the formation of a coating layer of β-TCP, having a high biological affinity, on a high-strength ceramic plate, where the coating would prevent the plate from deteriorating. The authors studied β-TCP coatings on the surface of partially stabilized zirconia ceramic plates which exhibited high strength and toughness. Since β-TCP does not react well on zirconia, an interlayer was formed using calcium metaphosphate; a slurry was prepared by mixing calcium metaphosphate and tetracalcium phosphate in appropriate proportions, which was applied and then heated. In doing so, a new layer coating technique was developed in which the β-TCP coating was also produced in the synthesis.

2. Experimental Methodology

2.1. Synthesis of Raw Material Powders

Calcium metaphosphate, CP, (CaP_2O_6) and tetracalcium phosphate, C4P ($Ca_4(PO_4)_2O$) powders were synthesized by the following method: 0.05mol% calcium carbonate ($CaCO_3$) and 0.1mol% ammonium hydrogen phosphate ($(NH_4)_2HPO_4$ in the case of C4P were mixed in an agate mortar for 1 hour with repeated dry and wet mixing using methanol. The powders were uniaxially pressed under 100MPa and then heated in air at 800°C for 8 hours for CP, or at 1400°C for 8 hours for C4P. Next, the compact was ground into a powder. Appropriate amounts of CP and C4P powders for the desired TCP composition were mixed in an agate mortar for 1 hour using methanol in the same manner as described above. CP or CP + C4P powders were dispersed into an aqueous deflocculant solution (Selnar D-305, Chukyo Yushi) to prepare the slurry.

2.2. Synthesis, Fusing Reaction

Partially stabilized zirconia powder containing 3mol%Y_2O_3 TZ-3YB, Tosoh) was uniaxially pressed under 100MPa into a disk 20mm in diameter. The pressed specimen was heated at 1450°C for 2 hours to yield a sintered compact. The zirconia compact was first coated with the CP slurry and heated at 1000°C for 40 minutes to fuse CP onto the surface of the compact. Then, the compact was coated with the CP + C4P slurry and heated at 1200°C for 40 minutes. For comparison, another zirconia compact was coated with the CP + C4P slurry, without a CP pre-coat, and heated at the same temperature for 40 minutes. In all cases, the compact was heated at a rate of 20°C/min and kept at 500°C for 30 minutes to remove the Selnar prior to being heated to the prescribed temperature described above. After heating, the compact was allowed to cool in the furnace.

2.3. Analysis

Qualitative analysis was performed on the various specimens via the powder X-ray diffraction method (Geiger flex, Rigaku Corp.) using an applied voltage of 30kV, current of 20mA, Cuk α rays and a carbon monochromator. The observation of specimens was performed using a scanning electronic microscope (SEM, SX-5300, Hitachi Corp.) The elementary analysis was performed using an energy dispersion type X-ray analyzer (EMAX-200, Horiba, Ltd). The thermal analysis was performed at a heating rate of
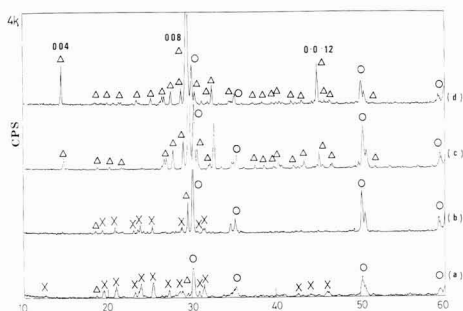
Fig. 1. X-ray diffraction patterns of heat-treated calcium metaphosphate on zirconia plate at various temperatures ((a) 900°, (b) 950°, (c) 1000° and (d) 1050°C),

○: ZrO_2, × :CP (CaP_2O_6), Δ: C2P ($Ca_2P_2O_7$).

10°C/min by using a differential thermal analyzer (TAS 100, Rigaku Corp.).

3. Results and Discussion

β-TCP is not highly reactive with respect to zirconia. Therefore, calcium metaphosphate (CP), a relatively low melting (975°C)[5] calcium phosphate compound, was heated to a temperature above its melting point and fused onto a zirconia plate to form an interlayer to which the β-TCP could adhere. **Figure 1** shows the powder X-ray diffraction patterns of the specimen surfaces heat-treated at temperatures between 900°C to 1050°C. For the specimen heat-treated at 900°C, peaks corresponding to CP[6] and zirconia were observed. For the specimen heat-treated in the temperature range above the melting point of CP, peaks identifying calcium pyrophosphate (C2P)[7] were observed. For the specimen heat-treated at 1050°C, i.e., a temperature 50°C or more above the melting point of CP, the d spacing agreed with that of C2P, but diffraction peaks were observed near $2\theta = 14°$, 30° and 45° which were higher than the JCPD card values. These peaks corresponded to the 0· 0· 12 peaks of 004 and 008 for C2P. This observation suggested that when CP was heated to a temperature above its melting point on the zirconia plate and then crystallized during cooling, the C-axis orientation was crystallized perpendicular to the plate. Figure 2(a) shows the SEM photograph of the surface of the specimen prepared by coating the zirconia plate with CP and heat-treating. For this specimen heat-treated at 1000°C, partially oriented crystals were observed. **Figure 2(b)** shows the cross section of the specimen, and **Figure 2(c)** shows the relative distribution of Ca obtained by the energy dispersion analysis along the direction of the line indicated in Fig.2(b). The interlayer of CP adhered closely to the zirconia plate, and the thickness of the interlayer was about 10 to 20μm.

Figure 3 shows the powder X-ray diffraction patterns of the specimen surfaces. The specimens were prepared by coating a zirconia plate with CP and heat-treating at 1000°C, or by coating with mixed slurry of CP and C4P, and heat-treating at different temperatures between 1000° to 1300°C. For the specimen heat-treated at 1000°C, peaks corresponding to C2P were observed in addition to those for zirconia.
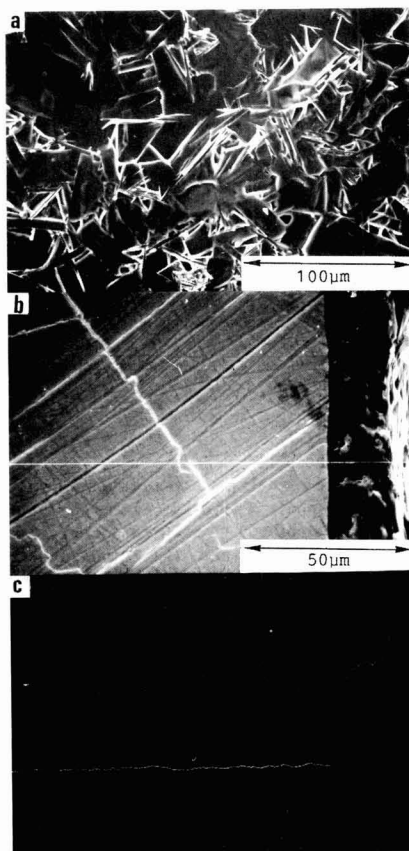
Fig. 2. Scanning electron micrographs of heat-treated calcium metaphosphate on zirconia at 1000°C.

(a) surface, (b) cross-section and (c) Ca ion content analyzed by energy dispersion analysis.

Fig. 3. X-ray diffraction patterns of heat-treated calcium metaphosphate and tetracalcium phosphate at various temperatures ((a) 1000°, (b) 1100°, (c) 1150°, (d) 1200° and (e) 1250°C) on heat-treated calcium metaphosphate on zirconia plate at 1000°C,

○: ZrO_2, Δ: C2P ($Ca_2P_2O_7$), + : β-TCP (β-$Ca_3(PO_4)_2$),

▲ : α - TCP (α-$Ca_3(PO_4)_2$)

Fig. 4. Scanning electron micrographs of heat-treated calcium metaphosphate and tetracalcium phosphate at 1200°C on heat-treated calcium metaphosphate on zirconia at 1000°C.
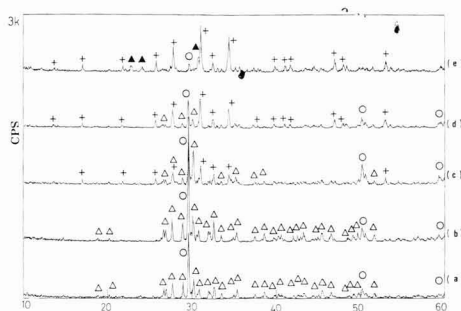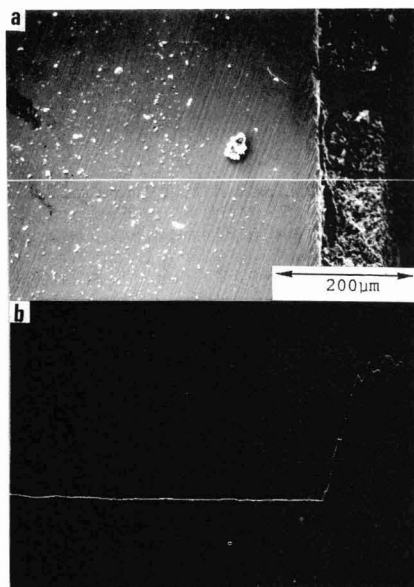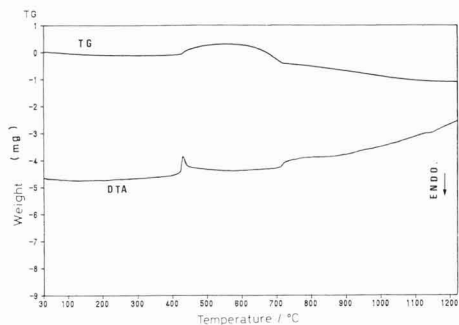(a) Cross-section, (b) Ca ion content analyzed by energy dispersion analysis.

Fig. 5. DTA and TG curves of the mixture of calcium metaphosphate and tetracalcium phosphate in air at a heating rate of 10°C min^{-1}. Sample weight: 40mg.

For the specimens heat-treated at 1150°C or higher, the peaks of tricalcium phosphate (β-TCP)[8] clearly appeared. For the specimen heat-treated at 1200°C, almost all the peaks were identified as those corresponding to β-TCP, although some peaks of C2P remained. This means that C2P and other components were obtained as by-products in the dry synthesis of β-TCP, although only a small amount of C2P was produced partially. When the specimen was heat-treated at 1250°C or higher, the strongest peaks of α-TCP[9] appeared, indicting the occurrence of a phase change from β to α. It was therefore concluded that β-TCP can be satisfactorily produced on a zirconia plate from a mixed slurry of CP and C4P heat-treated at 1200°C. **Figure 4** shows the SEM photograph of the cross section of the specimen heat-

treated at 1200°C as described above. As seen in **Fig.4(a)**, the zirconia plate was coated by a layer of relatively uniform thickness. **Figure 4(b)** shows the relative distribution of Ca analyzed by energy dispersion analysis along the direction of the line indicated in **Fig.4(c)**. These two figures indicate that the coating layer had a thickness above 100μm.

It was concluded that when CP and C4P were heat-treated as described above, C2P was partially formed, followed by the formation of TCP. **Figure 5** shows the thermal change of the mixed CP + C4P powder in the range from room temperature to 1300°C. At temperatures near 400°C, an exothermic reaction was observed which corresponded to the formation of C2P. After this exothermic reaction took place, an increase in weight was observed. This may be due to the absorption of oxygen needed to form C2P. The exothermic reaction observed in the temperature range above 700°C may correspond to the formation of β-TCP, and the exothermic reaction near 1150°C corresponds to the phase change of TCP from β to α. This result also confirms that TCP was formed from C2P. Kanazawa, et al.[10] carefully performed thermal analysis by heating various calcium phosphate compounds, and reported that TCP was synthesized via C2P.

When the zirconia plate was coated with a mixed slurry of C4P and CP without an interlayer of CP then heat-treated, β-TCP and C2P were formed at 1200°C as in the case where an interlayer of CP was used. At the same time, however, C4P, a starting material, and α-TCP, the high-temperature phase of β-TCP, also partially appeared. When the specimen was heat-treated at 1300°C, the starting material C4P did not appear, but the relative-quantity of α-TCP increased with respect to β-TCP. Without an interlayer of CP, the synthesis of β-TCP was not efficient, possibly due to the partial phase change from β to α. When the zirconia plate was coated with CP, C2P was formed which accelerated the reaction of CP and C4P on the surface to yield β-TCP. Thus, the use of an interlayer of CP resulted in a superior coating.

It is known that zirconia stabilized by the dissolution of oxides is changed to the monoclinic form by re-heating or by the presence of various additives. Wilson[11] studied specimens of the ZrO_2-CaO system to which phosphoric acid was added, and found that destabilization occurred at 1100°C. In the present study, partially stabilized zirconia containing 3mol% yttria was used as the base plate, and the surface of the zirconia plate was coated with CP by heating at 1000°C and then coated with a mixed slurry of CP and C4P at 1200°C. To study the interface between calcium phosphate and the zirconia plate, the specimen prepared in the above-described manner was immersed into a water solution of acetic acid diluted three times and investigated by the powder X-ray diffraction method. No peaks of β-TCP were observed due to the β-TCP having dissolved into the acid, however other peaks appeared in addition to those of zirconia and acid-resistant calcium pyrophosphate.[5] These additional peaks appeared at positions corresponding to zirconium phosphate $(Zr_{2.5}(PO_4)_3)$,[12] indicating that the stabilized zirconia plate reacted with the phosphate, and also that the coating layer chemically adhered closely to the plate. It further suggests that destabilization of stabilized zirconia occurred. The effect of this destabilization will be the focus of future studies.

4. Conclusions

A partially stabilized zirconia plate was coated with β-TCP by coating the zirconia plate with a mixed slurry of calcium metaphosphate and tetracalcium phosphate and then heat-treating. The use of an interlayer of calcium metaphosphate improved the adherence of the coating layer to the zirconia plate and accelerated the synthesis of β-TCP. It was found that the reaction to synthesize β-TCP from calcium metaphosphate and tetracalcium phosphate occurred via the formation of calcium pyrophosphate.

References:

1) M. Jarcho, R. L. Salsbury, M. B. Thomas and R. H. Doremus, J. Mater. Sci., 14, 142-150 (1979).

2) M. Akao, H. Aoki, K. Kato and A. Sato, J. Mater.; Sci., 17, 343-346 (1982).

3) M. Akao, H. Aoki, K. Tachiki, and T. Yamamoto, Yogyo-kyokai-shi, 95, 819-21 (1987).

4) N. Tamari, I. Kondo, and M. Mori, Yogyo-kyokai-shi, 96, 106-108 (1988).

5) Handbook of Chemistry, Volume on Basics, Revised 3rd Edition, "3. Properties of Compounds" p.I-116, The Chemical Society of Japan ed. (1984).

6) JCPDS #11-39.

7) JCPDS #9-346.

8) JCPDS #9-169.

9) JCPDS #9-348.

10) T. Kanazawa, Y. Katayama, M. Ueda, and S. Inoue, Kogyo Kagaku Zasshi, 72, 1253-1258 (1969).

11) H. H. Wilson, J. Am. Ceram. Soc., 57, 455-456 (1978).

12) JCPDS #38-17.

Phase Equillibria in the Al_2O_3-Y_2O_3-SiO_2 System, and Phase Separation and Crystallization Behavior of Glasses

Yuichiro Murakami and Hirokazu Yamamoto

Advanced Technology Research Center, Mitsubishi Heavy Industries, Ltd.
Sachiura 1-8-1, Kanazawa-ku, Yokohama-shi, 236, Japan

Subsolidus phase equilibria in Al_2O_3-Y_2O_3-SiO_2 system and the phase separation and crystallization behavior of glass in this system were studied by X-ray diffraction, differential thermal analysis, scanning electron microscopy and X-ray microanalysis. Phase relations, liquidus and solidus temperatures in this system were obtained. Phase equilibrium was not confirmed in a lower temperature than solidus temperature near 1340°C. The glass transition temperature (T_g), the starting temperature of crystallization (T_c), the 1st and 2nd peak temperatures of crystallization (T_o, and T_o', respectively) were studied as a function of composition. The activation energy of crystallization ΔE was determined by analyzing the heating rate dependence of To and found to be in a range of 472 ~ 890kJ/mol, depending on the composition. ΔE had a tendency to increase with decrease in liquidus temperature, suggesting that the glass becomes stable in compositions with lower liquidus temperatures. During heat treatment of glass at 1300°C, the phase separa tion was found to occur as an early stage of crystallization.

1. Introduction

The Al_2O_3-Y_2O_3-SiO_2 system can be manifest as a high-modulus, high-hardness and alkali-resistant glass, and has been extensively studied as the starting mixture for glass fibers.[1-5] Makishima et al.[3,4] studied the glass-forming range of the ternary system, reporting that the glass produced exhibited a high modulus of elasticity and softening temperature. More recently, Oda et al.[5] studied the effects of composition of the ternary system on the glass transition temperature and the modulus of elasticity, where the SiO_2 content was fixed at 40%. They pointed out that glass transition temperature increased as the Y_2O_3 content increased, and that Al^{3+} ions assisted the formation of the glass network structure with Y^{3+} acting as a modifying ion. However, few studies have systematically investigated the phase diagram, the separation of the glassy phase, or the crystallization behavior of the ternary system. Other glass systems containing a rare-earth element include Ba-Y-Si-O, which is also attracting attention as a high melting point glass.[6,7]

Li et. al. reported that the Y^{3+} ion in the Ba-Y-Si-O system works as a modifying ion which reinforces the glass bonds by reducing the thermal expansion coefficient and increasing the softening point.[6] Thus, the Y_2O_3-containing glass systems have the potential for industrial importance, but their structures and properties need to be fully understood before they can be widely commercialized.

Regarding the phase diagrams for the systems containing Al_2O_3, Y_2O_3 or SiO_2, the diagram for the pseudo binary system of Al_2O_3-Y_2O_3 has been already reported.[2] Al_2O_3 and Y_2O_3 are the major components of Sialon and oxynitride glass, and the phase diagram for the pseudo ternary system of Al_2O_3-Y_2O_3-Si_3N_4 has been also detailed.[2] Few studies, however, have discussed the ternary Al_2O_3-Y_2O_3-SiO_2 system. Bondar et al. have clarified the liquid-phase temperature,[1] but the detailed phase diagram depicting the solid-phase at high temperatures has not yet been described. In this study, the phases of the Al_2O_3-Y_2O_3-SiO_2 ternary system were investigated as well as the glassy phase separated therefrom and the glass crystallization behavior.

2. Experimental Procedure

2.1. Sample Preparation and Phase Diagram Establishment

The starting materials used in this study were Al_2O_3 (purity 99.9%, average grain size 0.96μm), Y_2O_3 (99.9%, 0.82μm), and SiO_2 (99.99%, 0.94μm). These starting materials were wet mixed in a given ratio in the presence of a solvent, formed into a 10×10×35mm shape under 700kg/mm², and thermally treated at 1300°C for 2hr to produce a compact. The compact was placed in a high-purity alumina crucible, and thermally treated at 1500°C for 5hr in an electric oven, and then quenched, to produce the sample. The compact composition had only a small quantity of the liquid phase and showed no softening by melting at the above temperature; it was further treated for 30hr at the longest, to confirm by X-ray diffraction analysis that it had reached an equilibrium. The crucible showed no loss of weight indicating that there was no reaction with the molten mixture such that the mixture was assumed not to be contaminated by elements from the crucible. The sample thus prepared was cut and polished, and then analyzed by X-ray diffraction analysis to determine the crystalline structures; scanning electron microscope (SEM) analysis and X-ray microanalysis (EPMA) identified the structures and composition to describe the phase and to confirm that the equilibrium was established at 1500°C.

Each sample was DTA analyzed to determine its phase transformation temperature, and to investigate the effects of composition on the phase transformation temperature. Each sample was heated at a rate of 7°C/min in an alumina crucible to a temperature (max=1800°C) approximately
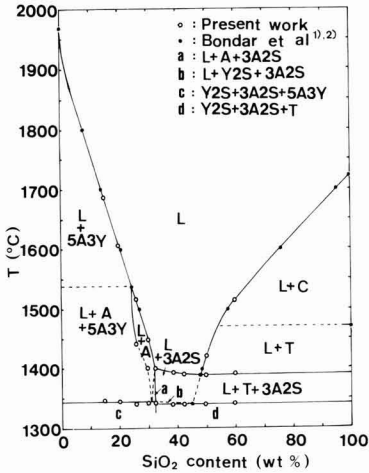
Fig. 1. Phase relation in quasibinary $Al_{1.25}Y_{0.75}O_3$-SiO_2 system.
L: represents liquid phase, C:Cristobalite (SiO_2),
T:Tridymite (SiO_2), 3A2S:Mullite ($Al_6Si_2O_{13}$),
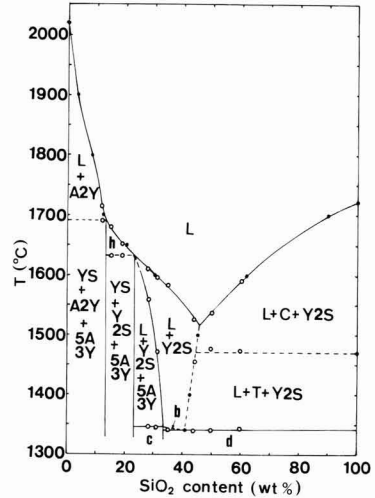Y2S:$Y_2Si_2O_7$, A:Al_2O_3, 5A3Y:Garnet ($Al_{1.25}Y_{0.75}O_3$).

Fig. 3. Phase relation in quasibinary $Al_{2/3}Y_{4/3}O_3$-SiO_2 system (b, c,
d and h show the same phases as those in Figs.1 and 2).

2.2. Formation and Separation of Glassy Phase, and Glass Crystallization Behavior

The calcined sample was melted in an infrared image oven with a halogen lamp as the light source; the molten composition was dropped onto a stainless plate to be quenched, producing the glass sample. The composition exhibiting only a liquid phase at 1500°C was made into glass by quenching it in the oven, as described above. The glass sample of the three-element system was DTA analyzed, at 5°C/min, to investigate the effects of composition on the glass transition temperature, the crystallization initialization, and the peak temperatures. The DTA heating rate was also varied in a range from 3 to 20°C/min to determine the energy of activation from the relationship between the crystallization peak temperature and the heating rate. In order to observe the structural changes during heat induced crystallization, the sample was thermally treated at 1300°C for 2hr. quenched, and then analyzed for changes in the microstructure using SEM back-scattered electron images.
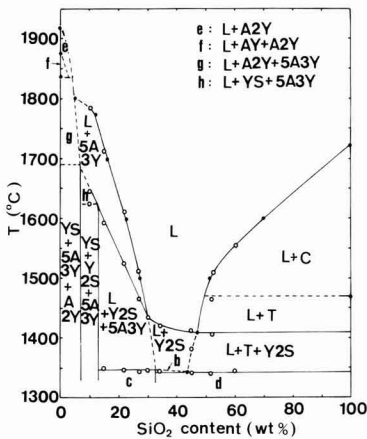

Fig. 2. Phase relation in quasibinary $AlYO_3$-SiO_2 system.
A2Y, AY and YS represent, respectively, $Al_{2/3}Y_{4/3}O_3$, $AlYO_3$ and
Y_2SiO_5 (b, c and d show the same phase as those in Fig.1).

50°C higher than the phase transformation temperature, and then immediately allowed to cool in the oven to identify the high temperature phases. For the compositions which exhibited a phase transformation, the maximum temperature of heating was 1640°C, although the level varied with composition; the cooling rate was approximately 60°C/min. The sample thus prepared was cut, and then analyzed by the methods described earlier to observe the crystalline structures and textures, and to identify the high temperature phase and establish the phase diagram. Most of the compositions contained SiO_2 of 60wt% or less in order to form the glassy phase. All of the contents in the diagram are expressed in wt%.

3. Results and Discussion

3.1. Phase Equilibria of Al_2O_3-Y_2O_3-SiO_2 at High Temperature

The phase diagrams produced corresponded to the four pseudo binary system of $Al_{1.25}Y_{0.75}O_3$-SiO_2, $AlYO_3$-SiO_2, $Al_{2/3}Y_{4/3}O_3$-SiO_2 and $Y_3Si_2O_7$-$Al_6Si_2O_{13}$. **Figures 1 through 4** show the phase diagrams; **Figures 5 and 6** exhibit SEM photographs of the structures. A total of eleven phases appeared in these systems; SiO_2 (cristobalite, hereinafter referred to as "C," existing at 1470° to 1713°C), SiO_2 (tridytmite, "T," existing at 870° to 1470°C), $Y_2Si_2O_7$(Y2S), $Y_4Si_3O_{12}$ (2Y3S, 1775° to 1800°C), Y_2SiO_5 (YS), $Al_{2/3}Y_{4/3}O_3$ ($Al_2O_3 2Y_2O_3$, A2Y), $AlYO_3$ (AY, 1835° to 1875°C), $Al_{.25}Y_{0.75}O_3$ ($5Al_2O_3 3Y_2O_3$, garnet, 5A3Y), Al_2O_3 (A), $Al_6Si_2O_{13}$ (mullite, 3A2S) and a liquid phase (L).

As shown in Fig.1 for the pseudo binary system of $Al_{1.25}Y_{0.75}O_3$-SiO_2, the experimentally determined liquidus
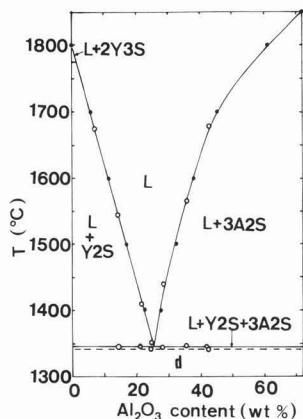
Fig. 4. Phase relation in quasibinary $Y_2Si_2O_7$-$Al_6Si_2O_{13}$ system. 2Y3S represents $Y_4Si_3O_{12}$. In this system, existence of L+Y2S3A2S phase was expected in a temperature range of 1340 ~ 1345°C (d shows the same phase as that in Fig.1).
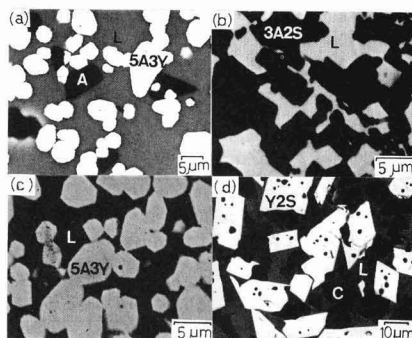

Fig. 5. SEM micrographs (backscattered electron image) of specimens quenched from high temperature.

(a) $(Al_{1.25}Y_{0.75}O_3)_{80}(SiO_2)_{20}$ quenched from L+A+5A3Y region at 1500°C.

(b) $(Al_{1.25}Y_{0.75}O_3)_{62}(SiO_2)_{38}$ quenched from L+3A2S region at 13870°C.

(c) $(AlYO_3)_{85}(SiO_2)_{15}$ quenched from L+5A3Y region at 1640°C.

(d) $(Al_{2/3}Y_{4/3}O_3)_{50}(SiO_2)_{50}$ quenched from L+C+Y2S region at 2500°C.
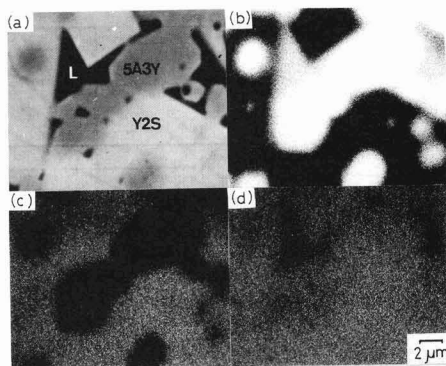

Fig. 6. Micrographs of $(Al_{2/3}Y_{4/3}O_3)_{72}(SiO_2)_{28}$ quenched from L+Y2S+5A3Y region of 1500°C observed by EPMA.

(a) Backscattered electron image, (b) X-ray image of Al, (c) X-ray image of Si, (d) X-ray image of Y.

temperature was in good agreement with that of Bondar et. al.[1] In this system, Al_2O_3 was formed as the initial crystal at an SiO_2 concentration range of 24.5 to 32.3%, with the result that the L+A region appeared. Regions a and b were considered to be the three-phase region; however, they were too narrow to be clearly demarcated from the others. On the low temperature side, compositions in the L+A and L+3A2S regions had an SiO_2 concentration of approximately 31.3 and 45.0wt%, respectively; these were estimated assuming that each solid+liquid region would narrow as the temperature decreased. Support for this assumption was the phase diagram of the ternary system proposed by Bondar et. al., in which the liquid-phase region narrowed as the temperature decreased.[1] In this study, however, the phase boundaries could not be established because the primary crystal, once grown, transformed too slowly at 1400°C to reach equilibrium. The unestablished boundaries are represented by the broken lines in the figure. SiO_2 in the SiO_2-rich region transformed from the cristobalite into the tridymite phase at 1470°C.[2] However, this phase transformation proceeded too slowly to be followed in the DTA analysis. The solidus temperature of the pseudo binary system was 1345°C in Region c where the SiO_2 concentration was 31.2% or less, and 1340°C in Region d with higher SiO_2 concentrations. Region c was considered to be the three-phase Y2S+3A2S+5A3Y region. However in this region, the primary crystals of Al_2O_3 formed at high temperature were grown and were not diminished by the heat treatment at 1300°C for 200hr, with the result that it was difficult to confirm the equilibrium conditions of the region at a solidus temperature of 1345°C or less. Figure 5(a, b) presents the SEM photographs of the L+A+5A3Y and L+3A2S phase, having an SiO_2 concentration of 20 and 38wt%, respectively.

Figure 2 presents the phase diagram of the pseudo binary system of $AlYO_3$-SiO_2. $AlYO_3$ existed at 1835° to 1875°C[2] and hence the three-phase YS+5A3Y+A2Y system was formed on the low temperature side in the region having an SiO_2 concentration of 6.8wt% or less. This region was thought to transform itself into the L+A2Y+5A3Y phase at

1690°C or higher. No clear DTA peak, however, was found at this temperature, thus the peak was estimated using the point at which the liquidus line in the Bondar diagram[1] intersected the YS+5A3Y+A2Y region. Figure 5(c) is the SEM image of the L+5A3Y phase with an SiO_2 concentration of 15wt%, quenched from 1640°C.

Figure 3 shows the phase diagram of the pseudo binary system of $Al_{2/3}Y_{4/3}O_3$-SiO_2. The SEM image of the L+C+Y2S phase, quenched from 1500°C, is shown in Figure 5(d); the EPMA-observed back-scattered electron image of the L+Y2S+5A3Y phase, quenched from 1500°C, is shown in Figure 6(a). In the X-ray image of Al shown in Fig.6(b), the Al-free region is represented by the black portion; in Figure 6(c), the X-ray image of Si, the black portion is the Si-free-region. There is a region low in Y concentration in the X-ray image of Y, shown in Fig.6(d), which corresponds to the glassy phase (marked with an L in
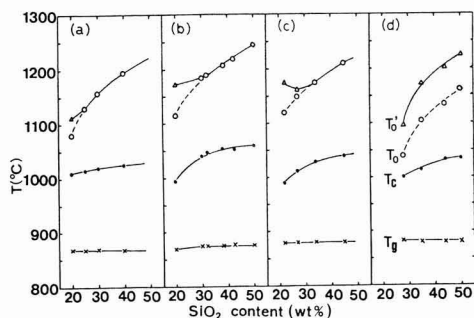
Fig. 7. Composition dependence of glass transition temperature (T_g), starting temperature of crystallization (T_c), the 1st and 2nd peak temperatures of crystallization (T_o and T_o', respectively) of Al₂O₃-Y₂O₃-SiO₂ glasses. (a) Quasibinary Al₁.₃₇₈Y₀.₆₂₂O₃-SiO₂ system, (b) Al₁.₂₅Y₀.₇₅O₃-SiO₂ system, (c) AlYO₃-SiO₂ system, (d) Al₂/₃Y₄/₃O₃-SiO₂ system.
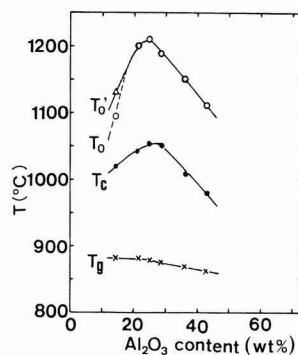

Fig. 8. Composition dependence of glass transition temperature (Tg), starting temperature of crystallization (Tc), the 1st and 2nd peak temperatures of crystallization (To and To', respectively) of Y₂Si₂O₇-Al₆Si₂O₁₃ glasses.

Fig.6(a)) formed from the quenched liquid phase. The X-ray diffraction analysis confirmed that the sample only consisted of Y2S and 5A3Y, and the glassy phase; thus, it was judged that it was the L+Y2S+5A3Y phase.

Figure 4 presents the phase diagram of the pseudo binary system of Y₂Si₂O₇ (Al₂O₃ concentration: 0wt%)-Al₆Si₂O₁₃ (Al₂O₃ concentration: 71.79wt%). Y2S shown in the left side of the figure was decomposed into the L+2Y3S phase at 1775°C or higher[2]; thus, it was expected that the L+2Y3S phase existed in the above temperature range. The eutectic composition of the pseudo binary system was represented by an Al₂O₃ concentration of approximately 25.5wt%, and the eutectic temperature was 1345°C. The region below 1340°C, i.e., the region below the broken line in Fig.4, is considered to be the Y2S+3Y2S phase when equilibrium is reached. In actuality, however, the three-phase Y2S+3A2S+T system was observed at a low temperature, because of the separation of SiO₂ (T) when the liquid phase solidified. It was expected that the L+Y2S+3A2S phase existed between 1345°C (the solid line) and 1340°C (the broken line). The two endothermic peaks overlapped each other in the DTA analysis, and the above phase was not detected even by the X-ray diffraction analysis of the sample quenched from a temperature in the above region.

3.2. Separated Glassy Phase and its Crystallization Behavior

The ternary systems were melted in an infrared image furnace and quenched on a stainless plate in order to confirm the glass-forming region. It was estimated that their melting point was around 1750°C, though this was not confirmed accurately because some of the molten samples were transparent and the others were not depending on their compositions. The glass-forming region determined in this study is shown by the broken line in **Fig.13**, as will be discussed later.

Figure 7 shows relationships between the glass transition temperature T_g, crystallization initiation temperature T_c, and the first and second crystallization peak temperatures T_o and T_o'. as a function of the glass composition, where the samples were of the pseudo binary systems having a constant Al₂O₃/Y₂O₃ ratio, heated by a DTA analyzer at

5°C/min. **Figure 8** shows the results for the pseudo binary systems of Y₂Si₂O₇-Al₆Si₂O₁₃, indicating that T_g was relatively independent of composition, but tended to decrease as the Al₂O₃ content increased. These results were in good agreement with those presented by Oda et. al.[5] T_c and T_o, on the other hand, increased as the SiO₂ content increased, (see Fig.7), and attained a maximum at the eutectic composition, (see Fig.8). Based on the above results coupled with those shown in Figs.1 through 4 for the composition dependence of the liquidus line, it was confirmed that T_c and T_o increased as the liquidus temperature decreased.

In the peripheral portions of the glass-forming region, which are characterized by low concentrations of SiO₂ and Al₂O₃, the crystallization peak temperature was split into two levels, T_o and T_o', suggesting that there were two types of crystals with different activation energies for crystal growth. The relative intensities of the two exothermic peaks observed in the DTA analysis, corresponding to T_o and T_o'., were composition dependent. The first peak was notably intense but the second one was very weak when the composition was high in Al₂O₃ approaching 5A3Y. On the other hand, when the composition was high in Y₂O₃, e.g., near Y2S, the second peak was highly intense, reversing the ratio. These results suggested that the second peak primarily corresponded to the growth of Y2S, whereas the first peak related to the growth of the other crystals, such as 5A3Y. These peaks overlapped each other, and it was difficult to differentiate the crystalline structures clearly by X-ray diffraction analysis, even if each sample was quenched from its peak temperature. X-ray diffraction analysis did confirm that the pseudo binary system shown in Fig.7(d) had separate Y2S and SiO₂ phases in the region containing 30% or more SiO₂; thus, it was concluded that the first peak in an SiO₂-rich composition was mainly attributable to the separation of SiO₂.

Crystallization peak temperatures T_o and T_o' varied with the DTA heating rate α, tending to increase as the heating rate increased. The relationship between T_o and α was determined by varying the heating rate in a range from 3° to 20°C/min. The following modified Kissinger equation[7,8] was used to predict the activation energy ΔE for crystal growth.
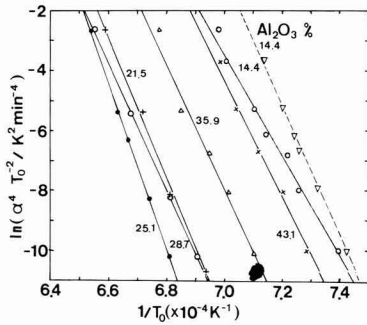
Fig. 9. Modified Kissinger plot showing a relation between heating rate (α, in unit of K/min) and the peak temperature of crystallization (T_o, in unit of K in this figure) in DTA of $Y_2Si_2O_7$-$Al_6Si_2O_{13}$ glasses as a function of Al_2O_3 composition. In a specimen with Al_2O_3 14.4% composition, dotted and real lines represent the 1st and the 2nd peak of crystallization (T_o and T_o', respectively).
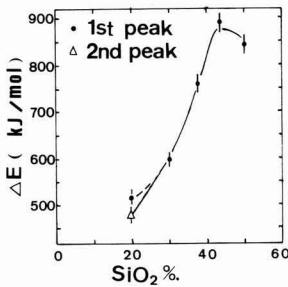

Fig. 10. Activation energy of crystallization ΔE of the quasibinary $Al_{1.25}Y_{0.75}O_3$-SiO_2 glasses as a function of SiO_2 composition. Real and dotted lines represent ΔE corresponded to the growth of different crystal, i.e. probably to that of Y2S and 5A3Y,   respec-

$$\ln(\alpha^n/T_0^2) = -m\Delta E/(RT_0) + \text{const.}$$

where, n and m are constants determined by the crystal growth mechanism.[8]

The values $n=4$ and $m=3$ were used, based on the proposal by Matsushita et al.[8] Since the samples for the DTA analysis contained granules 2 to 4mm in diameter, the grain growth was considered to be controlled mainly by the three-dimensional volumetric crystallization. **Figure 9** shows the relationship between α and T_o for the pseudo binary system $Y_2Si_2O_7$-$Al_6Si_2O_{13}$. For the sample with 14.4wt% Al_2O_3, the solid and broken lines represent dependence of α on To' and To, respectively.

Figure 10 and 11 show the dependence of the activation energy ΔE on composition for the $Al_{1.25}Y_{0.75}O_3$-SiO_2 and $Y_2Si_2O_7$-$Al_6Si_2O_{13}$ systems, respectively, where activation energy for grain growth was estimated from the T_o (or T_o') $- \alpha$ relationship. The ΔE value attained a maximum at an SiO_2 content of approximately 43% for the former system, and at the eutectic composition (Al_2O_3 content approximately 25.5wt%). It was found, by comparing the phase diagrams, that the glassy phase, exhibiting a lower liquid-phase temperature, had a higher ΔE level, and tended to be more stable. Furthermore, for the sample containing 14.4wt% Al_2O_3 shown in Fig.9, the solid line ($T_o' - \alpha$
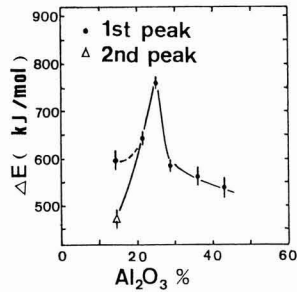

Fig. 11. Activation energy of crystallization ΔE of the quasibinary $Y_2Si_2O_7$-$Al_6Si_2O_{13}$ glasses as a function of Al_2O_3 composition. Real and dotted lines represent ΔE corresponded to the growth of different crystals, i.e. probably to that of Y2S and SiO_2 , respectively.

relationship) was shifted to the high temperature side from the broken line ($T_o - \alpha$ relationship), and was more dependent on α, indicating that the second peak had a lower activation energy than the first peak. One of the reasons for this phenomenon might have been the enhanced grain growth of Y2S, based on the fact that the 5A3Y grains in the glassy phase grew preferentially to reduce the Al_2O_3 content around them. Crystallization of a glass is generally a very complicated process (e.g., energy of activation for crystal growth is different on the surface than in the glass interior), and further investigations are needed to clarify the crystallization mechanism.

It was observed in this study that ΔE of the pseudo binary $Y_2Si_2O_7$-$Al_6Si_2O_{13}$ system attained a maximum at the eutectic composition Kozuka et. al., reported that the difference between the crystallization initiation temperature and the glass transition temperature, $T_c - T_g$, could be used as a parameter to represent the stability of glass against crystallization of the glass.[7] For the pseudo binary system prepared in this study, the maximum difference was close to the eutectic composition, as shown in Fig.8. These results suggested that the net work of glass was the strongest at the eutectic composition and that the activation energy for the atomic diffusion increased as it approached the eutectic composition. Assuming that the free energy, F_g, of the glassy phase generally decreases as liquidus temperature decreases, as is the case for the liquid phase, the difference between the free energies of the glass and the crystal phases $\Delta F = F_g - F_c$ increases as the composition deviates from the eutectic composition; concurrently the activation energy for the diffusion process decreases, and hence ΔE decreases.

Hyatt et. al.[9] pointed out that a phase separation occurred in a composition similar to the ternary system prepared in this study, but details were not given. In an attempt to confirm the presence of the separated phase in this ternary glass system, the sample was thermally treated at 1300°C for 2hr and then quenched, and the structures were observed by a scanning electron microscope. The back-scattered electron images are given in **Fig.12**, indicating that phase separation occurred extensively throughout the glass-forming region. Figure 12(a), a photograph of the central part of the glass-forming region, shows the separted phases entwined with each other in a complicated manner, indicating a possible phase separation via spinodal decomposition. The region just off the central part (Fig.12(b)) shows a
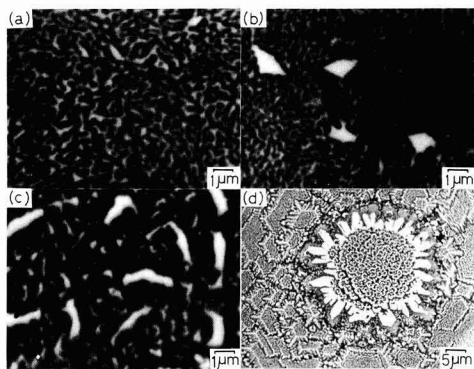
Fig. 12. SEM micrographs (backscattered electron image) of Al_2O_3-Y_2O_3-SiO_2 glasses annealed at 1300°C for 2hr.
(a)$(Al_2O_3)_{25}(Y_2O_3)_{32.5}(SiO_2)_{42.5}$, (b)$(Al_2O_3)_{21.54}(Y_2O_3)_{45.69}(SiO_2)_{32.77}$,
(c)$(Al_2O_3)_{21.47}(Y_2O_3)_{28.52}(SiO_2)_{50.01}$, (d)$(Al_2O_3)_{22.5}(Y_2O_3)_{57.5}(SiO_2)_{20}$.

Fig. 13. Phase separation and crystallization behavior of Al_2O_3-Y_2O_3-SiO_2 glasses annealed at 1300°C for 20hr as a function of composition. Dotted line shows glass-forming region obtained in this work.
●:decomposition probably by spinodal mechanism,
○:classical decomposition by nucleation and growth mechanism,
▲:decomposition suggesting the coexistence of both mechanisms,
△:dendritic growth of crystals in glass.

separated phase with an island-like, coarse texture in addition to the structures shown in Fig.12(a). This indicated that a spinodal type decomposition and a classical decomposition occurred simultaneously, the latter being caused by the formation and growth of nuclei. Figure 12(c), a photograph of the peripheral portion of the this region, shows the separated phases isolated from each other, some being fine and granular and others being coarse, indicating a classical phase separation caused by the formation and growth of nuclei. It is known that the concentration-modulated wavelengths of the decomposed structures vary depending on heat treatment temperature,[10] thus it is necessary to clarify the phase separation mechanisms involved in the ternary systems prepared in this study. Generally speaking, a region richer in elements with a large atomic number will be brighter in a back-scattered electron image. The dark portions in Fig.12, therefore, represented the regions rich in SiO_2 or Al_2O_3, and bright portions represent the regions rich in Y_2O_3; moreover, the glassy phase was probably separated into Y_2O_3-rich and Y_2O_3-deficient compositions. Figure 12(d) is a photograph of the sample with a Y_2O_3-rich composition at the border of the glass-forming region, where crystals were grown into a dendrite-like crystals forming cellular structures. It was also observed that some regions at the border of this region were fine in texture like those shown in Fig.12(c) when they were sufficiently low in Y_2O_3 content. Figure 13 shows the phase diagram constructed from the above results, where those compositions marked with ●'s represent the structures believed to be formed by the spinodal type decomposition, those with ○'s represent the structures formed by a classical decomposition, and those with ▲'s represent the structures formed by the two mechanisms. The compositions marked with △'s are those showing the dendrite-like crystal growth. The fine structures became coarse and deformed when the sample was heat-treated for a sufficiently long time, indicating the progress of crystallization. The phase separation, therefore, occurred during the initial stage of crystallization of the glassy phase.

It has been reported that there are uneven mixtures in the liquid-phase of the binary system of Y_2O_3-SiO_2, when the
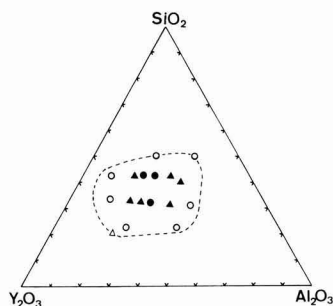
SiO_2 content is in a range between roughly 45 to 95wt%.[2] Moreover, a spinodal type decomposition is reported to occur in the glassy phase produced by quenching the binary ceramic system of Al_2O_3 and SiO_2, when its SiO_2 content is in a range between roughly 40 to 70wt%.[11,12] That is, the separation of SiO_2 from Y_2O_3 or Al_2O_3 tends to reduce the energy. This can account for, at least partly, the phase separation observed in the ternary systems prepared in this study.

4. Conclusions

An attempt was made to establish the phase diagrams of the ternary systems of Al_2O_3-Y_2O_3-SiO_2 and to clarify the properties of their glass phases by investigating the phase equilibria, the separation of the glassy phase, and the crystallization behavior of the four types of pseudo binary systems of $Al_{1.25}Y_{0.75}O_3$-SiO_2, $AlYO_3$-SiO_2, $Al_{2/3}Y_{4/3}O_3$-SiO_2 and $Y_2Si_2O_7$-$Al_6Si_2O_{13}$.

1) The phase equilibria of the above pseudo binary systems at high temperature near the liquidus temperature were established. Their liquidus temperatures were in agreement with those proposed by Bondar, et. al.[1] The lowest solidus temperature observed for these systems was 1340°C, below which no phase equilibrium was confirmed due to the long periods of time which were required to reach equilibrium.

2) The glass transition temperature of the Al_2O_3-Y_2O_3-SiO_2 systems was in a range from 865° to 885°C. It tended to decrease as the Al_2O_3 content increased, but no noticeable dependence on the SiO_2 content was observed. Their crystallization initiation temperature and peak temperature were in a range from 990° to 1060°C and from 1040° to 1245°C, respectively, each tending to increase as the liquidus temperature of the composition decreased. The compositions low in SiO_2 and Al_2O_3 had two crystallization peak temperature levels, and hence two types of crystals of different activation energies of crystal growth.

3) The activation energy ΔE for crystal growth was in a

range from 472 to 890kJ/mol. It was estimated by analyzing the dependence of the crystallization peak temperature on the heating rate, using the modified Kissinger equation. ΔE tended to increase for the composition having a lower liquidus temperature, and the glassy phase became more stable as the liquidus temperature decreased. The activation energy of the pseudo binary systems of $Y_2Si_2O_7$-$Al_6Si_2O_{13}$ attained a maximum at the eutectic composition.

4) Phase separation occurred during the initial stage of crystallization, when the glassy phase was thermally treated at 1300°C.

References:

1) I.A. Bondar and F.A. Garakhov, Izv. Akad. Nauk SS SR. Ser. Khim. 2. 1325-26 (1963).

2) Phase Diagram for Ceramists, the American Ceramic Society, Columbus, Ohio, Vol.1, (1964) pp.122-123, Vol.2 (1969) pp.95-165, Vol.5, (1983) pp.308-11.

3) A. Makishima, Y. Tamura and T. Sakaino, J. Am. Ceram. Soc., 61, 249-49 (1978).

4) A. Makishima and T. Shimohira, J. Mon-cryst. Solids, 38, 661-66 (1980).

5) K. Oda and T. Yoshio, Seramikkusu Ronbun-shi, 97, 1493-97 (1989).

6) Y. Li, H. Kozuka, and S. Sakka, Yogyo Kyokai-shi, 95, 538-45, (1987).

7) H. Kozuka, Y. Li, and S. Sakka, Zairyo, 37, 1216-22 (1989).

8) K. Matsuhita and S. Sakka, J. Non-cryst, Solids, 38, 741-46 (1980).

9) M.J. Hyatt and D.E. Day, J. Am. Ceram. Soc., 70, C288-87 (1987).

10) Y. Moriya, Glass handbook, Asakura Shoten, (175), pp.793-805.

11) J.F. McDowell and G.H. Beall, J. Am. Ceram. Soc., 52, 17-25 (1969).

12) S.H. Risbud and J.A. Pask, J. Am. Ceram. Soc., 60, 418-24 (1977).

Sensibility of the Bi-Pb-Sr-Ca-Cu-O Superconductive Films in Weak Magnetic Fields

Keizou Tsukamoto, Hiromasa Shimojima, Mamoru Ishii and Chitake Yamagishi

Central Research Laboratory, Nihon Cement Co. Ltd.,
1-2-23 Kiyosumi koutouku Tokyo 135

Bi-Pb-Sr-Ca-Cu-O superconductive films with various T_c (65~105K) and various J_c (0~155A/cm^2 at 77K) were obtained by annealing thin films prepared by rf-magnetron sputtering at 823~850°C for 110hr. High T_c and low J_c films showed high magnetic sensibility. Especially, the magnetic sensibility of the film annealed at 844°C was 1.87mV/gauss at 77.3K. However, the magnetic sensibility of the film with higher J_c(155A/cm^2) which was obtained by annealing at 850°C was low. The magnetic sensibility was high for the films with plate-like crystals partially parallel and partially perpendicularly oriented to the MgO substrate(mixed morphology). On the other hand, films composed of almost oriented plate-like crystals showed low magnetic sensibilities. It is considered that the invaded flux in the film with mixed morphology was very motive because of the weak-link grain boundaries.

1. Introduction

It is known that grain boundary phases exist in superconducting oxides including those of the Bi(Pb)-Sr-Ca-Cu-O system.[1] Many of these phases act as inter-granular weak links in sintered bodies, and greatly affect their superconductive properties (critical current density and critical temperature) in the presence of a magnetic field.[2-4]

When an external magnetic field is applied to a superconductor, a magnetic flux less than the lower critical field (H_{c1}) can easily penetrate a grain boundary phase. This flux is moved by a Lorentz force or thermal agitation, generating resistance in the superconductor.

The application of these changes in superconductive properties by the application of a magnetic field is under study in an attempt to adapt superconductive oxides for uses such as magnetic[5-8] and microwave detectors.[9-10] These detectors operate on a change in the resistance of a superconductor induced by applying a magnetic or microwave field while passing a constant current through the polycrystalline superconductor.

Magnetic detectors utilizing changes in resistance excel in sensibility to a magnetic field (resistance change induced by the external applied field) compared to other sensors based on InSb semiconductors currently on the market, thus their practical use is highly anticipated.

In this study, relationships between the sensibility to the magnetic field and the critical temperature, the critical current density, and the film microstructures have been examined for superconductive polycrystalline thin films obtained by annealing sputtered thin films of Bi-Pb-Sr-Ca-Cu-O.

2. Experimental Procedure

2.1. Preparation of Thin Films

Bi-Pb-Sr-Ca-Cu-O thin films were prepared on commercial MgO single crystal substrates by rf magnetron sputtering using multitargets.

① $Bi_{0.5}Pb_{0.5}O_x$ (Bi_2O_3/PbO powder mixture)
② $CaCu_{0.75}O_x$ ($CaCO_3$/CuO powder fired at 950°C)
③ $SrCu_{0.75}O_x$ ($SrCO_3$/CuO powder fired at 950°C)

In preparing the thin films, Bi-Pb-O/Ca-Cu-O/Sr-Cu-O layers were stacked in order by sputtering ①, ②, and ③.[11-13] Their compositions were controlled by adjusting the sputtering time for each target. In this experiment, sputtering times were of ① 6 seconds, ② 59.5 seconds, and ③ 34.5 seconds, repeated 400 times.

The thickness of each film deposited in a single cycle of each target was 5nm; the total sample thickness reached 2μm in the end. The prepared thin films were amorphous and thus nonsuperconductive, and therefore were subjected to annealing.

2.2. Annealing of Thin Films

A two-step annealing was adopted whereby samples were heated at 780°C for 2 hours as the primary annealing, followed by heating at 823°~850°C for 110 hours as the secondary annealing. The thin films were heated quickly to the primary annealing temperature, maintained for 2 hours, and then quenched. Subsequently, they were quickly reheated to the secondary annealing temperature, held for a specified period of time, and then cooled in the furnace to room temperature. The thin films were annealing in an alumina boat together with $Bi_{0.96}Pb_{0.24}SrCaCu_{1.6}O_x$ pellets.

2.3. Evaluation of Thin Films

The compositions of the obtained thin films were analyzed by EPMA; the crystalline phases were determined by XRD. The volume fraction of high T_c phases was calculated from the intensity ratio of the (002) reflections lines of the obtained XRD patterns.[11-13]

The resistance of the thin films was measured using the conventional four terminal method. The critical current density was measured at 77.3K in a zero magnetic field using the current value when the output voltage exceeded 1μV (terminal distance: 2mm). The critical temperature was the temperature at which the resistivity of the films
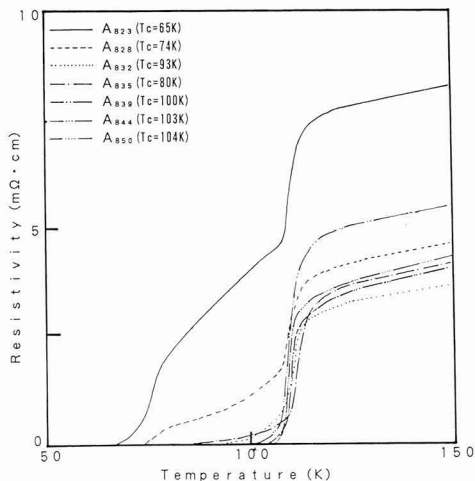
Fig. 1 Temperature dependence of the resistivity for the films.

Table 1. Critical temperature and critical current density (critical curent) of the annealed films.

Annealing temp. (℃)	823	828	832	835	839	844	850
Tc (K)	65	74	93	80	100	103	104
Ic at 77. 3K (mA)	0. 0	0. 0	0. 7	0. 1	0. 4	3. 0	8. 0
Jc at 77. 3K (A/cm²)	0	0	14	2	7	71	155

attained a value on the order of $10^{-6}\Omega cm$. Samples of microstructures were observed by SEM.

The sensibility to the magnetic field was measured by applying an external field to a sample placed in a Helmholtz coil after generating a field of 0-10 gauss by passing a direct current of 0-100mA through the Helmholtz coil. The field was applied vertically to the film surface. During measurement, a constant current was applied to the film and the output voltage, which varied according to an increase in the external field, was measured using the conventional four-terminal method. Samples were oblong thin films 8mm long and 3mm wide, with silver wires bonded using silver paste to 0.5mm spots of deposited gold in 2mm intervals, to serve as current and voltage electrodes.

3. Experimental Results

3.1. Critical Temperature and Critical Current Density of Thin Films

The composition of the obtained thin films was $(Bi+Pb)_{1.00}Sr_{1.00}Ca_{0.96}Cu_{1.95}O_x$ by EPMA analysis. The thin films were subjected to a two-step annealing to form superconducting thin films. Their resistivity was measured in a cryostat (**Fig.1**). **Table 1** shows the critical temperatures of these thin films and the critical current densities (critical current values) measured in liquid N_2.
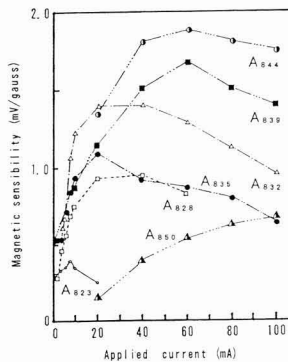

Fig. 2 Relation between the sensibility in the weak magnetic field and the applied current.
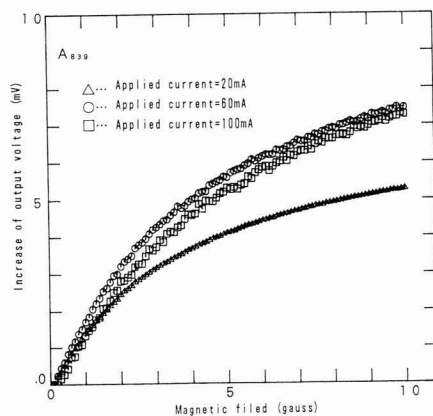

Fig. 3 Sensibilty curve in weak magnetic field of the A₈₃₉ film.

3.2. Dependence of Sensibility to the Magnetic Field on Applied Current Values

The obtained thin films were used to measure the sensibility to the magnetic field for external fields in the range 0-10 gauss and applied currents of 2-200mA.

The sensibility to the magnetic field of each thin film varied with the current applied.

Figure 2 shows the relationship between the sensibility to the magnetic field and the applied current. Additionally, the dependence of the output voltage difference on the magnetic field was almost the same for each thin film. **Figure 3** presents the typical results of this measurement for a thin film treated at 839°C (hereinafter referred to as A₈₃₉, indicating the secondary annealing temperature).

In the figure, the gradients of field dependent curves of the output voltage difference in the range of 0-2 gauss were different from those in the range of 2-10 gauss.

Consequently, sensibility to the magnetic field was represented by the average slope in the weak field range from 0 to 2 gauss where the relationship was almost linear.

In each thin film, the sensibility increased with an increase in applied current, up to an applied current value providing the maximum sensibility; for currents exceeding this value, the sensibility showed a slight decrease.

Table 2. Relation between the applied current and critical current density.

Film	Max, sensibility (mV/gauss)	Applied current I (mA)	$\dfrac{I}{Ic}$
A_{823}	0.39	8	∞
A_{828}	0.94	40	∞
A_{832}	1.40	40	57
A_{835}	1.08	20	200
A_{839}	1.68	60	150
A_{844}	1.87	60	20
A_{850}	0.66	100	13
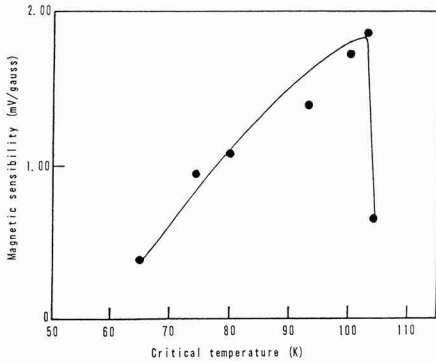
Fig. 4 Relation between the sensibility in the weak magnetic field and the critical temperature.

Moreover, the value of the applied current providing the maximum sensibility for each thin film was much higher than the critical current value (**Table 2**).

The improvement of the sensibility to the magnetic field with an increase in applied current was probably due to a mechanism in which the Lorentz force is heightened by an increasing applied current, which activates the movement of the intruding magnetic flux.

3.3. Dependence of Sensibility to the Magnetic Field on Critical Temperature and Critical Current Density
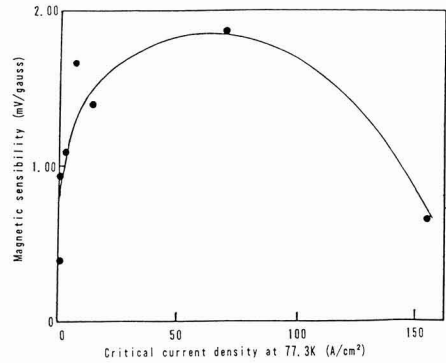
Figures 4 and 5 present the relationships between the sensibility to the magnetic field and the critical temperature or the critical current density for the obtained thin films.

The sensibility to the magnetic field of all the samples, except for the A_{850} thin film treated at its critical temperature (850°C), increased until the maximum value (1.87m/gauss for the A_{844} thin film) was reached. The A_{850} thin film, with a high critical current density, exhibited a lower sensibility in spite of a high critical temperature.

The above results suggest that a thin film with a high critical temperature and a moderate critical current density (on the order of 50-100A/cm^2) exhibits a high sensibility to the magnetic field.

Superconductive polycrystalline thin films can be classified into three kinds of bonding states ((1)-(3)) for their superconducting particles in terms of critical temperature, critical current density and magnetoelectric conversion efficiency.

1) Critical temperature <77.3K
   →No bonding among superconductive particles

Fig. 5 Relation between the sensibility in the weak magnetic field and the critical current density.

    (low sensibility to the magnetic field)
2) Critical temperature >77.3K
   Critical current density: Low
   →Weak bonding among superconductive particles
   (high sensibility to the magnetic field)
3) Critical temperature >77.3K
   Critical current density: High
   →Strong bonding among superconductive particles
   (low sensibility to the magnetic field)

3.4. Crystalline Phases of Thin Films

Figure 6 shows the XRD patterns of the thin films after annealing. With a rise in the secondary annealing temperature, the intensity of the Ca$_2$PbO$_4$ diffraction line (CP in Fig.6) decreased, while that of the high T$_c$ phase increased. Moreover, as the secondary annealing temperature increased, the (001) diffraction line of the high and low T$_c$ phases became stronger; in particular, the A$_{850}$ thin film was substantially oriented in the c-axis direction, (by contrast, the intensity of the (200) diffraction line decreased).

A sweeping statement should not be made because of possible influences by the critical temperature and the critical current density, but when the superconducting crystal was sufficiently oriented along its c-axis, the sensibility to the magnetic field showed a decrease, not an increase. This indicates that the orientation of superconducting crystals (plate like crystals) promotes bonding among the crystals causing an intruding magnetic flux which is different from that in the case for weak magnetic bonding among crystals, thus affecting the sensibility to the magnetic field.

3.5. SEM Observation and EPMA Analysis of Thin Films

Figure 7 shows the SEM photographs of the thin films after secondary annealing at various temperatures. **Table 3** lists the results of the EPMA analysis of the thin films and their constituent particles after the secondary annealing.

The (Bi + Pb) content of thin films decreased with an increase in the secondary annealing temperature, which suggested the evaporation of Pb (0.97 →0.68). Moreover, in the case of a low secondary annealing temperature, Ca$_2$PbO$_4$ (needle like crystals) remained before full decomposition.

In the A$_{823}$~A$_{844}$ thin films, some plate like crystals were observed vertical to the substrate, while in A$_{850}$ film, they showed further c-axis orientation. This agreed with the XRD results which indicated that higher secondary anneal-
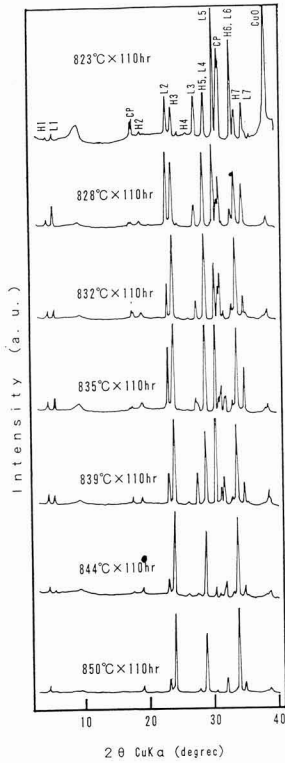
Fig. 6 XRD patterns of the annealed films.
H: $Bi_2Sr_2Ca_2Cu_3O_x$
L: $Bi_2Sr_2Ca_1Cu_2O_x$
CP: Ca_2PbO_4
H1: (002), H2: (008), H3: (0010), H4: (115), H5: (0012),
H6: (200), H7: (0014), L1: (002), L2: (008), L3: (115),
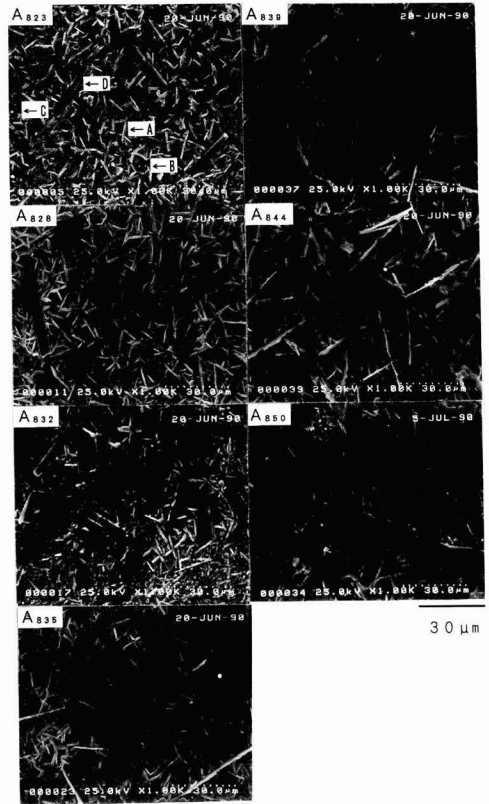L4: (0010), L5: (157), L6: (200), L7: (0012)

Fig. 7 SEM photographs of the annealed films.
A: Plate-like crystal ($\perp$)
B: Plate-like crystal (//)
C: Spherical crystal
D: Needle-like crystal

Table 3. EPMA analysis of the annealed films.

Film	Bi+Pb	Sr	Ca	Cu	Grain in the annealed film	Bi+Pb	Sr	Ca	Cu
	1.00	1.00	0.96	1.95					
A_{823}	0.97	1.00	0.93	1.31	Plate-like crystal ($\perp$)*	0.91	1.00	0.76	1.23
					Plate-like crystal (//)**	0.84	1.00	0.93	1.45
					Spherical crystal ***	0.98	1.00	0.86	1.08
					Needle-like crystal****	2.88	1.00	4.64	0.88
A_{828}	0.97	1.00	0.88	1.36	($\perp$,//)、Spherical、Needle-like				
A_{832}	0.91	1.00	0.93	1.46	"				
A_{835}	0.71	1.00	0.90	1.65	($\perp$,//)、Needle-like				
A_{839}	0.74	1.00	0.89	1.48	($\perp$,//)				
A_{844}	0.71	1.00	0.96	1.73	"				
A_{850}	0.68	1.00	0.88	1.51	(//)				

*Plate-like crystal ($\perp$) ···high Tc phase and low Tc phase
**Plate-like crystal (//) ···high Tc phase and low Tc phase
***Spherical crystal ···Cu poor crystal
****Needle-like crystal···Ca_2PbO_4

ing temperatures offer improved c-axis orientation.

The A_{839} and A_{844} thin films with high sensibility to the magnetic field were composed of the plate like crystals vertical to substrate and c-axis oriented crystals. On the other hand, the A_{850} thin film consisting of oriented plate like crystals had a low sensibility to the magnetic field. In addition, films with an impurity phase (Ca_2PbO_4 needlelike crystals or Cu-deficient spherical crystals) had low sensibility to the magnetic field.

From the results the following relationships ((4)-(6)) are considered to be established between the microstructures of the thin films and the sensibility to the magnetic field.

4) Microstructure of Thin Film:

     impurity phase + plate like crystals $(//,\perp)^*$

     $\rightarrow$ low conversion efficiency

5) Microstructure of Thin Film:

     plate crystals $(//, \perp)$

     $\rightarrow$ high conversion efficiency

6) Microstructure of Thin Film:

     plate crystals $(//)$

     $\rightarrow$ low conversion efficiency

*Plate crystals $(//)$: Crystals oriented to the substrate;

Plate crystals $(\perp)$: Crystals vertically oriented the substrate

4. Conclusions

Bi-Pb-Sr-Ca-Cu-O superconducting thin films were prepared by rf magnetron sputtering to study the relationships between their sensibility to the magnetic field and critical temperature, critical current density, and film microstructures. The obtained results are as follows:

1) The sensibility to the magnetic field was high in the case of films with high critical temperature and moderate critical current density (about 50A/cm^2).

2) The sensibility was also high when the film microstructure was composed of a mixture of superconducting plate like crystals c-axis oriented and vertically oriented to the substrate. In contrast, the sensibility was low in the case of films with impurity phases or advanced c-axis orientations.

References:

1) H. Maeda, Y. Tanaka, M. Fukutomi, and T. Asano, Jpn. J. Appl. Phys., 27, L209-210 (1988).

2) M. Miura, H. Kumakura, K. Togano, and H. Maeda, Appl. Phys. Lett., 54, 1582-1584 (1989).

3) T. Hikata, T. Nishikawa, M. Mukai, K. Sato, and H. Hitotsuyanagi, J. Appl. Phys., 28, L1204-1206(1989).

4) T. Hikata, K. Sato, and H. Hitotsuyanagi, J. Appl. Phys., 28, L82-84(1989).

5) H. Nojima, S. Tsuchimoto, and S. Kataoka, Jpn. J. Appl. Phys., 27, 746-750 (1988).

6) S. Tsuchimoto, E, Ohno, and H. Nojima, J. Japan Society of Powder and Powder Metallurgy, 36, 11-14 (1988).

7) H. Nojima, S. Kataoka, S. Tsuchimoto, M. Nagata, R. Kita, H. Shintaku, E. Ohno, and N. Hashizume, IEDM Tech. Digest, 12.7, 892-893 (1988).

8) N. Yotsuya et. al, Annual Spring Proceedings of Oyo Butsurigakkai, (1990),127.

9) J. Yoshisato, A.Takeoka, T.Ikemachi, K.Niki, T.Yokoo, S.Nakano, and Y.Kuwano, Jpn. J. Appl. Phys., 29, (1990), 1080-1085.

10) J. Yoshisato, EMC, 26, 96-99 (1990)

11) K. Tsukamoto, H. Shimojima, and C. Yamagishi, Nihon Seramikkusu Kyokai Gakujutsu Ronbun-shi, 98, 1039-1044 (1990).

12) K. Tsukamoto, H. Shimojima, M. Ishii, and C. Yamagishi, Japan Society of Powder and Powder Metallurgy, 37, 813-816 (1990).

13) K. Tsukamoto, H. Shimojima, and C.Yamagishi, J. Mater. Sci., 26, 1321-1326 (1991).

Preparation of ZrSiO₄ Powder via the Sol-Gel Process (Part 5)

Toshiyuki Mori, Hirokuni Hoshino, Yoshimitsu Ishikawa, Teiji Yamaguchi, Hiroshi Yamamura, Hidehiko Kobayashi*, and Takashi Mitamura*

Advanced Materials Research Laboratory, TOSOH Co., Ltd.

2743-1 Hayakawa, Ayase-shi 252, Japan

*Dept. of Applied Chemistry, Faculty of Engineering, Saitama University 255 Shimo-ohkubo, Urawa-shi 338, Japan

ZrSiO₄ fine powders were prepared from zirconium oxychloride (ZrOCl₂) and colloidal silica (SiO₂). Effects of the concentration of ZrOCl₂, calcination temperature, heating rate and secondary particle size in hydrolysis solutions on the preparation of ZrSiO₄ fine powders have been studied. The ZrSiO₄ precursors having Zr-O-Si bond were found in all the solutions after hydrolysis, and formation rate of ZrSiO₄ was influenced significantly by the concentration of ZrOCl₂. Also the rate in the case of other concentrations than 0.4M was affected remarkably by heating rate, and there was a marked tendency for crystallization of ZrO₂ and SiO₂ to proceed preferentially and creation of ZrSiO₄ nucleus to be obstructed when the heating rate was slow. It was obvious that ZrSiO₄ fine powders of the single phase could be prepared at a relatively low temperature such as 1300°C by forming the ZrSiO₄ precursors having Zr-O-Si bond and controlling the secondary particle size after hydrolysis.
[Received September 25, 1990; Accepted November 19, 1990]

1. Introduction

Zircon (ZrSiO₄) has been attracting attention mainly as a refractory material, due to its low thermal expansion coefficient[1] and thermal conductivity.[2-4] Furthermore, it is expected to be highly applicable, together with sintered mullite (3Al₂O₃ · 2SiO₂) at high temperatures. Unfortunately, it is difficult to synthesize high-purity zircon powder.

The synthesis of zircon powder from zirconium oxychloride and tetraethyl silicate (Si(OC₂H₅)₄) has been discussed.[5-9] The authors have previously discussed the effects of heating rate and ZrSiO₄ seed types on zircon yield,[10] as well as the factors involved in the formation of the precursor.[11] In this study, several factors affecting zircon yield were investigated related to the synthesis of high-purity zircon powder from zirconium oxychloride and colloidal silica.

2. Experimental Procedure

The starting materials were zirconium oxychloride

(TOSOH) and colloidal silica (concentration: 20wt%, Nissan Kagaku). An aqueous solution of zirconium oxychloride (0.2 to 1.7M) was mixed with an equimolar amount of colloidal silica; the mixture was refluxed to hydrolyze the zirconium oxychloride, and then dried to prepare the starting powder.

The powder thus prepared was fired at 700°C, and then calcined at specified temperature (900° to 1350°C) to prepare the zircon powder.

The zircon powder was analyzed by X-ray diffraction analysis to identify and to analyze quantitatively the product crystalline phase. The size and shape of the primary and secondary particles were observed by a scanning electron microscope (SEM) and transmission electron microscope (TEM). A quantitative analysis by X-ray diffractometry was carried out using the following equation with the diffraction lines of the (101) plane of the tetragonal phase of zirconia, the (111) plane of the monoclinic phase of zirconia, the (111) and (111) planes of monoclinic zirconia, and (200) plane of zircon:[5,6]

Ziron yield α_{ZrSiO4} was calculated from the diffraction line area of the (200) plane of zircon divided by (the diffraction line area of the (200) plane of zircon the diffraction line are of the (101) plane of tetragonal zirconia + the diffraction line areas of the (111) and (111) planes of monoclinic zirconia).[5,6] The size of the secondary particles of the hydrolyzed sol was determined by a NICOMP analyzer (Pacific Scientific Instrument Div., Model 370) equipped with an Ar ion laser as the light source, to investigate the mechanisms involved in the zircon synthesis.

The formation of the zircon precursor was assessed by the presence of the Zr-O-Si bound using FT-IR 400 to 4000cm⁻¹) and X-ray diffraction analysis. In addition, several factors which affected the synthesis of zircon were investigated.

3. Results and Discussion

3.1. Effects of Zirconium Oxychloride Concentration on Zircon Synthesis

The equimolar mixture of zirconium oxychloride and colloidal silica was treated to hydrolyze the zirconium oxychloride, and then sintered at a specified temperature (900°, 1200°, 1300° or 1350°C) for a given period of time (1, 2, 4 or 8hr); the heating rate was 1°C/min.

Figure 1 shows the effects of holding time on zircon yield, for zirconium oxychloride starting concentrations of (a) 0.2, (b) 0.4, (c) 0.8 and (d) 1.7M. The zircon yield increased as the zirconium oxychloride concentration in-
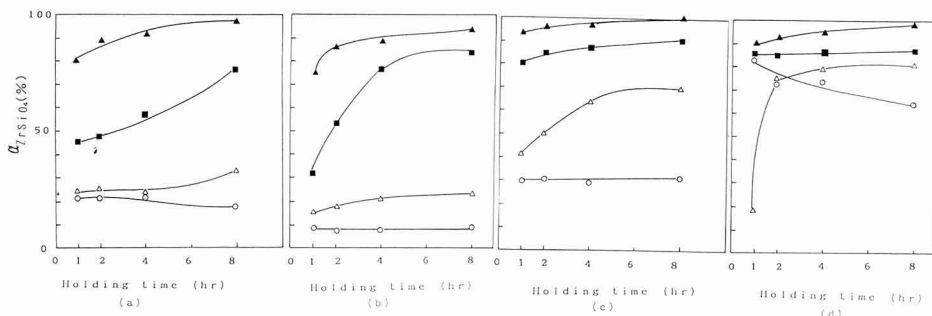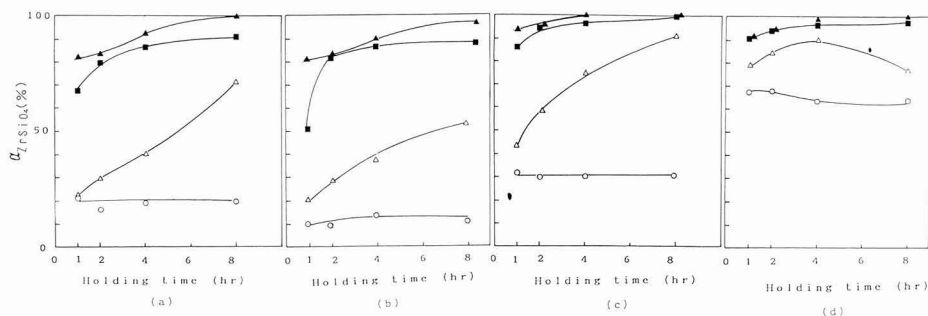
Fig. 1. Formation rate of zircon (α_{ZrSiO4}) as a function of holding time at various temperature.
(a) 0.2M of ZrOCl$_2$, (b) 0.4M of ZrOCl$_2$, (c) 0.8M of ZrOCl$_2$, (d) 1.7M of ZrOCl$_2$ (Heating rate: 1°C/min)
($\bigcirc$: 900°C, $\triangle$: 1200°C, $\blacksquare$: 1300°C, $\blacktriangle$: 1350°C)

Fig. 2. Formation rate of zircon (α_{ZrSiO4}) as a function of holding time at various temperatures.
(a) 0.2M of ZrOCl$_2$, (b) o.4M of ZrOCl$_2$, (c) 0.8M or ZrOCl$_2$, (d) 1.7M of ZrOCl$_2$, (Heating rate: 20°C/min)
($\bigcirc$: 900°C, $\triangle$: 1200°C, $\blacksquare$: 1300°C, $\blacktriangle$: 1350°C)

creased at a relatively low temperature of 900°C, but did not always depend on the concentration at 1200°C or higher temperatures. It was found to be the maximum with a concentration of 0.8M.

It was also noted that zircon yield was very high for the powder synthesized from 1.7M zirconium oxychloride and sintered at 900°C, however, the yield decreased as the holding time increased. X-ray diffraction analysis of the product from 1.7M zirconium oxychloride, sintered at 900°C for 1hr, showed that it contained only small quantities of uncrystallized zirconia and silica. Thus, the high zircon yield could be associated with the reaction of uncrystallized zirconia and silica starting materials, and the decrease in the zircon yield with holding time due to the presence of fairly large quantities of crystallized zirconia and silica which failed to react.

3.2. Effects of Heating Rate on Zircon Yield

The crystallization of the unreacted zirconia and silica starting materials was considered to be one of the factors decreasing the zircon yield, as discussed in Section 3.1. Therefore, an attempt was made to increase the zircon yield by sintering the starting mixture at a higher heating rate to control the crystallization of the starting materials. **Figure 2** shows the results of similar tests, but at a higher heating rate of 20°C/min.

As shown from comparison with Fig.1, increasing the heating rate clearly increased the zircon yield at each zirconium oxychloride concentration, and only the single-
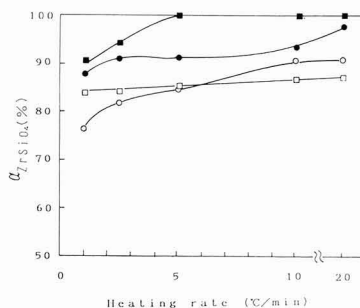

Fig. 3. Formation rate of zircon (ZrSiO$_4$) as a function of heating rate at various concentrations of ZrOCl$_2$.
Temperature: 1300°C, Holding time: 8hr
($\bigcirc$: 0.2M, $\square$: 0.4M, $\bullet$: 1.7M, $\blacksquare$: 0.8M)

phase zircon product was obtained under the conditions of 1300°C and 4hr. However, the mixed 1.7M zirconium oxychloride powder showed a decreasing zircon yield under the conditions of 1200°C for less and 20°C/min, because the crystallization of the unreacted materials took place preferentially to zircon formation.

Next, heating rate was varied (1, 5, 10 and 20°C/min) to examine the zircon yield from the starting mixture sintered
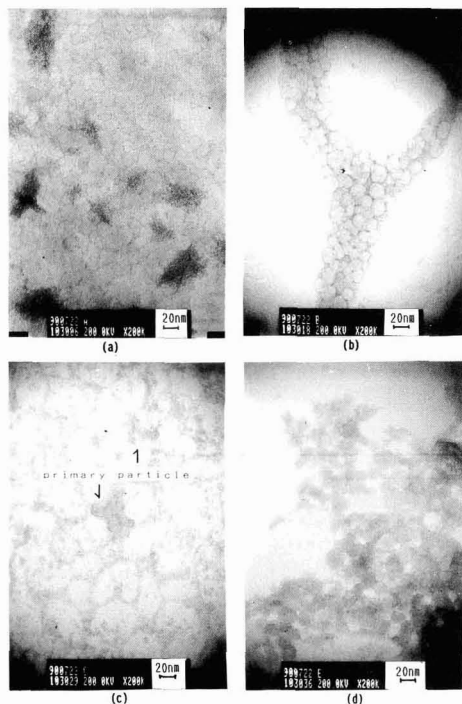
Fig. 4. TEM images of ZrOCl₂ hydrolysis solution.
(a) 0.2M of ZrOCl₂, (b) 0.4M of ZrOCl₂, (c) 0.8M of ZrOCl₂, (d)
1.7M of ZrOCl₂

at 1300°C for 8hr. The results, shown in **Fig.3**, shows that
the zircon yield increased as heating rate increased for all
the mixtures except that of the 0.4M zirconium oxychloride.

It is therefore possible to increase the zircon yield by
increasing the heating rate which controls the crystallization
of the unreacted materials such as zirconia.

3.3. Effects of Particle Size in Hydrolysis Solution

In order to determine why the crystallization of zirconia
or silica is controlled by increasing the heating rate (thereby
increasing the zircon yield), the sizes of the primary and
secondary particles present in the hydrolyzed sol were in-
vestigated.

Figure 4 shows the TEM images of the hydrolyzed sol,
indicating that the primary particles were about 10 to 20nm
in size.   **Figure 5** shows the effects of zirconium
oxychloride concentration on secondary particle size, in-
dicating that the particle size largely depends on the ZrOCl₂
concentration.

These results showed that although increasing the heat-
ing rate controlled the crystallization of zirconia and silica,
the zircon yield was affected less by the heating rate when
the difference in size between the secondary and primary
particles was large as in the 0.4M zirconium oxychloride
mixture. This trend was also observed for the starting mix-
ture of 0.8M zirconium oxychloride, although to a smaller
extent. On the other hand, the starting mixtures of 1.7M
and 0.2M zirconium oxychloride, having a smaller dif-
ferences in particle sizes, were significantly affected by

heating rate (where the zircon yield decreased as the heating
rate decreased) because the crystallization of zirconia and
silica took place preferentially to the formation of zircon.

3.4. Formation of Zircon Precursor and Zircon Yield

It was found that the difference in size between the
secondary and primary particles was one of the factors that
effected zircon formation: however, that alone could not
explain why it was difficult to attain a 100% zircon yield
from the starting mixture of 0.4M zirconia oxychloride. In
an attempt to understand the above phenomenon, the
hydrolysis solution dried at 100°C was analyzed by X-ray
diffraction to observe whether or not the zircon precursor
containing Zr-O-Si bonds was formed. The results shown
in **Fig.6** indicate that the crystalline phase of zircon was
formed from the starting mixture of 0.4M or higher, zir-
conium oxychloride.

The presence of Zr-O-Si, Si-O-Si and Zr-O-Zr bonds in
the 0.2M zirconia oxychloride sample was investigated by
FT-IR to clarify whether or not the diffraction profile, which
appeared faintly, was due to the presence of zircon, and
whether any unreacted zirconia or silica was present in the
zircon phase which appeared at higher concentrations. The
results are shown in **Fig.7**. Known samples of zirconia,
silica, and the single zircon phase sintered at 1500°C were
also analyzed by FT-IR for comparison. The absorptions
considered to be derived from the Zr-O-Si bond were ob-
served near 640 and 900cm⁻¹ indicating formation of the
Zr-O-Si bond.   Similar results were observed for the
samples from lower zirconium oxychloride concentrations.
The X-ray diffraction analysis results also showed that the
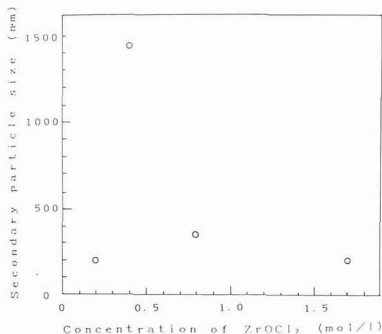sample from the starting mixture with a zirconium

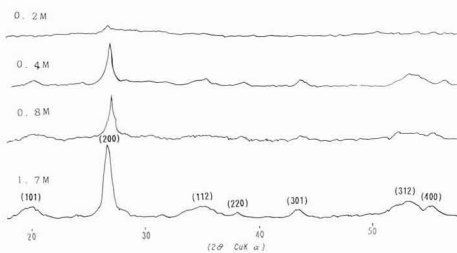**Fig. 5.** Secondary particle size as a function of concentration of
ZrOCl₂.

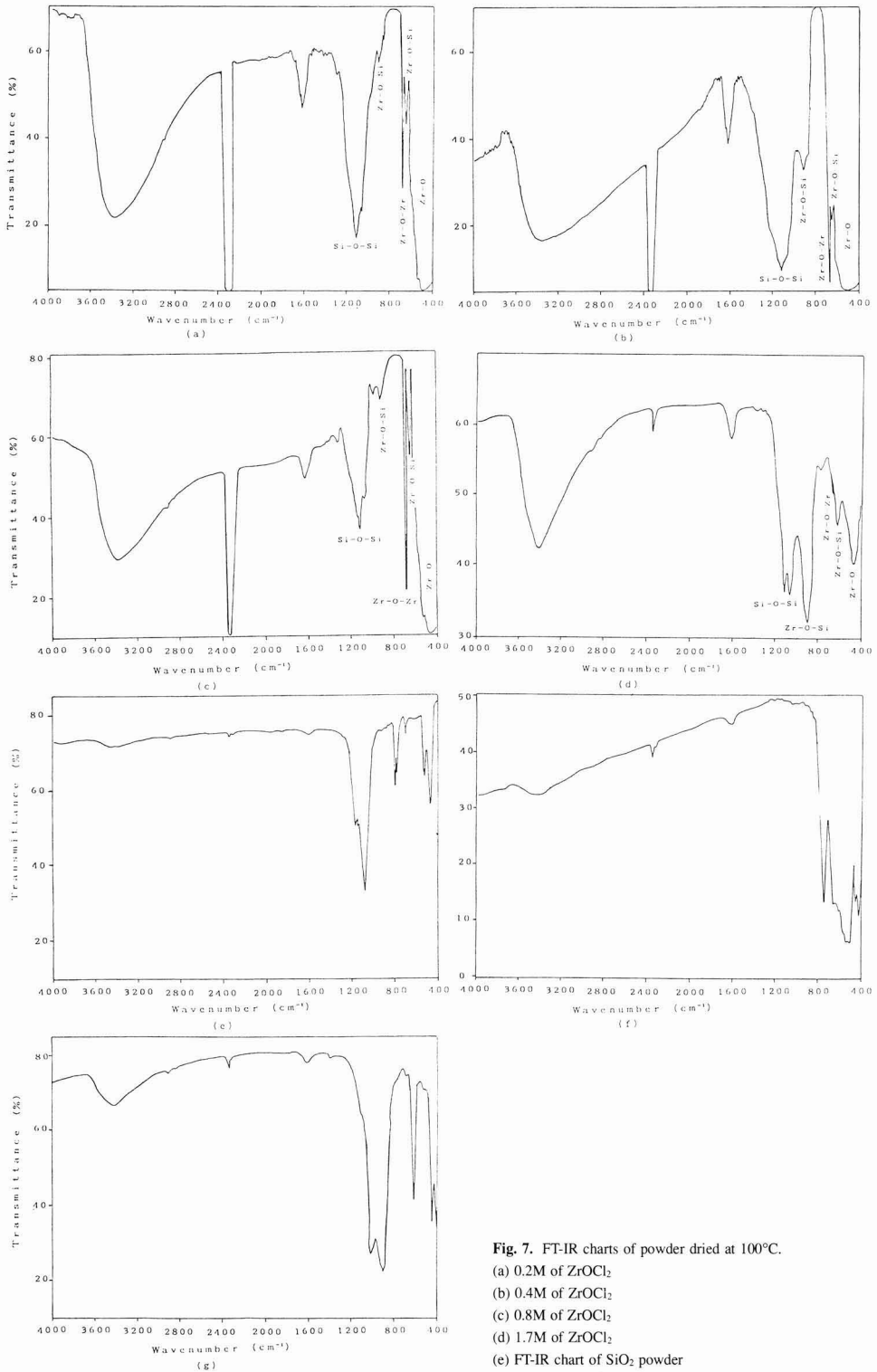**Fig. 6.** X-ray diffraction patterns of powder dried at 100°C.

Fig. 7. FT-IR charts of powder dried at 100°C.
(a) 0.2M of $ZrOCl_2$
(b) 0.4M of $ZrOCl_2$
(c) 0.8M of $ZrOCl_2$
(d) 1.7M of $ZrOCl_2$
(e) FT-IR chart of SiO_2 powder
(f) FT-IR chart of ZrO_2 powder
(g) FT-IR chart of zircon powder.

oxychloride concentration of 0.4M or higher consisting of the single zircon phase alone, exhibited peaks relevant to Si-O-Si and Zr-O-Zr bonds. It was thus concluded that the zircon precursor having a Zr-O-Si bond was formed via the hydrolysis of zirconium oxychloride, and its formation could be accelerated by increasing the zirconium oxychloride concentration.

These results indicated that to increase the zircon yield it was essential to accelerate the formation of the zircon precursor, while keeping the difference between the secondary and primary particles as small as possible. For example, a large zircon yield will not be evident from a starting mixture of 0.4M zirconium oxychloride, even when the zircon precursor is formed, because the size of the secondary particles is large and because the difference in size between the secondary and primary particles is also large. On the other hand, the starting mixture of 1.7M zirconium oxychloride exhibited a low zircon yield, in spite of a large quantity of the zircon precursor being formed, due to the very small size of the secondary particles in the sample. It may be qualitatively concluded that the zircon formation will be accelerated when the starting material, e.g., 0.8M zirconium oxychloride allows the formation of a large quantity of the zircon precursor, and consists of secondary particles of relatively small size.

The test results may be explained by the catalytic nucleus formation mechanism proposed by Komarneni.[12] According to this model, the zircon nuclei formed are introduced into the matrix to reduce the surface free energy, thereby accelerating the formation of zircon. In other words, the zircon nuclei, when formed, will work to increase the zircon yield if the system has a sufficient quantity of the reactive species in contact with the nuclei. It is believed that the zircon precursor species are formed in the hydrolyzed sample to become the zircon nuclei, which expand as they react with the nearby zirconia and silica. Comparing, for example, the samples from the 0.8M and the 1.7M zirconia oxychloride mixtures, the former consisting of large secondary particles would have a larger number of contact points with the nuclei and show a higher zircon yield. On the other hand, in the sample from the starting mixture of 0.4M zirconia oxychloride, the zircon formation would be retarded by unreacted zirconia and silica agglomerated unevenly around a small number of the zircon precursor species, even though the sample consisting of large secondary particles had a large number of contact points. **Figure 8** presents the SEM image of the single zircon phase powder prepared from the starting mixture of 0.8M zirconium oxychloride sintered at 1350°C for 8hr. The zircon powder produced was fine, consisting of particles of 0.5μm or less.

4. Conclusions

Powdered zircon was synthesized from zirconium oxychloride and colloidal silica; some of the factors that affected the synthesis were investigated, with the following results:

1) The zircon yield depended on the concentration of zirconium oxychloride as one of the starting materials. The single-phase zircon was prepared from the starting mixture consisting of equimolar 0.8M zirconium oxychloride and
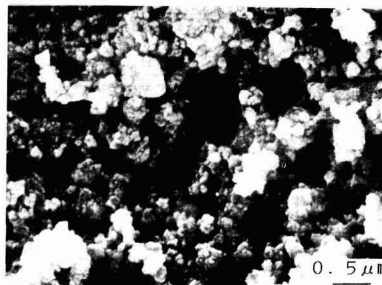

Fig. 8. SEM image of zircon powder.
Concentration of ZrOCl$_2$: 0.8M
Temperature: 1350°C
Holding time: 8hr

colloidal silica, sintered at 1300°C.

2) The zircon yield was also affected by the rate at which the starting mixture was heated: at a low heating rate, crystallization of zirconia and silica took place preferentially, reducing the apparent zircon yield.

3) The effect of the heating rate on the zircon yield related to difference in size between the secondary and primary particles present in the as-hydrolyzed sol: the effect of the heating rate tended to be diminished for the samples having a large difference in secondary/primary particle size.

4) The formation of the zircon precursor was generally accelerated as the concentration of zirconium oxychloride increased.

5) It is essential to accelerate the formation of the zircon precursor and, at the same time, produce secondary particles of relatively small size in the as-hydrolyzed sol, to promote the catalytic nucleus reactions which will increase the zircon yield.

References:
1) S. Motoi, Seramikkusu, 7, 29 (1972).
2) M. Danhara, ibid., 23, 960-62 (1988).
3) Y. Kakumu, Taikabutsu, 39, 510-12 (1987).
4) K. Ichikawa and N. Tsukamoto, "Zircon (Science and Technology)," Uchida Rokaku-ho, (1988) pp.22-42.
5) Y. Kadogawa and Y. Yamate, Yogyo Kyokai-shi, 93, 338-40 (1985).
6) Y. Sugano and T. Suzuki, Zairyo, 37, 378-84 (1988).
7) Y. Sugano and T. Suzuki, Hyomen kagaku, 9, 207-12 (1988).
8) Y. Sugano, "New Materials Series, Zircon," edited by S. Somiya, Uchida Rokaku-ho, (1989) pp.35-41.
9) G. Vilmin. S. Komarneni and R. Roy, J. Mat. Sci., 22, 3556-760 (1987).
10) H. Kobayashi et al., Nippon Seramikkusu Kyokai Gakujytsu Ronbunshi 98, 567–72 (1990).
11) H. Kobayashi et al., Nippon Seramikkusu Kyokai Gakujytsu Ronbunshi 99, 42–46 (1991).
12) S. Komarneni, J. New Ceramics, 2, No.6, 89-94 (1989).

The Appearance Mechanism of Permanent Stains on Glass Plates (III)

Evaporation of a Liquid Droplet of Aqueous Solutions of Slightly Soluble Electrolytes on Glass Plates and the Patterns of the Droplets after Evaporation

Hiroshi Utsugi*, Atsushi Endo*, Noboru Suzuki*, Yukie Kimura*, Atsushi Seki*, Teruo Matsuba*, Takashi Nozu**, and Masao Arakawa**

*Department of Environmental Chemistry, Faculty of Engineering, Utsunomiya University, 2753 Ishii-cho, Utsunomiya, 321, Japan
**Nippon Sheet Glass Corporation Ltd., Central Research Laboratory, Kaidoshi 1, Konoike-aza, Itami 664, Japan

Evaporation of a liquid droplet of aqueous solutions of slightly soluble electrolytes such as $CaCO_3$, $CaSO_4$, and KIO_4 and of concrete-soaked-rain water and concrete-soaked distilled water on untreated and surface-treated glass plate has been investigated through the measurement of bottom length and contact angle of the liquid droplet against time. The deposition of the solute after evaporation has also been investigated. The contact angle decreased at a constant bottom length during the evaporation of a droplet on untreated glass plates. The solute deposited on the edge of the droplet showed a caldera-like ring after complete evaporation. On the other hand, contact angle decreased to a limited value θ_R at a constant length of bottom of a droplet on the hydrophobic surface of glass plate with low surface energy and afterwards the length of bottom of a droplet decreased at a constant contact angle θ_R during its evaporation. A crystalline agglomerate smaller than that of the initial liquid droplet was deposited after complete evaporation.

1. Introduction

The evaporation of liquid droplets on a plate can occur in one of three ways: (A) the bottom length of the droplet is constant and the contact angle varies over time: (B) the bottom length of the droplet is constant until the contact angle reaches a certain level (A type evaporation), thereafter the contact angle stays at a constant level while the bottom length of the droplet decreases, or (C) both the bottom length of the droplet and contact angle decrease.

The evaporation of liquid droplets on the hydrophobic surface of a heat reflective glass plate has been reported as well as the evaporation mechanism for quinoline and iso-quinoline liquid droplets which are known to be type B[1]. On the other hand, studies on the evaporation mechanisms of aqueous solution droplets and the course of the deposition of the solute have shown that liquid droplets on the surface of a heat reflective glass plate undergo A-type evaporation causing caldera-like agglomerations; liquid droplets on the

hydrophobic surface of a heat reflective glass plate with smaller energies undergo B-type evaporation, depositing a group of single crystals.[2] This paper reports our findings regarding the evaporation of liquid droplets of aqueous solutions of slightly soluble electrolytes, including the course of deposition and agglomeration of the solutes after evaporation.

2. Methodology

A section of Ti-deposited heat reflective glass plates were used as the sample plate, 0.5cm in thickness; CFL6S (Top), CFL6S (Back) which was in contact with a tin bath, ODTCS-CFL6S (top), and ODTCS-CFL6S (Back) which was soaked in a hexane solution of octadecyl trichlorosilane (10vol%) for surface treatment, then washed and dried after washed with acetone. The droplets were saturated solutions of calcium carbonate, (0.065wt%) calcium sulfate (0.205wt%) potassium periodate (0.41wt%) rain water (pH=4.8), concrete-soaked-rain water (pH=9.6 ~ 9.9), and concrete-soaked distilled water. The concentration of the concrete-soaked aq. solutions was 0.106g of residue/100ml. The contact angle and the bottom length of a 0.05µl droplet on a sample plate were measured using a contact angle measuring apparatus (Eruma Optical Co., Ltd.) or photographed and then measured.

3. Results

The changes in the contact angle and the bottom length of droplets of saturated aq. solutions of calcium carbonate, calcium sulfate, potassium periodate, concrete-soaked-distilled water, rain water, and concrete-soaked-rain water on CFL6S (Top) and (Back) plates were recorded over the passage of time as shown in **Figs.1, 2** and **3**. Also, the changes in contact angle and bottom length of the droplets on ODTCS-CFL6S are shown in **Figs.4, 5** and **6** to determine the rate equations describing the rate of decrease in the contact angle against time at a fixed bottom length of a droplet. The changes of $(\cos\theta-1)/\sin\theta$ against time are also shown in the same figure. The course of the evaporation of a saturated aq. solution of calcium carbonate on CFL6S (Top) and ODTCS-CFL6S (Top) test plates is shown in
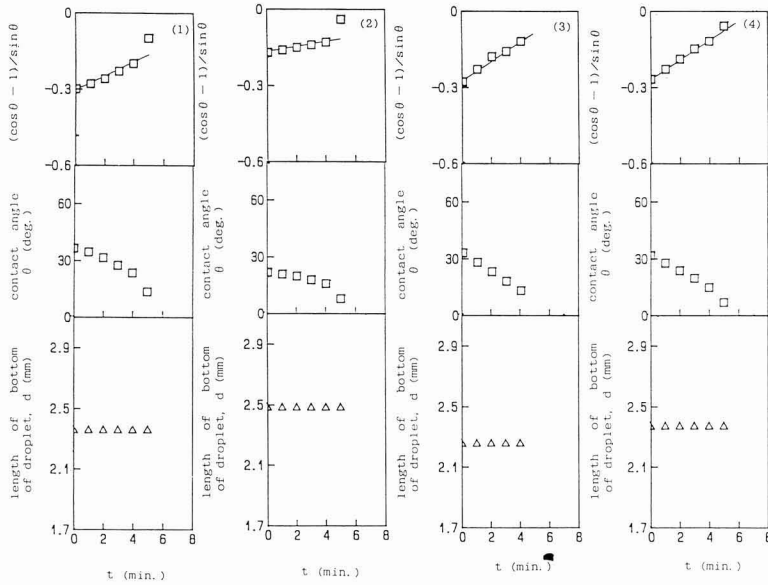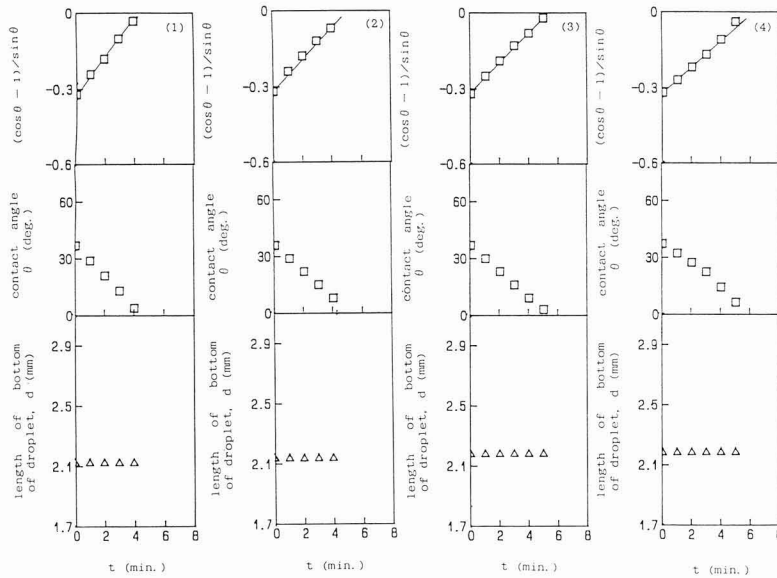
Fig. 1. The change of contact angle and the length of bottom of a droplet of aq. solutions of various kinds of electrolytes on CFL6S (Top) and $(\cos \theta - 1)/\sin \theta$ against time. (1) $CaCO_3$, (2) $CaSO_4$, (3) KIO_4, (4) aq. solution of concrete soaked by water.

Fig. 2. The change of contact angle and the length of bottom of a droplet of aq. solutions of various kinds of electrolytes on CFL6S (Back) and $(\cos \theta - 1)/\sin \theta$ against time. (1) $CaCO_3$, (2) $CaSO_4$, (3) KIO_4, (4) aq. solution of concrete soaked by water.

Fig.7. The deposition of saturated aq. solutions of calcium sulfate, potassium periodate, and concrete-soaked-distilled aq. solutions after evaporation to dryness on CFL6S (Top) and ODTCS-CFL6S (Top) is shown in **Fig.8.** the deposition of concrete-soaked rain water droplets evaporated to dryness on CFL6S (Top) (Back) and ODTCS-CFL6S (Top) and (Back) is shown in **Fig.9**.

4. Discussion

4.1. Droplet Type and Evaporation Mechanism

As shown in **Fig.10**, the evaporated droplets are classified by the following two types:[1,2] (A) the bottom length of the droplet is constant but the contact angle decreases upon evaporation, and (B) the contact angle decreases at a fixed bottom length until the contact angle reaches a certain
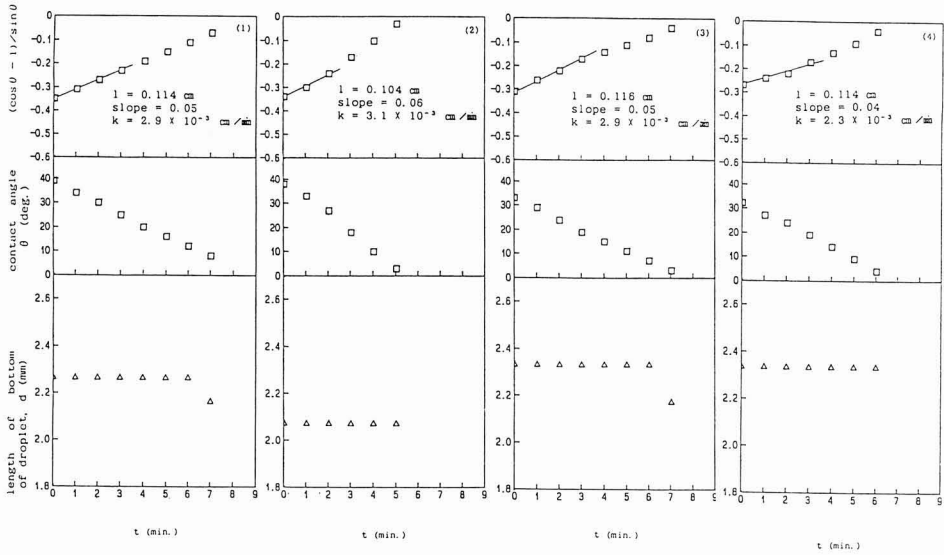
Fig. 3. The change of contact angle and the length of a droplet of the droplets of rain water and aq. solution of concrete soaked by rain water on CFL6S (Top) and (Back) and (cos θ-1)/sin θ against time. (1) rain water on CFL6S (Top), (2) concrete aq. solution on CFL6S (Top), (3) rain water on CFL6S (Back), (4) concrete aq. solution on CFL6S (Back).
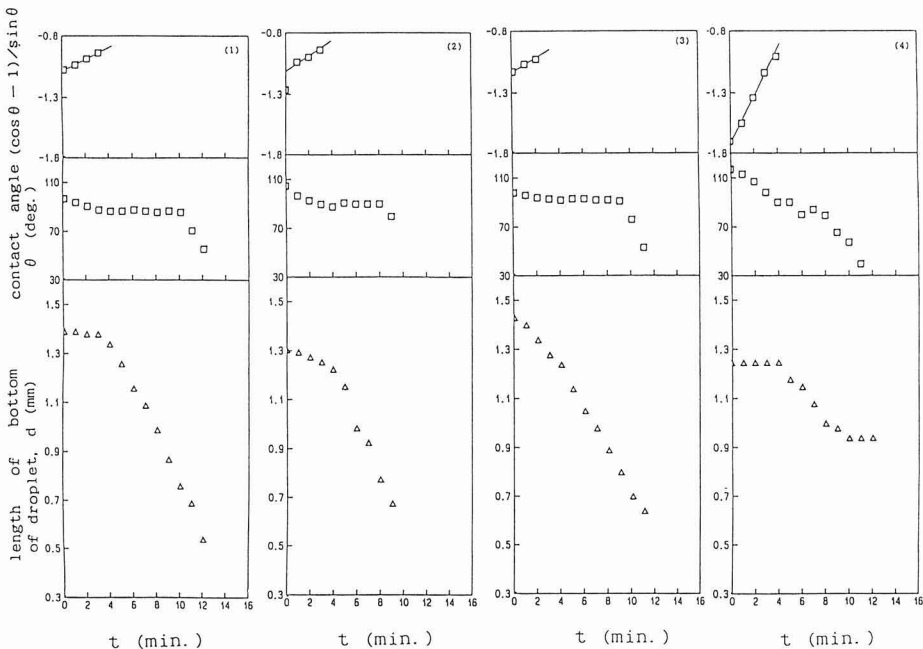

Fig. 4. The change of contact angle and the bottomlength of a droplet of aq. solutions of various kind of electrolytes on ODTCS-CFL6S (Top) and (cos θ-1)/sin θ against time. (1) CaCO₃, (2) CaSO₄, (3) KIO₄, (4) aq. solution of concrete soaked by water.

level, then the bottom length of the droplet decreases at a fixed contact angle. The initial stage of B type evaporation is the same as A type evaporation.

As shown in Figs.1-3, the evaporation of the droplets of the saturated aq. solutions of calcium carbonate, calcium sulfate, potassium periodate, concrete-soaked-distilled water, rain water, and concrete-soaked rain water droplets on CFL6S (Top) and (Back) test plates, causes a decrease in the contact angle and the constant bottom length. This change belonged to A type evaporation. The changes in the contact angle over time can be derived as in our previous report[1] and expressed as follows:
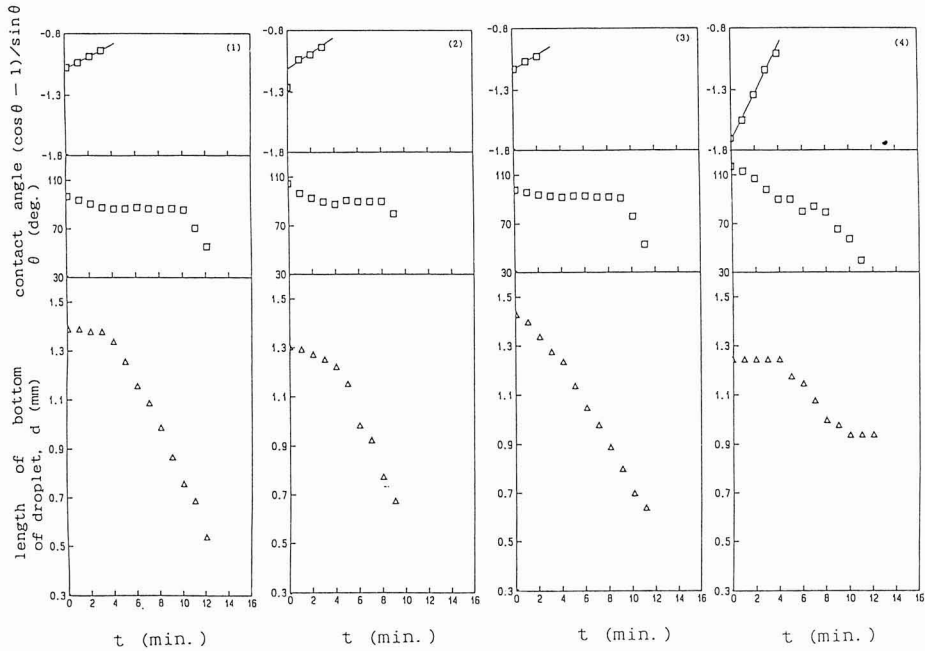
51

Fig. 5. The change of contact angle and the length of bottom of a droplet of aq. solutions of various kind of electrolytes on ODTCS-CFL6S (Back) and (cos θ-1)/sin θ against time. (1) CaCO₃, (2) CaSO₄, (3) KIO₄, (4) aq. solution of concrete soaked by water.

$$\frac{\cos\theta - 1}{\sin\theta} = \frac{\cos\theta_0 - 1}{\sin\theta_0} + \frac{k}{d}t \quad \cdots \cdots \cdots (1)$$

where θ_0, d, and k are the contact angle, bottom length of the droplet and the rate constant. As shown in this Figs.1-3, $(\cos\theta-1)/\sin\theta$ establishes a linear relationship versus time, thus it is assumed that in this case the evaporation follows the mechanism described by equation (1).

The rate constants obtained from the gradients of the straight lines are shown in **Table 1**.

As shown in Figs.4-6, the initial state of the evaporation of liquid droplets on ODTCS-CFL6S (Top) and (Back), test plates which were hydrophobic surfaces with smaller surface energies corresponds to an A type evaporation, indicated by a linear relationship between $(\cos\theta-1)/\sin\theta$ and time. Thus, the evaporation during the initial stage follows the mechanism of Equation (1). The A type rate constant, k, obtained from the gradient of the straight line is also shown in Table 1. When the contact angle reaches a certain angle, θ_R, the evaporation becomes B type, and the change in the of the droplet, d, over time can be expressed as follows:[1]

$$d = d_o - \frac{4\sqrt{\alpha\,(2-\alpha)}}{\alpha\,(3-\alpha)}\,kt \quad \cdots \cdots \cdots (2)$$

where α, d_o, and k represent $\alpha=1-\cos\theta_R$, the initial bottom length of the droplet causing a change in the droplet bottom length, and the rate constant, respectively.

As shown in Figs.4-6, the bottom length of the droplet, d, in a certain range of contact angles, shows a linear relationship versus time, thereby indicating the mechanism described by Equation (2). The B type rate constant obtained from the gradient of this straight line is also shown in Table 1. As shown in this table, the rate constant, k, for drops on both the surface-treated and the untreated CFL6S (Top) and (Back) was $4.0\pm0.8\times10^{-3}$cm/min when derived from the bottom length of the droplet, and $2.8\pm1.0\times10^{-3}$cm/min when derived from the changes in the contact angle. These values are almost in agreement, and correspond the rate constant $3\sim6\times10^{-3}$cm/min,[1] established for the evaporation of liquid droplets on a similar glass surface. the above findings indicate that the mechanism of the evaporation of liquid droplets can be successfully measured from the changes of both the bottom length of droplets and contact angles over time, and that the solute does not noticeably affect the evaporation of water.

4.2. Deposition of Solutes Following the Evaporation of Solvents

The course of the evaporation of saturated aq. solutions of calcium carbonate is shown in Fig.7(A). As shown in the picture taken 10min after the liquid was dropped, the bottom length of the droplet remained unchanged, but a deposit of calcium carbonate was found at the edge of the droplet. The caldera-like deposition of calcium carbonate indicated after the evaporation therefore evaporation was found to be in type A. However, as shown in Fig.7(B), the bottom length of the droplet was founded to be smaller 6 min after liquid was dropped on the surface-treated ODTCS-CFL6S (Top) plate. Since the droplet became a single group of calcium carbonate crystals after evaporation, this evaporation of liquid droplets was type B. The evaporation of liquid droplet of saturated aq. solutions of calcium sulfate, potassium periodate, concrete-soaked-distilled water, rain water, and
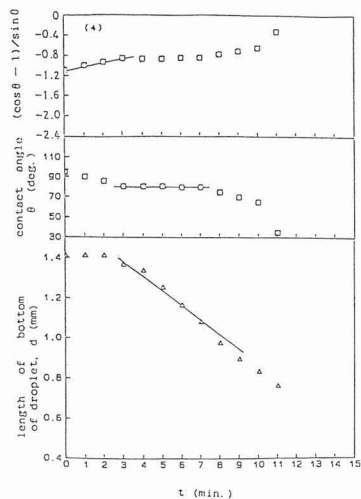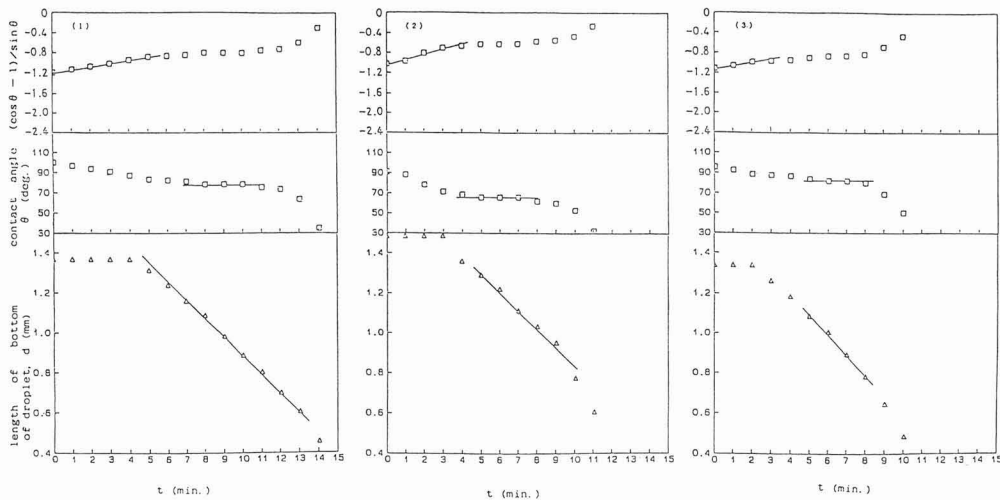
Fig. 6. The change of contact angle and the length of a droplet of the droplets of rain water and aq. solution of concrete soaked by rain water on ODTCS-CFL6S (Top) and (Back) and (cos θ-1)/sin against time. (1) rain water on ODTCS-CFL6S (Top), (2) ODTCS-CFL6S (Back), (4) concrete aq. solution on ODTCS-CFL6S (back).
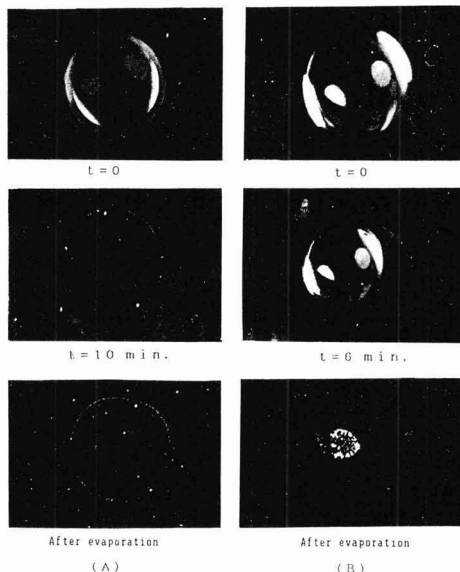
Fig. 7. Photographs of a droplet of CaCO₃, aq. solution on CFL6S (Top) and ODTCS-CFL6S (Top) in the process of evaporation. (A) CFL6S (Top), (B) ODTCS-CFL6S (Top).

concrete-soaked-rain water on the untreated CFL6S (Top) plate exhibited A-type evaporation, and the desposition of solutes after evaporation was found to be on the edge of the droplet as shown in Figs.8 and 9(1). However, as shown in Figs. 8 and 9(2) the solutes were clustered into one place forming a group of crystal after evaporation of their droplets on the surface-treated plate, ODTCS-CFL6S(Top). Thus, the evaporation of liquid droplets was found to be in these cases were B-type.

In the previous cases, the liquid droplets of aqueous solution of slightly soluble solute were found not to shrink, but to deposit solsctes at the edge of the droplets following evaporation on CFL6S (Top) plates having presumably larger surface energies. On the other hand, the droplets on

the hydrophobic ODTCS-CFL6S (Top) plates having lower surface energies shrink at a fixed contact angle, and solutes were gathered in the central portion of the droplets before they formed a group of crystals.

These findings concerning the deposition of solutes following evaporation may give us valuable insight into, for example, the deposition of solutes in regard to the function of the catalytic surface in the impregnation method.

*This paper was partially introduced at a Coloring Material Study Meeting in October, 1988.

*This paper was reported at a Joint Local General Meeting of the Niigata Branch of the Japan Chemical Society in August 1989.
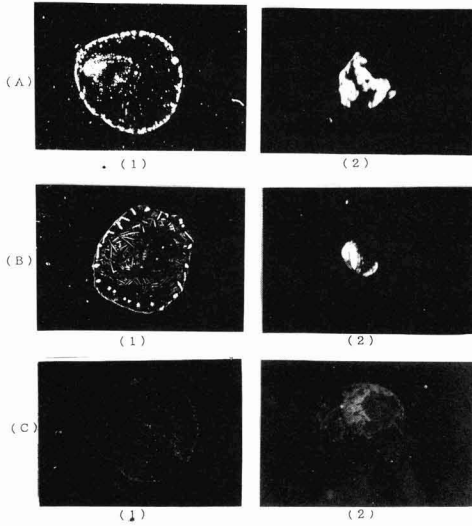
Fig. 8. Photographs of a droplet of aq. solutions of various kinds of electrolytes on CFL6S (Top) and ODTCS-CFL6S (Top) after evaporation.

(1) CFL6S (Top), (2) ODTCS-CFL6S (Top); (A) a droplet of aq. solution of CASO₄, (B) a droplet of aq. solution of KIO₄, (C) a droplet of aq. solution of concrete soaked by water.
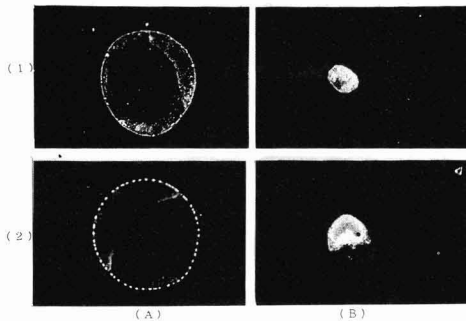

Fig. 9. Photographs of a droplet of aq. solution of concrete soaked by rain water on CFL6S (Top), (Back) and ODTCS-CFL6S (Top), (Back) after evaporation.

(A) CFL6S, (B) ODTCS-CFL6S; (1) TOP, (2) Back.

References:

1) H. Utsuki, A. Endo, N. Suzuki, Y. Iikura, K. Aiba, T. Matsuba, and K. Nozu, Japanese Chemistry, 9, 1531 (1989).

2) H. Utsuki, A. Endo, N. Suzuki, Y. Kimura, A. Seki, T. Matsuba, K. Nozu and M.l Arakawa, Japanese Chemistry, 9, 1540 (1989).

This article is a full translation of the article which appeared in Nippon Seramikkusu Kyokai Gakujutsu Ronbunshi (Japanese version), Vol.99, No.3, 1991.

Table 1. The rate constants of the evaporation of droplets.

| Sample	solute	d (cm)	θ_R(deg.)	length of bottom of a droplet	$k \times 10^3$ (cm/min) contact angle
CFL6S (Top)	CaCO₃	0.119	—	—	2.1
	CaSO₄	0.124	—	—	1.1
	KIO₄	0.114	—	—	2.3
	concrete	0.119	—	—	2.7
CFL6S (Back)	CaCO₃	0.105	—	—	3.7
	CaSO₄	0.107	—	—	3.2
	KIO₄	0.109	—	—	3.3
	concrete	0.109	—	—	2.7
ODTCS-CFL6S (Top)	CaCO₃	0.070	88	2.9	1.8
	CaSO₄	0.070	78	3.6	2.8
	KIO₄	0.068	84	4.3	2.0
	concrete	0.066	74	3.9	3.6
ODTCS-CFL6S (Back)	CaCO₃	0.069	86	4.3	3.8
	CaSO₄	0.065	90	5.0	2.1
	KIO₄	0.071	91	4.0	3.1
	concrete	0.069	81	3.9	4.7
CFL6S (Top)	rain water	0.114	—	—	2.9
	concrete (rain water)	0.104	—	—	3.1
CFL6S (Back)	rain water	0.116	—	—	2.9
	concrete (rain water)	0.114	—	—	2.3
ODTCS-CFL6S (Top)	rain water	0.068	78	4.5	2.4
	concrete (rain water)	0.074	65	3.5	4.1
ODTCS-CFL6S (Back)	rain water	0.067	80	4.5	2.3
	concrete (rain water)	0.071	80	3.2	2.8
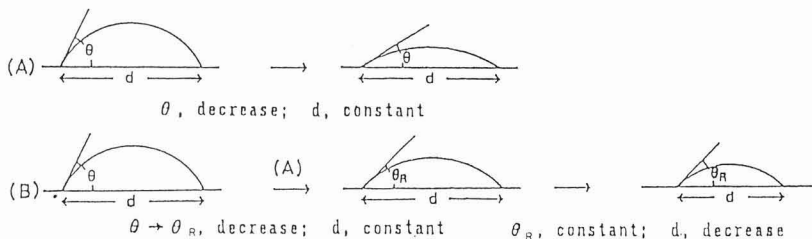
Fig. 10. Schematic diagram of evaporation of liquid droplet.

Synthesis of Mullite from Fly Ash and Alumina Powder Mixture

Takeshi Ohtake, Kunio Uchida[*], Fumikazu Ikazaki[*], Mitsutaka Kawamura[*], Teiji Ohkubo[*] and Kunio Kamiya[*]

Uchiyama Concrete Co., 1-7-23, Fujimi, Urayasu-shi, Chiba 279-01
[*]National Chemical Laboratory for Industry, 1-1, Higashi, Tsukuba-shi, Ibaraki 305

Synthesis of mullite from fly ash mixed with alumina powder was studied. A suitable fly ash containing small amounts of flux components such as alkali, alkali earth metal and iron oxides and contents of the flux components reduced by pretreatment like magnetic led to separation, a mullite-like material with relatively good quality. When a 1:1 mixture of pretreated fly ash and γ-alumina was heated to above 1673K, 80% mullite yield was achieved. Properties of sintered bodies of mullite powder made from fly ash and γ-alumina were almost comparable to those of a synthetic commercial grade mullite body.

1. Introduction

The possibility of improving the properties of fly ash particularly kaoline was studied in an attempt to prepare replacement ceramic materials, namely mullite. In view of its high purity and excellent mechanical properties, numerous studies have been made on the synthetic methods for mullite as well as its evaluation as a fine powder.[1-8] Inexpensive general-purpose mullite is used for wear-resistant materials such as tile, pope lining, etc., and is attracting interest as a wear-resistant building material due to its interlocking capabilities and its water permeability.

About 3.8 million tons of fly ash are annually emitted, primarily by thermal power stations, 40% of which is used in cement, calcium silicate fertilizers, lightweight aggregates, etc.; however, the remaining 60% is used as reclaimed landfill and generates disposal expenses.

Fly ash is generated in the flame of a thermal power station boiler whose temperature is as high as 1773~1873K. As shown in the X-ray diffraction pattern in **Fig.1**, differing quantities of mullite and quartz, a major mineral, are present as well as the existence of a glass which composes the matrix. It is believed that this fly ash can be used as a silica source, and if its mixture with alumina is calcined, the alumina and quartz will readily react with the glass to yield mullite. However, mullite contains impurites such as alkali, alkaline earth, and iron oxides, which are unsuitable substances, thus a method of eliminating such impurities was studied along with an analysis of the properties of mullite prepared from pretreated fly ash.

2. Experimental Procedure

Fly ash was obtained from two different sources, the Matsushima Power Plant of Tohoku Electric Power k.k. and the Shin-Onoda Power Plant of Chugoku Electric Power K.K. The alumina source was γ-alumina.

In the chemical analysis of the ash, alumina, and calcined bodies, the samples were dissolved and SiO_2 was quantitatively determined by the precipitation weight measurement method or in solution by the colorimetric method using molybdenum blue for coloration. Al_2O_3, CaO and MgO were titrated by EDTA, Fe_2O_3 and TiO_2 were determined by colorimetry, and Na_2O and K_2O by flame spectrochemical analysis.

Impurities contained in the fly ash could be removed by pretreatment such as the primary elimination of iron by magnetic separation, decarbonization by calcination, pulverization, as well as secondary elimination of iron by acid washing. Different combinations of procedures and their conditions were studied.

In studying the generation of mullite and the properties of mullite-like materials, pretreated fly ash and alumina were compounded in a dried weight ratio of 1:1, mixed and pulverized using a crushing type pulverizer (mean particle diameter: 7~8μm) so that the composition of materials approximated the chemical composition.

The weight ratios of $[SiO_2]/[Al_2O_3]$ in the Shinonoda and Tohoku fly ash samples were 34.6/65.4 and 33.6/67.4, respectively, calculated by the following equation using the analyzed values given in **Table 1**. This compounded sample was mixed with 10wt% water to obtain a moist $[SiO_2]/[Al_2O_3]=[0.5SiO_{2[ash]}/\{[0.5Al_2O_3]_{ash} + 0.5\}$ powder before it was pressed (~98MPa) into a mold about 16 mm in diameter and 14~16 mm in height. An electric furnace with molybdenum disilicide heating elements was used to
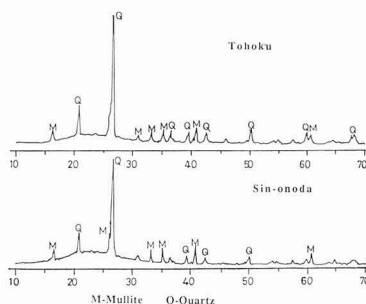

Fig. 1. X-ray diffraction patterns of fly ash

Table 1. Chemical composition of fly ash

Ash	Pretreatment	SiO₂	Al₂O₃	Fe₂O₃	TiO₂	CaO	MgO	K₂O	Na₂O	Ig. loss	Total
M	As received	59.09	22.46	4.86	0.96	4.27	1.85	1.80	1.77	2.64	99.70
	Magnetic Sep -Decarbon.	62.04	24.57	1.70	0.94	4.70	1.87	1.97	1.87	-	99.66
	Magnetic Sep -Acid wash.	67.22	24.61	1.66	0.94	1.12	0.76	1.85	1.51	-	99.67
O	As received	64.36	21.75	1.82	1.20	1.44	0.94	3.02	0.83	4.50	99.88
	Magnetic Sep -Decarbon.	68.40	25.24	0.97	1.18	0.81	0.29	2.44	0.25	-	99.58

Cf.   M: Tohoku power plant ash, O: Sin-onoda power plant ash
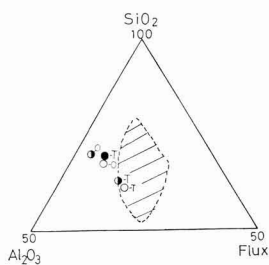
Fig. 2. Chemical composition of fly ash represented by triangular diagram. ○-T:Tohoku (as received), ○- O:Sin-onoda (as received), ◑-T:Tohoku (Magnetic Sep-Decarbon), ◑-O:Sin-onoda (Magnetic Sep-Decarbon), ●-T:Tohoku (Magnetic Sep-Decarbon-Acid Wash)
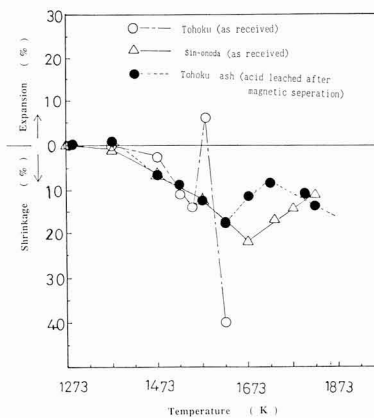

Fig. 3. Shrinkage and expansion properties of received and pretreated ashes observed by a high temperature microscope in air at heating rate of 9 deg/min.

calcine the bodies at 1673, 1773, 1873, and 2123K for 2 hours using a heating rate of 150°/hr.

The chemical composition, degree of shrinkage, and water absorption of the calcined bodies, true density of the ground powder of the calcined bodies and of the starting minerals were identified by x-ray diffraction and quantitatively determined by the method using calibration curves. In addition, SEM observation of the samples was conducted. The diffraction patterns of the (210) plane were integrated for the quantitative determination of mullite in the calcined bodies, as were the diffraction patterns of the (012) plane of α-alumina.

Commercially available mullite and α-alumina powder were used to prepare calibration curves, and potassium chloride was used as a reference substance. Mullite powder from the ground sintered bodies, as well as commercially available mullite, was molded under the above conditions, and the following properties of the sintered bodies prepared at 1873K were measured for comparison: degree for shrinkage, water absorption, bulk density, compressive strength 1=4F/π ab where F: load, a: sample diameter, b: sample height; high-temperature bending strength, heat resistance, thermal shock resistance, and the thermal expansion coefficient.

3. Experimental Results and Discussion

3.1. Pretreatment of Fly Ash

Blowing which often expands a mold during the course

of preparing mullite from a compound sample, and coloring due to the iron oxide impurity, contribute to a decrease in the quality of the mullite produced. Thus, the materials must be purified to avoid this decline in product quality. As shown in Table 1, the chemical composition of fly ash samples differed as to the production site, but the main components were silica and alumina (85~90%), followed by iron oxide, calcium oxide, and ignition loss (3~10%). The CaO component, 2~5%, was due to the combusted coal, but a larger amount of CaO could be observed if it had been added in the course of the dry desulfurization of waste gas from a thermal power station. The ignition loss was primarily non-combusted residual coal. The fly ash, expressed in a triangular diagram for the 3 elements: SiO₂, Al₂O₃, flux (Na₂O + K₂O +CaO + Mg₂O +FeO + Fe₂O₃), corresponds to the white circles in **Fig.2**. The range of chemical compositions of substances exhibiting expanding properties as reported by Riley[10] is also shown by the shaded area in Fig.2. When the chemical composition of the fly ash exists within this range of compositions, the fly ash samples expand (foam) in the neighborhood of 1473~1573K when heated. As shown in **Fig.3,** the expanding property of the fly ash was in agreement with that predicted by Riley, with the untreated Tohoku ash (material ash) expanding at a temperature above 1523K. The required conditions and the combination of pretreatments used to improve the above properties are shown in **Fig.4.** The chan-

ges in the fly ash chemical compositions due to these pretreatments are shown in Fig.2 initially removing the iron by magnetic separation, improved the composition to some extent as shown in the figure, however it was not sufficient. The chemical composition could be successfully shifted from the range of expanding properties if the iron was secondarily removed by acid washing. As a result, an abnormal expansion in the heated property of treated ash (Tohoku ash) was improved in the neighborhood of 1473~1573K as shown in Fig.3.

3.2. Changes in the Generation of Mullite due to Sintering Temperature

Figure 5 shows an x-ray diffraction diagrams for bodies sintered at different temperatures. The major diffraction patterns were identified as mullite and α-Al_2O_3. The minor diffraction patterns, however, were not identifiable. **Figure 6** shows the temperature dependent mullite and α-Al_2O_3 yields which were quantitatively determined using the calibration curves. It was found that there was already 34% mullite at 1473K, and approximately 80% at 1673K. The results of this quantitative determination were in agreement with mullite yields using kaoline as the starting material.[8]

The powder obtained by grinding the calcined body is shown in **Fig.7**, however, the characteristic shape of the mullite particles remains unclear. The physical properties

of the calcined bodies depended on the calcining temperature as shown in **Fig.8**. It is surmised from the changes in the degree of shrinkage and absorption that the sintering progressed with a rise in temperature, but the density ratio between the powder of the calcined body and mullite was nearly fixed. This corresponds well to the volumes of mullite and α-Al_2O_3 previously determined for this temperature
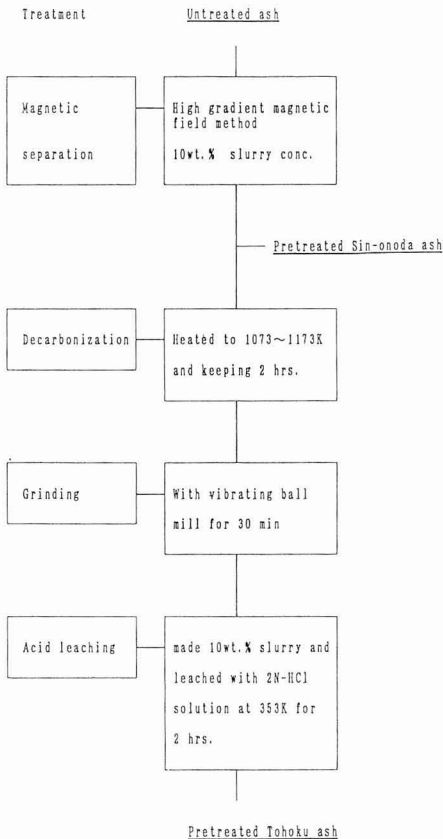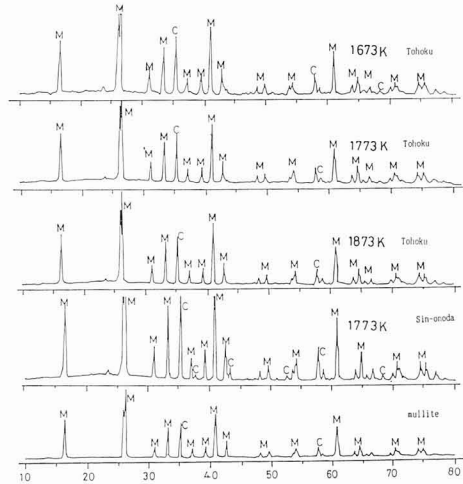

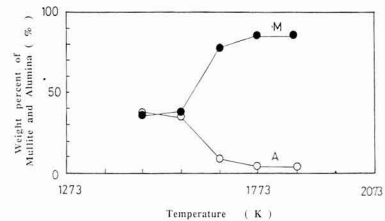**Fig. 5.** X-ray diffraction patterns of the sample heated at different temperature s

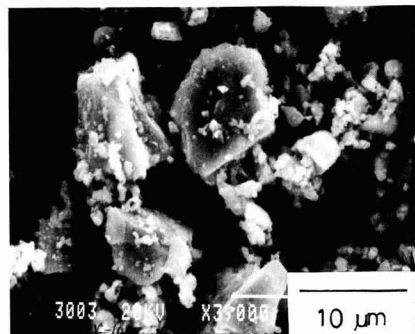**Fig. 6.** Change of mullite generation with temperature; M: mullite, A: alumina

Fig. 7. SEM photograph of mullite powder synthesized at 1873K

Fig. 4. Flow sheet of pretreatment and its condition

Treatment   Untreated ash

Magnetic separation — High gradient magnetic field method   10wt.% slurry conc.

—— Pretreated Sin-onoda ash

Decarbonization — Heated to 1073~1173K and keeping 2 hrs.

Grinding — With vibrating ball mill for 30 min

Acid leaching — made 10wt.% slurry and leached with 2N-HCl solution at 353K for 2 hrs.

Pretreated Tohoku ash

range as were shown in Fig.6.

In view of these results, it is possible that no direct correlation exists between the progression of sintering and the mullite yield.

The sintering of mullite is known to occur at any level above 1900K,[11] however, the fact that this sample was sinterable at a relatively lower temperature may be attributable to the excessive levels of SiO_2 and the flux elements (Fe_2O_3, CaO, MgO, R_2O) listed in **Table 2.**

3.3. Comparison with Commercially Available Synthesized Mullite

Table 3 shows the properties of commercially available synthesized mullite heated at 150°/hr and sintered at 1873K for 2 hr; these results were compared with those for the sintered bodies of mullite synthesized from fly ash. The commercially available synthesized mullite remained non-sintered with an absorption rate of 13.2% and bulk density of 2.15 even though the powder was molded and calcined at 1873K; the molded body of mullite powder from fly ash was almost sintered.

The optimal calcining condition: SiO_2=38% and Al_2O_3=60% of commercially available mullite ceramics exhibited a strength of 180MPa, a thermal expansion coefficient of 4.6×10^{-6}/K, waster absorption of 0.0% and specific gravity of about 2.7.[12] It is naturally expected that a sintered body of commercially available mullite will exhibit better properties than fly-ash mullite. Nonetheless, the excellent values obtained from the sintered bodies of fly ash under the above conditions may be explained by the differences in degree of sinterability between the commercially available mullite and the fly ash mullite. The two fly-ash mullite samples were more easily sintered than the commercially available mullite, thus the fly-ash mullite samples showing similar levels of thermal of 56.9MPa (Shin-onoda ash) and 86.4MPa (Tohoku ash) which were higher than that of the commercially available mullite. In addition, the true density was less than that of highly purified mullite, due to the larger silica content.

Thus, wear resistant materials benefiting from improved properties at lower sintering temperatures are expected to be developed in the future. Another characteristic of mullite ceramics, the bending strength at high temperatures varies depending on the ratio between silica and alumina and that between mullite and silica.[4,6] As shown in Table 3, the fly-ash mullite exhibited a strength of 130~160MPa at 1273K under the current sintering conditions. Although it is far less than the strength of highly purified mullite (e.g. 300MPa at 1573K with 71% Al_2O_3), it is sufficient for use as general-purpose heat-resistant materials for heat transfer pipes at high temperature, etc.
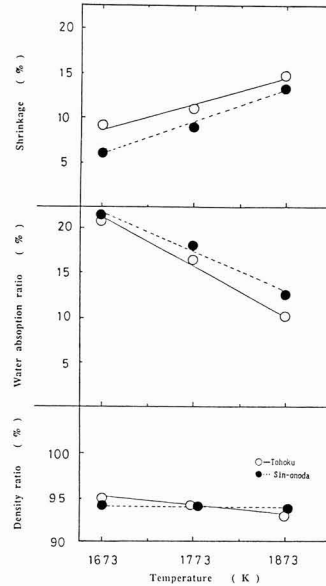

Fig. 8. Change of product property with heating temperature Density ratio (%), Water absorption ratio (%), Shrinkage (%)

Table 2. Chemical composition of synthetic mullite powder

Prod.	Raw material	SiO₂	Al₂O₃	Fe₂O₃	TiO₂	CaO	MgO	K₂O	Na₂O	Total	Al₂O₃/SiO₂ ‡
1	Ash-M+γ alumina	35.49	59.82	0.92	0.53	0.63	0.35	0.92	0.70	99.36	0.991
2	Ash-O+γ alumina	35.45	61.19	0.59	0.54	0.42	0.14	0.92	0.72	99.97	1.015
4	Commercial Mullite	26.39	71.37	0.72	0.07	0.25	0.02	0.18	0.36	99.36	1.59

‡ mole ratio

Table 3. Properties of mullite body made from fly ash and alumina (mixing ratio 1:1)

Sample	Silica source	Alumina source	Shrinkage (%)	Water absorption ratio (%)	Bulk density (g/ml)	Density (g/ml)	Compressive strength (MPa)	Flexural strength (MPa) R.T.	Flexural strength (MPa) 1273K	Thermal expansion coef. x10⁻⁶/K	Resist. to thermal shock (K)	Pyrometric cone equivalent SK No
1	Ash-M	γ	13.1	0	2.62	2.99	86.4	162.5	126.5	8.69	245	38
2	Ash-O	γ	12.5	3.4	2.62	2.98	56.9	195.0	160.0	5.47	245	38 *
4‡	Kaolin	H	3.1	13.2	2.15	3.11	29.4	105.0	78.5	6.30	245	38 *

Calcination condition; heating rate=150 deg/h, keeping temperature=1873K, keeping time=2h
M: Tohoku power station   γ: γ-alumina   H: aluminium hydroxide
*‡: Commercial mullite

4. Conclusion

In an attempt to effectively use fly ash containing large amounts of oxide impurities, an inexpensive method of synthesizing mullite was studied, resulting in the following findings:

1) Paying attention to the composition of fly ash selected, it can be successfully used to replace the silica source in manufacturing mullite if iron alone is removed by magnetic separation.

2) When fly ash and alumina are compounded in a ratio of 1:1, approximately 80% of mullite was yielded at sintering temperatures higher than 1673K as shown by x-ray diffraction results.

3) As compared to commercially available mullite powder, fly-ash mullite powder was more easily sintered at a lower temperature. This was conceivably attributable to the chemical composition of the fly ash; the excessive levels of SiO_2 and flux elements (Fe_2O_3, CaO, MgO, R_2O) were different from those in the theoretical composition, and acted as a sintering adjunct.

4) The mechanical properties of the sintered bodies of fly-ash mullite compared well to the properties of sintered bodies of commercially available synthesized mullite under the same conditions but at relatively lower temperature. Thus the fly-ash mullite should be sufficiently useful as a general-purpose mullite material.

References

1) K.S. Madzudiyasni and L.W. Brown; J. Am. Ceram. Soc., 55, 546(1972).
2) M.Suzuki, S.Hiraishi, M.Yoshimura, and S.Unemiya, Ceramic Soc. Japan, 92, 320 (1984).
3) Y.Hirata, H.Minamisono, and K.Shimada, ibid., 93, 36 (1985).
4) S.Kanzaki, T.Kumazawa, J.Asaumi, O.Abe, and H.Tabata, ibid., 93, 407 (1985).
5) K.Hamano, T.satoh, and Z.Nakagawa, ibid., 94, 818 (1986).
6) S.Kanzaki, T.Kurihara, N.Iwai, Y.Ohashi, and H.Tabata, ibid., 95, 1213 (1987).
7) H.Suzuki and H.Saito, ibid., 95, 697 (1987).
8) T.Mitsutome, I.Furusako, and H.Nagai, "Mullite 2-Materials and Sintered Bodies" Uchida Roukakuho (1987) p129.
9) Y.Nakamura, Materials, 15, 184 (1966).
10) C.M. Riley, J. Am. Ceram. Soc., 34, 121 (1951).
11) S.Ohta and T.Kumazawa, "Mullite 2-Materials and Sintered Bodies" Uchida Rokakuho (1987) p93.
12) S.Munemiya, "Mullite 2-Materials and Sintered Bodies" Uchida Rokakuho (1987) p1.

Effect of Aluminum Doping on the Thermoelectric Power of Sintered SiC

Kazuo Okano, Kenji Fujinuma, Kazutoshi Maruoka

Department of Electric Devices Technology, Oyama Polytechnic College
612-1, Yokokura Mitake, Oyama-shi, Tochigi, 323, Japan

The effects of aluminum doping on the thermoelectric power of sintered SiC were investigated, SiC doped with up to 0.6wt% aluminum was fired in the temperature range 1900°C ~ 2050°C. The thermoelectric power was measured at 100°C in vacuum with a temperature difference of 10K across the specimen. The thermoelectric power increased with increasing aluminum addition and with the firing temperature. Non-aluminum containing SiC fired at 1900°C had the lowest thermoelectric power at 2μv/k. On the other hand, SiC doped with added 0.6wt% aluminum and fired at 2050°C had the highest thermoelectric power at 60μV/K.

1. Introduction

Sintered SiC is a typical ceramic semiconductor with excellent chemical stability at high temperatures, thus its application to high-temperature electronic devices such as high-temperature thermistors[1-3] and thermal batteries[4] is expected. The electrical properties of sintered SiC are notably affected by the defects in crystal grains and the concentration of impurities, etc. involved in the microstructure, and are therefore also sensitive to manufacturing conditions such as the kind and amount of additives, firing temperature, etc. Thus, it is necessary to clarify the relationships among the manufacturing conditions, microstructure and electric properties of sintered bodies.

In this study experiments were conducted in which the effects of additional impurities on the electrical properties were investigated as part of an on-going effort to produce a sintered SiC applicable to thermal batteries. Various amounts of aluminum and several firing temperatures were established by changing the manufacturing conditions prior to studying the effects on the thermoelectric power.

2. Experiment

2.1. Specimen Manufacturing

α-SiC of 0.42μm in mean particle diameter, manufactured by Showa Denko K.K. was used as the starting material. Carbon (2.0wt%) and boron (0.5wt%) were used as sintering aids and aluminum (0 ~ 0.6wt%) was added as the dopant. Phenolic resin was added to provide the 2.0wt%

of carbon. Aluminum boride, AlB_2 was added to yield 0.2, 0.4, or 0.6wt% of aluminum; and boron carbide, B_4C, was added to give 0.5wt% boron in each specimen. The powders were mixed by the wet method in a Teflon ball mill using benzene as a catalyst for 24hr before drying. The dried powder was then uniaxially pressed into a pellet of $15mm\Phi \times 2.5mm^1$ at 150MPa, and heated in a vacuum at 1900° ~ 2050°C for one hour.

2.2. Observation by Scanning Electron Microscope

The surfaces of the specimens were polished by mirror grinding and etched using aqueous solutions of potassium ferricyanide and sodium hydroxide to observe the microstructures by scanning electron microscope.

2.3. Measurement of Thermoelectric Power

Figure 1 shows a schematic diagram of the apparatus used to measure thermoelectric power. Specimen ① was fixed by the sample holder ②, and the temperature at both ends of the sample was adjusted by operating the upper and lower heaters ④. The temperature at both ends of the sample was measured by respective thermocouples ③. The thermoelectric power, V_T, of the sample was measured with temperature difference of 10K at a mean temperature of 373. The measurement was made in vacuum by connecting the exhaust vent ⑤ with a vacuum pump.

3. Results and Discussion

Figure 2 shows SEM photographs of respective samples containing 0 ~ 0.6wt% of aluminum fired at 1900° to 2050°C. The particle diameter tended to be larger and more highly densified when a larger amount of aluminum
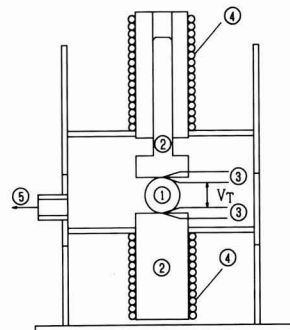

Fig. 1. Schematic diagram of thermoelectric power measurement apparatus.

was added at higher firing temperatures.

Samples containing less than 0.4wt% aluminum showed more pore and no marked growth of grains when fired at 1900°C. When fired at 1950°C, the sample containing less than 0.2wt% aluminum exhibited many pore, however, the particle diameters were smaller. For the specimen sintered at 2000°C, the sample which doesn't contained aluminum exhibited many pores, however small particle diameters.

The particles were significantly larger and more densified in the samples fired at 2050°C irrespective of the amount of aluminum. Thus, it was shown that even with small amounts of the aluminum additive, marked particle growth could be achieved when the firing temperature was higher.

To explore the relationship between the microstructure and firing temperature, the added amount of aluminum was fixed. The particle growth was significant with notably fewer pore only in those samples free of any aluminum and fired at 2050°C. Marked growth and density of particles were recognized in the samples containing 0.2 and 0.4wt% aluminum, fired at 2000° and 1950°C, respectively. Marked growth and density were also recognized in the samples containing 0.6wt% aluminum fired at all temperature levels. When the thermoelectric power of these samples was measured, all samples were found to be P type, irrespective of the amount of aluminum. This was conceivably a result of the boron and aluminum (added as firing aids) acting as acceptors in the semiconductive material.

Figure 3 shows the relationship between the firing temperature and the Seebeck coefficient for the samples containing different amounts of aluminum. At a fixed
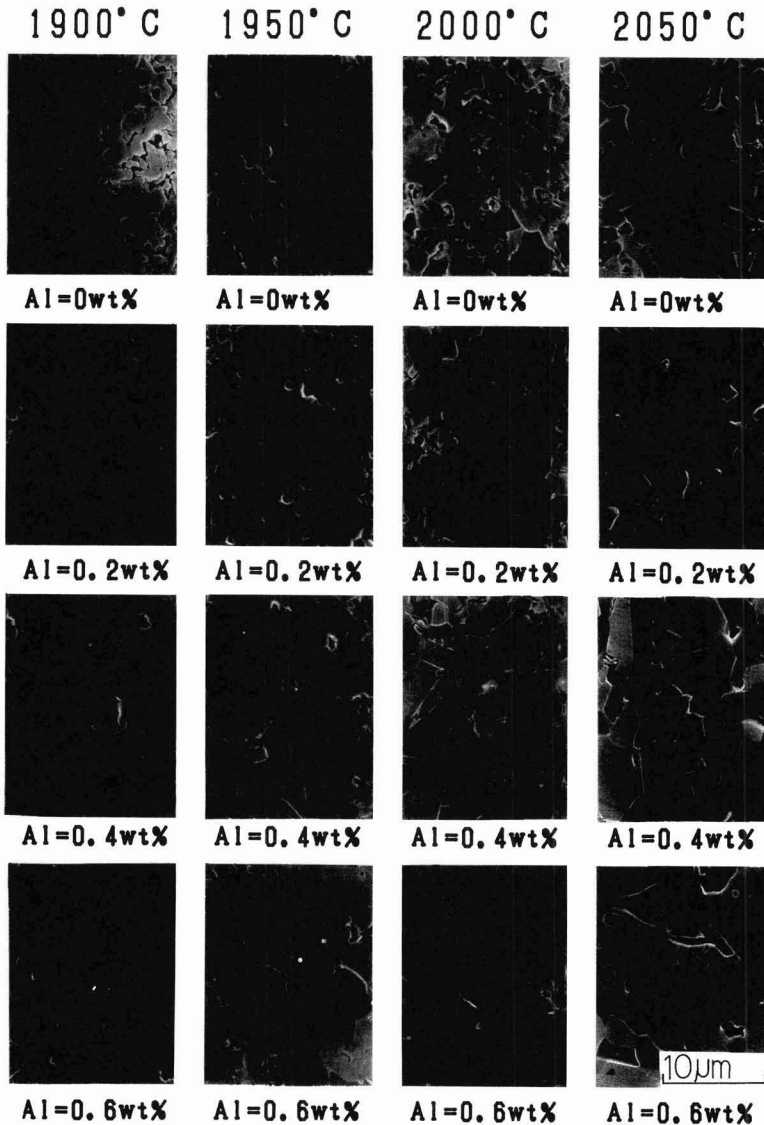

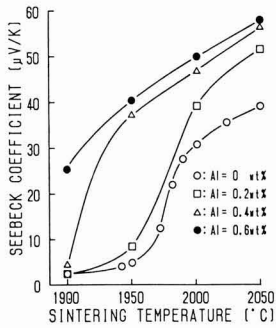**Fig. 2.** SEM photographs of etched surface of sintered SiC

Fig. 3. Seebeck coefficient of sintered SiC as a function of sinter-
ing temperature.

Fig. 4. Seebeck coefficient of sintered SiC as a function of
aluminum addition.

aluminum content, the Seebeck coefficient increases with
the firing temperature. In the samples containing less than
0.2wt% aluminum, the Seebeck coefficient showed a rapid
increase between 1950° and 2000°C. This maybe explained
by the fact that boron added to SiC as a sintering aid is
rapidly diffused among the SiC particles around 1950°C.[5,6]
Thus, when the firing temperature exceeds 1950°C, the
boron, acting as a sintering aid, becomes important along
with an increases in density, and the Seebeck coefficient
rapidly increases when the diffused boron becomes an ac-
ceptor. Such rapid changes become less notable, however,
when the aluminum concentraion is increased, to the point
where the Seebeck coefficient increases almost linearly with
increasing firing temperature in the sample containing
0.6wt% aluminum. The effects of aluminum and boron dif-
fusion are reflected in the Seebeck coefficient in samples
containing larger amounts of aluminum, and the rapid chan-
ges deriving from boron diffusion are conceivably
diminished.

The data in Fig.3 is replotted in **Fig.4** to illustrate the
relationship between the Seebeck coefficient and the amount
of aluminum for the different firing temperatures. The
Seebeck coefficient of the sintered SiC increased with in-
creasing aluminum content for all firing temperatures.
Since boron is diffused in SiC particles when the firing
temperature is higher than 2000°C, the Seebeck coefficient
is high even if the sample contains no aluminum.

When the firing temperature is as high as 1950°C, the
Seebeck coefficient was less than 10μV/K in the samples
with more , pores and smaller than average particle
diameter, i.e., those containing less than 0.2wt% aluminum.
However, the Seebeck coefficient rapidly increased when
the aluminum content increased to more than 0.4wt%.
When the firing temperature was 1900°C, the Seebeck coef-
ficient was smaller than 10μV/K in the samples containing
less than 0.4wt% aluminum (e.g, those with more pores
and mean particle diameters less than 2μm as shown in
Fig.2), and increased by about nearly a factor of 10 when
the aluminum content increased to 0.6wt%.

The smaller Seebeck coefficients in the samples with
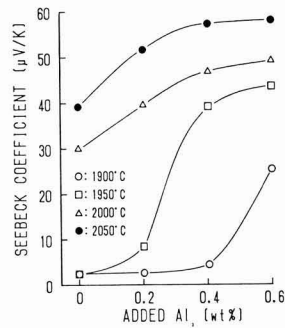more pores and smaller mean particle diameters may be

explained as follows. When the microstructure was ob-
served, it was found that these pores became smaller with
larger mean particle diameters as more aluminum was added
at higher firing temperatures. Since the microstructure of
the SiC particles is notably affected by the addition of
aluminum, the more aluminum diffused in the sample, the
higher the Seebeck coefficient becomes due to the higher
concentrations of the acceptor.

4. Conclusions

The following summarizes our findings regarding the ef-
fects of additional aluminum and firing temperatures on the
thermoelectric power of sintered SiC.
1) When the firing temperature was fixed, the Seebeck coef-
   ficient increased as the aluminum content increased.
2) When aluminum content was fixed, the Seebeck coeffi-
   cient of a sample increased as the firing temperature was
   raised.
3) The Seebeck coefficient experienced the minimum value
   of 2μV/K when no aluminum was added at 1900°C, and
   exhibited the maximum level of 60μV/K when 0.6wt%
   of aluminum was added at 2050°C.

References:
1) K. Okano, Trans IEICE, Vol.E70, (1987) pp.336-38.
2) K. Okano, H. Kurisaki and S. Kaminouchi and M. Ito, Ceramic
   Articles, 97, 1176-80 (1989).
3) K. Okano, Ceramics Association, 94, 219-25 (1986).
4) C. Pai, K. Koumoto, H. Yanagida, Seramikkusu Ronbunshi, 97,
   1170-75 (1989).
5) H. Suzuki and T. Hase, J. Am. Ceram. Soc. 63, 349-50 (1980).
6) H. Suzuki, Ceramics, 18, 3-9 (1983).

Formation of Epitaxial Pb(Zr, Ti)O₃ Film by CVD

Hiroshi Funakubo, Katsuhiro Imashita, Nobuo Kieda and Nobuyasu Mizutani

Department of Inorganic Materials, Faculty of Engineering, Tokyo Institute of Technology,
2-12-1, O-okayama, Meguro-ku, Tokyo 152, Japan

$Pb_x(Zr_y, Ti_{1-y})O_3$ films were prepared by CVD using $Pb(DPM)_2$, $Zr(OÁt-Bu)_4$, $Ti(OÁi-Pr)_4$ and O_2 as starting materials. Metal alkoxide was selected for both Ti and Zr starting materials, which were effective for controlling Ti and Zr contents in the films. PZT films with the composition, x = ca. 1.0 and y = ca. 0.5, were grown repeatedly with almost complete epitaxy on (100) MgO substrate. Film deposition rate of film was about 200 - 300nm/min.

1. Introduction

$Pb_x(Zr_y, Ti_{1-y})O_3$, PZT, has been widely used as a piezoelectric material because of its excellent properties. The thin films having the polar axis perpendicular to the substrate, especially epitaxial films, are more useful for the applications to various devices. The polarization axis of tetragonal PZT is parallel to the <001> axis. However, it is known that piezoelectric properties of PZT depend on its composition and crystal structure,[1] so that precise controls of composition and crystallinity are required. Various techniques such as sputtering,[2-5] laser ablation,[6] ion beam deposition,[7,8] and electron beam evaporation[9] have been applied to the preparation of PZT films. Moreover, preparation from the liquid phase (such as by metallo-organic decomposition,[10] (MOD) and sol-gel techniques,[11,12]) has also been reported.

The most widely accepted deposition technique of tetragonal PZT film with c-axis orientation is the sputtering method. However, difficulty in the precise control of composition and structure in the bulk of the film still remains. In CVD, it is relatively easy to precisely control film composition and crystallinity, which has led to wide use in the crystal growth of semiconductors. However, the preparation of PZT film by CVD has hardly been reported. Okada et al.[13] reported the preparation of c-axis oriented PZT films on (100) MgO substrate by CVD using $Pb(C_2H_5)_4$, $Zr(DPM)_4$, $Ti(O·i-Pr)_4$ and O_2 as starting materials. However, epitaxial growth was not ascertained. Moreover, they also reported that c-axis oriented film was not obtained when $Zr(O·i-Pr)_4$ was used instead of $Zr(DPM)_4$.

In this paper, PZT films were prepared on (100) MgO substrates by CVD using Ti tetra-isopropoxide [$Ti(O·i-Pr)_4$], tetra-tertiary butokyzirconium [$Zr(O·t-Bu)_4$], bis(dipivaloyl methanato) lead [$Pb(DPM)_2$] and O_2 as starting materials. Metal alkoxide was selected for both Ti and Zr staⁱting materials, which were effective for controlling Ti and Zʳ contents of the films. An almost epitaxially grown film

with a composition of x = ca. 1.0 and y = ca. 0.5 was obtained with good reproducibility. This composition was almost equivalent to one showing excellent piezoelectric properties.

2. Experimental Procedure

The schematic diagram of CVD apparatus for PZT film was almost the same one as previously reported elsewhere.[14] $Ti(O·i-Pr)_4$ and $Zr(O·t-Bu)_4$ vapor were generated by bubbling N_2 through each liquid. On the other hand, $Pb(DPM)_2$ vapor was generated by heating its powders and carried with N_2. The flow rates of each carrier N_2 gas were regulated by precise needle valves and measured by flow meters. These vapors were mixed with O_2 and N_2 (balancing gas to make the total gas flow rate constant). The gas mixture was introduced into a cold-wall type CVD reactor ($77mm\phi \times 350mm$) through a nozzle (internal diameter: 14mm) and flowed against the (100) MgO substrate ($0 \times 10 \times 0.5mm^3$). The gas line was heated to prevent the condensation of each vaporized starting material. The deposition conditions for the PZT films with x = ca. 1.0 and y = ca. 0.5 are summarized in **Table 1**.

The constituent phases and orientation of the film were identified by an X-ray powder diffractometer(XRD) (Philips PW-1700). The texture of the film was obtained from an X-ray pole figure device (Philips PW1078/50). Microstructures and compositions of the films were observed using SEM (JEOL JSM-T-200) with EDS (Philips PV9900).

3. Results and Discussion

The films deposited on the substrates were transparent and slightly whitish in color. The growth rate was about 200 - 300nm/min, which was more than 10 times as fast as that of dc or rf sputtering methods. The films adhered well to the substrates.

Table 1. Deposition conditions of PZT film.

Precursor	Pb : $Pb(DPM)_2$
	Zr : $Zr(O·t-Bu)_4$
	Ti : $Ti(O·i-Pr)_4$
Temperature of vaporizer	Pb : 165 °C
	Zr : 50 °C
	Ti : 42 °C
Flow rate of carrier for each component	Pb : 180 ml/min (N_2)
	Zr : 40 ml/min (N_2)
	Ti : 40 ml/min (N_2)
	O_2 : 40 ml/min (N_2)
Total gas flow rate	: 480 ml/min
Total gas pressure	: 20 Torr
Deposition temperature	: 700 °C
Substrate	: (100) MgO
	(10mm x 10mm x 0.5)
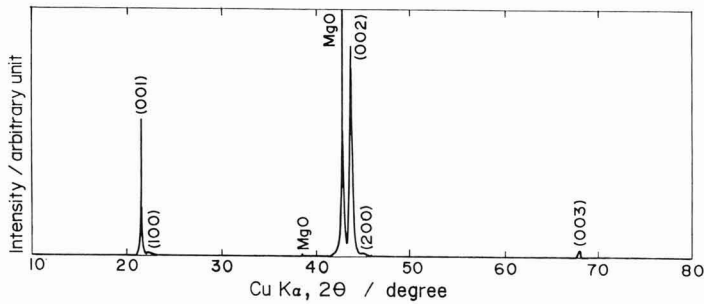
Fig. 1. XRD pattern of PZT film on (100) MgO substrate.

(a)(001), (b)(101)

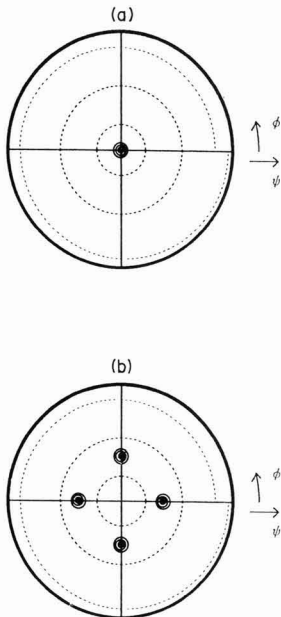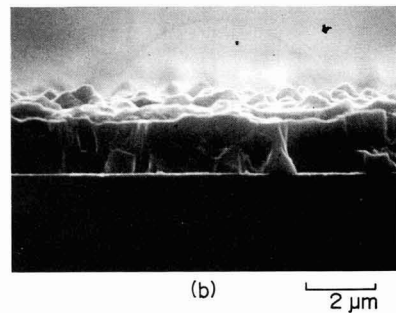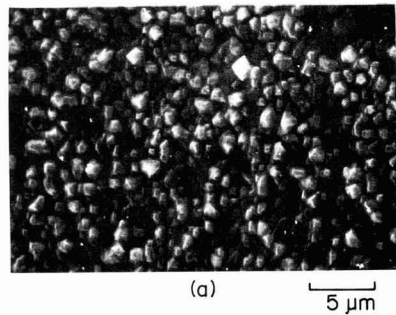**Fig. 2.** X-ray pole figures of the PZT film.

Fig. 3. SEM micrographs of PZT film.
(a)surface, (b)fractured surface

Figure 1 shows an XRD pattern of the film. Only (00l) and (h00) peaks of tetragonal PZT were observed together with those of MgO, and the intensities of (00l) reflections were significantly stronger than those of (h00) ones. The degree of c-axis orientation was $\alpha = \Sigma I(00l)/\Sigma I(hkl)$, where I(00$l$) and I($hkl$) represented the X-ray diffraction intensities of (00l) and (hkl) reflections. The α of PZT film for Fig.1 was about 0.9, which suggests that the PZT films are highly <001> oriented.

Figure 2 shows (001) and (101) X-ray pole figures of the same PZT film as that for Fig.1. ϕ is the rotation axis perpendicular to the film plane and Ψ is the rotation axis perpendicular to ϕ and θ. The (001) pole was observed only at the center, $\phi = 0°$, in **Fig.2(a)** which shows that the film has highly preferred [001] orientation. Moreover, as shown in **Fig.2(b)**, high concentrations of (101) poles were observed at a radius corresponding to $\Psi = 45°$ and every 90°

along ϕ. This result shows that there is not only a crystal structural arrangement having an axis perpendicular to the substrate, but also that with a parallel one.[15] From the result of Figs.1 and 2, the PZT film was considered to be almost completely epitaxially grown on (100) MgO substrate.

The reproducible preparation of PZT films with x = ca. 1.0 and y = ca. 0.5, was ascertained by EDS measurement. This composition was in good agreement with the estimated values by the lattice parameter of the film as compared with those reported by Kakegawa et al.[16]

Figure 3 shows SEM micrographs of the same PZT film. The PZT film was dense and made up of fine grains. Okada et al.[13] reported the dependence of density of the film on the ratio of Zr to Ti. However, in the present study, PZT film was dense irrespective of film composition.

4. Conclusion

Almost completely epitaxially grown $Pb_x(Zr_y, Ti_{1-y})O_3$ films with the composition of x = ca. 1.0 and y = ca. 0.5 were successfully prepared on (100) MgO substrate by CVD using $Pb(DPM)_2$, $Zr(O \cdot t\text{-}Bu)_4$, $Ti(O \cdot i\text{-}Pr)_4$ and O_2 as starting materials. The deposition rate of the film was about 200 - 300nm/min.

The detailed preparation and properties of the films will be described later in a full-length paper.

References:

1) B. Jaffe, R. S. Roth and S. Marzulle, J. Res. Nati. Bur. Stand., 55, 239-254(1955).

2) A. Okada, J. Appl. Phys., 48, 2905-2909 (1977).

3) S. B. Krupanidichi and M. Sayer, J. Vac. Sci. & Technol., A2, 303-306(1984).

4) T. Fukami, T. Sakuma, K. Tokunaga and H. Tsuchiya, Jpn. J. Appl. Phys., Suppl.22-2, 18-21(1983).

5) R. Takayama and Y. Tomita, J. Appl. Phys., 65, 1666-1670(1989).

6) S. Otsubo, T. Maeda, T. Minamikawa, Y. Yonezawa, A. Morimoto and T. Shimizu, Jpn. J. Appl. Phys., 29, L133-136(1990).

7) R. N. Castellano, Ferroelectrics, 28, 387-390(1980).

8) R. N. Castellano and L. G. Feistein, J. Appl. Phys., 50, 4406-4411(1979).

9) M. Oikawa and K. Toda, Appl. Phys. Lett., 29, 491-492(1976).

10) J. Fukushima, K. Kodaira and T. Matsushita, J. Mater. Sci., 19, 595-98(1984).

11) T. Suzuki, M. Matsuki, Y. Matuda, K. Kobayashi and Y. Takahashi, J. Ceram. Soc. Jpn., 98, 754-58(1990).

12) G. Yi, Z. Wu and M. Sayer, J. Appl. Phys, 74, 2717-24(1988).

13) M. Okada, K. Tominaga, T. Araki, S. Katayama and Y. Sakashita, Jpn. J. Appl. Phys., 29, 718-722(1990).

14) K. Imashita, H. Funakubo, N. Kieda and N. Mizutani, Nippon Kagaku Kaishi, 1395-1401(1990).

15) H. R. Wenk, "Preferred Orientation in Deformed Metals and Rocks: An Introduction to Modern Texture Analysis", Academic Press (1985) pp11-47.

16) K. Kakegawa, J. Mohri, S. Chiba, S. Sirasaki and K. Takahashi, Nippon Kagaku Kaishi, 717-721(1976).

Information & Communications

News

Ceramics, Japan '91

The Ceramic Society of Japan will celebrate its centenary in October, marketing the expansion of its activity area from the traditional ceramic and glass industries to a variety of high-technology fields including those of high-temperature, functional, electronic, optoelectronic, and biotechnological materials. As part of the centennial events, the Society is planning to hold "Ceramics, Japan '91" exhibition from October 16 through 20 with the principal theme of "Ceramics towards the 21th Century." Nikkan Kogyo Shimbun will support the event, which will take place at Pasifico's Yokohama Exhibition Hall. There are three areas in the hall: (1) the Society's zone, (2) the participants' zone, and (3) the ceramics enlightenment corner. The exhibits cover (1) building and civil engineering, (2) chemicals, metals and ceramics, (3) energy, nuclear and electrical power, (4) machinery and precision products, (5) electronics, information and communications, (6) transportation, (7) aerospace devices and underwater structures, (8) bio- and life-sciences, (9) printing, cosmetics and toys, (10) domestic affairs and sports, and (11) traditional ceramic products.

Silicon Carbide Thin Films

Prof. T. Inada and his colleagues of the Faculty of Engineering at Hosei University have deposited a thin film of silicon carbide on a silicon substrate at low temperature by the CVD method, where evaporated carbon from 99.999% pure graphite is directed onto an N-type silicon substrate placed in a container kept at 10^{-6} Torr (the method is named direct carbonization). Carbon deposited on the substrate grows epitaxially when the substrate is heated to 1000°C to form a thin film of β-type silicon carbide at 0.001μm/min. It was confirmed by RHEED and XRD analyses that a high-quality, amorphous film of β-type silicon carbide was formed on the substrate. A superhigh-speed element, better than a gallium-arsenic device, may be realized when silicon carbide is used as the emitter of a bipolar transistor. The researchers are planning to develop such devices using the thin films.

Alumina Fibers of 7μm in Diameter

Daimei Kagaku Kogyo has developed alumina fibers of 7μm in diameter, and commercialized a long fiber bundle consisting of 500 alumina fibers. Fibrous alumina is a good insulating material highly resistant to heat and corrosion, and having a length of several cm it has been used for insulators. Three Japanese companies, including Daimei Kagaku, have produced long alumina fibers, but only of 10μm in diameter. The finer fibers will exhibit better properties. The company is sending the samples to prospective users (price: 120,000yen/kg), and plans to construct a commercial plant for alumina fiber fabrics.

Precision Abrasive of Diamond

Sumitomo 3M has developed and started selling precision diamond abrasive which is at least twice as good as conventional ones in cutting characteristics and durability. High-technology industries such as communications, information electronics and aerospace are currently developing very hard materials (i.e. new alloys and ceramics) and becoming increasingly dependent on advanced finishing and precision grinding techniques. The new abrasive is characterized by fine diamond particles metal- or resin-bonded to flexible fibers. The structure in which abrasive pellets are orderly arranged is more resistant to clogging and radiates heat more efficiently. The abrasive base, being flexible, makes the abrasive more compatible with surface curvatures of the object to be polished, and allows finishing those parts inaccessible to conventional abrasives. There are eight types by grain size (from 2μm to 250μm) and two types by function (one has pressure-sensitive adhesives, and the other a removal fastener on the bake). The price is 11,000 yen for a 10cm square sheet. The company is planning to expand its applications to belts and discs.

High-Purity Alumina Ceramics

Toshiba Ceramics has established an FC business promotion department to develop the markets of a variety of ceramic products on a full scale. Based on ceramic filters and transparent products of high-purity alumina. The company has been producing a variety of apparatus for the food and bio-related industries which incorporates filters of high-purity alumina introduced by France's S.C.T. Recent demand in the semiconductor industry for inline gas filters is increasing to meet the requirements of more integrated circuit production lines. The filter of high-purity alumina (99.9% or more) will allow highly accurate filtration of 0.01μm or less, due to improved flow characteristics of its unique nonsymmetrical, multi-layered structures. The element has a mechanical strength of 175kg/cm^2, sufficiently resistant to excessive flow or pressure. The transparent alumina ceramics are produced by the company's proprietary technology originally developed for artificial sapphire. A high-purity, high-density alumina sinter consisting of 30 to 40μm grains, its characteristics closely resemble those of single-phase alumina to allow almost all visible rays to diffuse through the body. The major area of application at present is a light tube for sodium-vapor lamps. Prospective applications (thanks to its heat-resistance -- up to 1850°C) include: laser-related devices, sheaths for high-temperature thermocouple, metal-melting crucibles, infrared ray transmitting materials, microwave transmitting materials, and semiconductor-related materials. The article size can be increased to 120mm in diameter and 3000mm in length, which will further expand its applicable areas.

Zeolite-Base Antimicrobial, Deodorization-Type Ultrasonic Humidifier

Sinanen New Ceramics is selling zeolite-base antimicrobial, deodorizing-type ultrasonic humidifiers in which the water tank is lined with an antimicrobial sheet of urethane coated with zeolite to keep the tank free of bacteria. The zeolite coating works as an inorganic antimicrobial agent of alkaline aluminosilicate. Ultrasonic vibration of service water in the tank release chlorine as a microbial agent, with the result that water tends to be contaminated with various bacteria. This contamination is effectively prevented by the zeolite coating. Humidifiers, which prevent excessive dryness in a room, are attracting attention as devices to prevent influenza. The company has sold 40,000 units since 1989, and with the addition of 4*l*- and 1*l*-types, hopes to expand sales to 80,000 units in 1991.

Production of Polycrystalline (Artificial Diamond)

Sumitomo Coal Mining plans to commercially produce polycrystalline (artificial diamond) which is finer in surface texture and hence more suited for grinding purposes than the single-crystal type. It will allow precise grinding to 0.01μm or less. An "impact compression method," based on coal mining
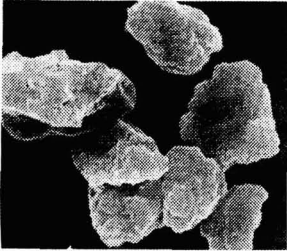
Photo 1. Artifical diamond

blasting techniques, will be used in which a double-wall cylinder (30cm in diameter, 80cm high) is packed with explosives (in the annular space) and graphite. The explosives will create a pressure of some 500,000 atm and a temperature of 2000°C, to produce polycrystalline diamond instantaneously. The test apparatus is capable of producing 100 carats worth of diamond a day. The company has been increasing the production capacity to 250 carats/day by developing a larger cylinder of improved material, and plans to construct a commercial plant in a closed coal mine in Hokkaido. The projected initial production is 2 million carats a year.

Higher Critical Temperature Bismuth Superconducting Oxide

A research group consisting of Okayama University, the National Defense Academy, and the Institute for Chemical Research of Kyoto University have reported the successful processing of a new bismuth superconducting oxide which has a high temperature phase and a critical temperature of 115K.

The group used a lead-rich starting composition. Even when ordinary processing technology was used, the critical temperature was over 110K, and the best figure obtained was 116K. They added 0.34 of lead to the usual starting composition of 0.96 bismuth, 0.24 lead, 1.0 strontium, and 1.1 calcium. The starting raw materials were the nitrates of each element, and precursor powder was obtained by the oxalate method. After drying and heating, the well-mixed powder was presintered at 800°C for 12 hrs. A pellet 20mm in diameter was prepared from this raw material by crushing, mixing and pressing, and was sintered at 845 to 855°C for 24 to 300 hrs. The resulting material contained a trace of Ca_2Pb and the low-temperature phase compound as well as the high-temperature compound. The critical temperature went to 115K and up. The result of a complex magnetization measurement which gave 117K showed that a new higher critical temperature bismuth material had been achieved.

Magnetic Force of 2500 Gauss

Nippon Steel Corp. has reported the successful development of a high-level yttrium-family superconducting oxide with a magnetic force of 2500 gauss. The success came from increasing the crystal size from 1 to 3cm square, and the company said that it was possible to produce crystals up to 6cm square.

Using a high-quality rare-earth permanent magnet, a weight of 1kg was suspended. The magnetic power of the superconducting oxide depended on the crystal size which was included in the bulk material, and could be increased by obtaining bigger crystals and decreasing grain boundary layers. Nippon Steel Corp. was successful in making larger crystals by using an improved melting process called the QMG method and by making uniaxial growth of the crystal. The raw material was melted at about 1400°C. After a second melting at 1200°C, the sample was held at 1100°C for 30min., and cooled at a rate of 1°C per hour to obtain a conical superconducting oxide 4cm in diameter and 7cm high.

Minute Resistivity Measurement Apparatus for Superconductors

Stabilizer Co., Ltd. has obtained a licence for a "stabilized constant direct voltage circuit system for superconductivity measurement" which can measure the differential output of superconductor resistivity with stability below 10^{-6}. It plans to install this in its "Power Source for Superconducting Magnets" and sell it for research purposes. This stability was obtained by adding a response circuit for slow varying signals with a noise filter and time-position spontaneous measuring circuit. The main parts were encapsulated in a thermostat to avoid the influence of temperature variation on the sample. Lower cost and standardization were also established.

Metal Oxide Fine Powder Process

Prof. T. Matsuda and his group at Saitama University have developed new microwave low temperature plasma heating technology by which metal oxide fine powder which has a broader surface can be processed in a short time. The resulting diameter is controllable within 50 angstrom to a few microns. For example, 10 grams of magnesium hydroxide encapsulated in glass tubing was evacuated and irradiated with 100- watt, 2.45GHz micro-waves and in 5 minutes gave magnesia fine powder of a surface as large as 372 square meters per gram. (Conventional electric furnaces produce fine powder with a surface of approximately 100 to $150m^2$). A high quality substrate for superconducting oxide thin film can be prepared with the fine powder obtained by using this new technology.

Bismuth-Family Thin Film

Oki Electric Co. has developed a thin film from bismuth family superconducting oxide on a silicon substrate, thereby establishing a prospects for making high temperature superconductor bipolar transistors. The film is a copper layer of two or three atomic thicknesses on substrate, on which a 0.1 micron bismuth family thin film was formed at 530°C; subsequently a 0.3 micron-m bismuth family thin film was formed at 700°C. The critical temperature was 20K. The reason two steps were used for forming bismuth layers was to prevent vaporization of copper above 530°C. It aims to develop a transistor structure which has a bismuth-family superconducting oxide base. Until now, ceramic layers formed to avoid mutual diffusion reactions between silicon and bismuth prevented current flowi.

Raw Materials for Superconducting Oxide Films

Nippon Sanso K.K. has developed and started sales of raw materials for high temperature superconducting oxide films by a metal oxide chemical vapor deposition method(MOCVD) of organic metal compounds. It developed a high-productivity original organic process and was successful in the purification of raw barium and strontium which were considered difficult to purify. The raw materials are sold in 10 gram ampules, and the cost per gram will be about 6,000 yen. The hygroscopicity of barium and strontium was a barrier to obtaining high purity raw materials for making films. Nippon Sanso was able to make 99% high purity raw

materials using original semi-conductor processing technology as well as organic processing technology of the Isotech Corp., a US company with which it cooperated.

Critical Temperature of 127K

Matsushita Electronic Industry Co. has reportedly raisied the highest critical temperature record of the thallium-family superconducting oxide from 125K to 127K. The key was to keep the sintering process temperature low and prolong. The Meissner effect was confirmed at 127.2K and the temperature which gave zero electrical resistance was 124.9K. Until now, the highest critical temperature of high temperature superconductor was 125K which was measured by IBM who also did the double checking on the 1988 report from Prof. Herman of Alabama University. The critical temperature reported from other laboratories was around 122K.

Ceramic Liner

Matsuzaka Boeki's "AS-MK II" ceramic liner is attracting attention again, this time as a result of the Gulf Crisis, to protect blowing tubes in coal-fired boilers and blast furnaces. A total of 200 tons of the liner was sold in the past 2 years, which is finer (particle size: 2 to 3μm), harder, more slippery and roughly 10 times more resistant to wear than conventional liners. Its compressive strength is 19700 to 26700kg/cm^2, and it can be installed by gluing or welding. Its demand as a wear-resistant material is also increasing for various industrial machines such as mixers, classifiers and pneumatic transportation machines. The company is expecting an annual
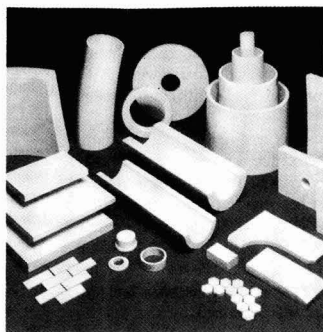
Photo 1. New ceramic liner.

demand of 1500 tons.

Shirasu Porous Glass

Shirasu porous glass (SPG), produced from Shirasu volcanic ash as the starting material, has been commercialized by three companies (Fuji Davison Chemicals, Ise Kagaku Kogyo and Ohtsu Tire) and licensed by the Miyazaki Prefectural Industrial Insti-
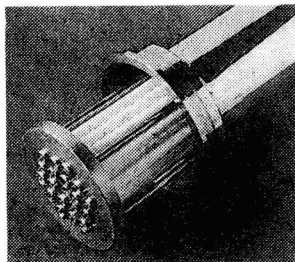
Photo 1. Separation membrane module which employs shirasu porous glass.

tute which developed the production process. SPG is characterized by a porous structure in which a number of fine pores ($1/10^6$ to 1/102mm) are interwoven with each other. The pore size of one SPG type is fairly uniform and can be designed freely. Being glass, it can be easily shaped into plates, pipes, fibers, particles and so on. The first commercial applications are the pipes to support filter membranes for purifying wine and vinegar. Finely powdered SPG is also used as a filler for superhigh-speed liquid chromatography. Ohtsu Tire is planning to apply SPG to air purifiers.

New Method for Manufacture of LBO Single Crystal

In co-operation with Ohkura Electric Co., Ltd., Mr. Tohru Katsumata, lecturer of the Faculty of Engineering of Toyo University has succeeded in the growth of a single crystal of tetra-lithium of boric acid (LBO) by the horizontal Bridgeman method. The LBO single crystal has excellent properties as a substrate material for surface acoustic wave (SAW) elements in television sets, pagers and so on. The new manufacturing process can produce high-quality single crystals at low cost (from 1/5 to 1/10 that of conventional ones made with the Czochralski (CZ) process using a platinum crucible).
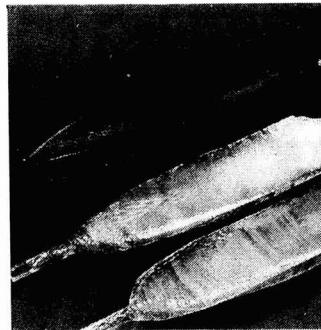

Photo 1. LBO single crystal and graphite.

The new process uses a boat of graphite with an inferior wetting property which does not react with the LBO single crsytal. The powder of high purity boric acid tetra-lithium and seed crystals are placed in the boat. The single crystals are grown by moving the boat at a speed of 0.4 to 1mm per hour in a kiln with a temperature gradient from 60°C to 1000°C. The new process can be applied to reduce the manufacturing costs of β-barium of boric acid and tri-lithium of boric acid single crystals, which will be used as non-linear optical materials.

Higher Critical Temperature Bismuth Superconducting Oxide

A research group consisting of Okayama University, the National Defense Academy, and the Institute for Chemical Research of Kyoto University have reported the successful processing of a new bismuth superconducting oxide which has a high temperature phase and a critical temperature of 115K.

The group used a lead-rich starting composition. Even when ordinary processing technology was used, the critical temperature was over 110K, and the best figure obtained was 116K. They added 0.34 of lead to the usual starting composition of 0.96 bismuth, 0.24 lead, 1.0 strontium, and 1.1 calcium. The starting raw materials were the nitrates of each element, and precursor powder was obtained by the oxalate method. After drying and heating, the well-mixed powder was pre-sintered at 800°C for 12 hrs. A pellet 20mm in diameter was prepared from this raw material by crushing, mixing and pressing, and was sintered at 845 to 855°C for 24 to 300 hrs. The resulting material contained a trace of Ca_2Pb and the low-temperature phase com-

pound as well as the high-temperature compound. The critical temperature went to 115K and up. The result of a complex magnetization measurement which gave 117K showed that a new higher critical temperature bismuth material had been achieved.

Raw Materials for Superconducting Oxide Films

Nippon Sanso K.K. has developed and started sales of raw materials for high temperature superconducting oxide films by a metal oxide chemical vapor deposition method(MOCVD) of organic metal compounds. It developed a high-productivity original organic process and was successful in the purification of raw barium and strontium which were considered difficult to purify. The raw materials are sold in 10 gram ampules, and the cost per gram will be about 6,000 yen. The hygroscopicity of barium and strontium was a barrier to obtaining high purity raw materials for making films. Nippon Sanso was able to make 99% high purity raw materials using original semi-conductor processing technology as well as organic processing technology of the Isotech Corp., a US company with which it cooperated.

Magnetic Force of 2500 Gauss

Nippon Steel Corp. has reported the successful development of a high-level yttrium-family superconducting oxide with a magnetic force of 2500 gauss. The success came from increasing the crystal size from 1 to 3cm square, and the company said that it was possible to produce crystals up to 6cm square.

Using a high-quality rare-earth permanent magnet, a weight of 1kg was suspended. The magnetic power of the superconducting oxide depended on the crystal size which was included in the bulk material, and could be increased by obtaining bigger crystals and decreasing grain boundary layers. Nippon Steel Corp. was successful in making larger crystals by using an improved melting process called the QMG method and by making uniaxial growth of the crystal. The raw material was melted at about 1400˚C. After a second melting at 1200˚C, the sample was held at 1100˚C for 30min., and cooled at a rate of 1˚C per hour to obtain a conical superconducting oxide 4cm in diameter and 7cm high.

Minute Resistivity Measurement Apparatus for Superconductors

Stabilizer Co., Ltd. has obtained a licence for a "stabilized constant direct voltage circuit system for superconductivity measurement" which can measure the differential output of superconductor resistivity with stability below 10^{-6}. It plans to install this in its "Power Source for Superconducting Magnets" and sell it for research purposes. This stability was obtained by adding a response circuit for slow varying signals with a noise filter and time-position spontaneous measuring circuit. The main parts were encapsulated in a thermostat to avoid the influence of temperature variation on the sample. Lower cost and standardization were also established.

Metal Oxide Fine Powder Process

Prof. T. Matsuda and his group at Saitama University have developed new microwave low temperature plasma heating technology by which metal oxide fine powder which has a broader surface can be processed in a short time. The resulting diameter is controllable within 50 angstrom to a few microns. For example, 10 grams of magnesium hydroxide encapsulated in glass tubing was evacuated and irradiated with 100- watt, 2.45GHz micro-waves and in 5 minutes gave magnesia fine powder of a surface as large as 372 square meters per gram. (Conventional electric furnaces produce fine powder with a surface of approximately 100 to 150m$^{2)}$). A high quality substrate for superconducting oxide thin film can be prepared with the fine powder obtained by using this new technology.

Bismuth-Family Thin Film

Oki Electric Co. has developed a thin film from bismuth family superconducting oxide on a silicon substrate, thereby establishing a prospects for making high temperature superconductor bipolar transistors. The film is a copper layer of two or three atomic thicknesses on substrate, on which a 0.1 micron bismuth family thin film was formed at 530˚C; subsequently a 0.3 micron-m bismuth family thin film was formed at 700˚C. The critical temperature was 20K. The reason two steps were used for forming bismuth layers was to prevent vaporization of copper above 530˚C. It aims to develop a transistor structure which has a bismuth-family super-

conducting oxide base. Until now, ceramic layers formed to avoid mutual diffusion reactions between silicon and bismuth prevented current flowi.

Critical Temperature of 127K

Matsushita Electronic Industry Co. has reportedly raisied the highest critical temperature record of the thallium-family superconducting oxide from 125K to 127K. The key was to keep the sintering process temperature low and prolong. The Meissner effect was confirmed at 127.2K and the temperature which gave zero electrical resistance was 124.9K. Until now, the highest critical temperature of high temperature superconductor was 125K which was measured by IBM who also did the double checking on the 1988 report from Prof. Herman of Alabama University. The critical temperature reported from other laboratories was around 122K.

Instantaneous Calorimeter

The National Research Laboratory of Metrology has developed an instrument that utilizes a laser beam to measure the specific heat of high-temperature materials of more than 700˚C.

Since high-temperature material bodies have a large thermal loss by radiation, the general specific heat measuring method can not be used as measurement takes too long due to the largeness of the machine..

The laser flash differential calorimeter irradiates a narrow, focused laser beam to a sample and measures temperature changes in the rear side of the sample using a radiation thermometer. The same operation is simultaneously performed for a standard sample of sapphire (for which specific heat is known) at each temperature from very low temperatures to about 2,000˚C. The specific heat of the sample can then be determined by comparing the measured results of both samples. As the temperature increase of the sample by laser takes less than 0.1 second, the specific heat can be measured in a very short period of time.

The application of lasers for specific heat measurement will allow the determination of thermal properties of new materials such as nuclear fuels and heat-resistant ceramics exposed to high temperatures.

Superconducting Oxide Shielding Equipment

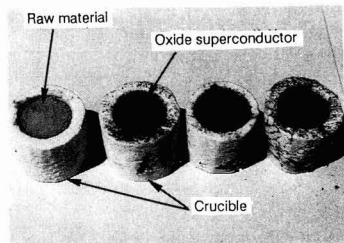Mitsui Metal Co. and Sumitomo Heavy Industries collaborated to develop the

Photo 1. Yttrium system acid superconductor and its material.

ZEROMAG, a piece of equipment used in low magnetic field shielding under the leadership of the Institute of Physical and Chemical Research. The device consists of a bismuth-family superconducting oxide vessel, a cryostat, and a closed-loop helium refrigerator. The dimensions of the shielding vessel are 90mm in diameter and 300mm in height, and it exhibits shielding perfor-mance of minus 100 decibels for a low magnetic field at a frequency of 0.2 Hz. Both companies plan to sell 20 zeromags to universities and research institutes in the first year. The price will be approximately 15 million yen

Robot for Preparation of Superconducting Oxide Samples

The Superconductivity Research Laboratory in cooperation with Toyo Engineering Co. reported that they have built an automatic multi-sample preparation machine which can prepare eight kinds of superconducting oxide samples at once. The machine can quickly produce a variety of samples which have different compositions and it also has good reproducibility in delicate sample preparation. The weighing, mixing, drying and forming steps are all automated. The steps of presintering, crushing and final forming will be introduced by the end of this fiscal year. The current machine gave maximum 20 kinds of samples, and eighty samples a day. The cost will be approximately 300 million yen.
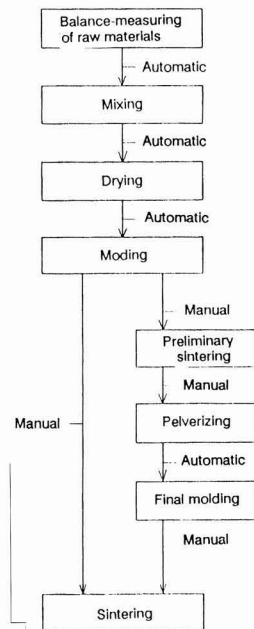
Fig. 1. Flow chart for automatic multi-sample mixing processes.
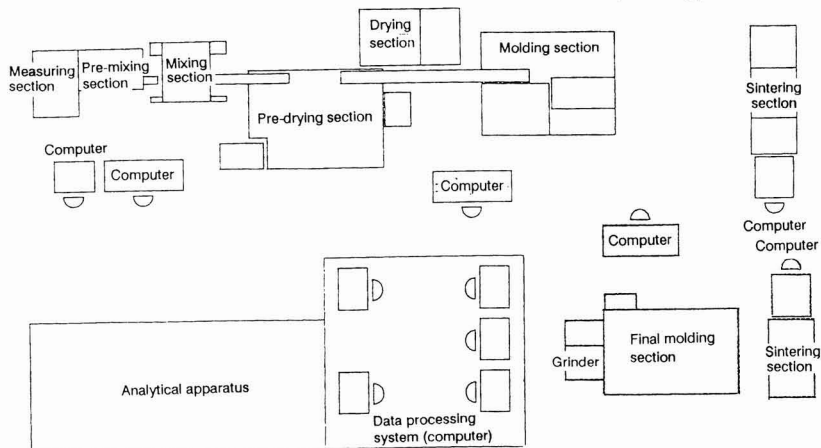
Fig. 2. Automatic multi-sample mixer.

Abstracts of Articles on Ceramics from the Selected Journals of the Academic Societies

Manufacture of Lightweight Aggregates Utilizing Coal Fly Ash

Kuniyoshi ISHII

(Kyushu Electric Power Co. Inc.)

SYNOPSIS ： — In establishing coal firing power plants, the processing of a large amount of coal ash generated from the plants is becoming a serious problem and the development of the technology to effectively utilize a large amount of coal ash as a resource is expected.

In accordance with such social demands, Kyushu Electric Power Co. Inc., Kyuden-sangyo Co. Inc., and Kobe steel, Ltd. jointly succeed in development of the technology of manufacturing the lightweight aggregates which was expected to enable to effectively utilize a large amount of coal fly ash. The product has been brought to market under the brand name of FA-LIGHT.

FA-LIGHT is produced by the sintering process utilizing the unburned carbon left in coal fly ash, after the green pellets agglomerated by the mixed and premoistened fly ash are ignited by the pulverized coal firing burner.

This technology can make a great contribution to the recycling of industrial waste, compared with the conventional process to manufacture the lightweight aggregates from shale with the rotary kiln system, because the process effectively utilizes a large amount of coal fly ash of industrial waste and consume less fuel by adopting of the sintering method utilizing the unburned carbon left in coal fly ash.

Key Words
Coal fly ash, Lightweight aggregates, Effective utility

Appearance of a Maximum of T_c and a Large Negative dT_c/dP in the Superconducting Tl–Ba–Ca–Cu–O Compounds under Pressure

Nobuo MÔRI, Hiroki TAKAHASHI, Yuichi SHIMAKAWA,[†] Takashi MANAKO[†] and Yoshimi KUBO[†]

Institute for Solid State Physics, University of Tokyo, Roppongi, Minato-ku, Tokyo 106
[†]*Fundamental Research Laboratories, NEC Corporation, 4-1-1 Miyazaki, Miyamae-ku, Kawasaki 213*

The pressure dependence of T_c for the superconducting Tl–Ba–Ca–Cu–O compounds has been measured. It is found that the pressure coefficients of T_c in $Tl_2Ba_2CaCu_2O_8$ change the sign from positive to negative with a maximum T_c and that the highly hole-doped $Tl_2Ba_2CuO_6$ compounds show a large negative value of dT_c/dP. These results revealed a new feature of the pressure dependence of T_c in the hole-doped superconductors and can be interpreted speculatively in terms of the hole concentration in the CuO_2 planes assuming that the carrier concentration is redistributed with pressure.

[superconductivity, pressure effects, copper oxides]

Superconductivity and Phase Transition of Zirconium under High Pressure up to 50 GPa

Yuichi AKAHAMA, Mototada KOBAYASHI and Haruki KAWAMURA

Department of Material Science, Himeji Institute of Technology,
Himeji, Hyogo 671-22

The superconducting transition temperature, T_c, of group-IV transition metal zirconium has been studied as a function of pressure up to 50 GPa in relation to the pressure-induced structural phase transition. Corresponding to a phase transition from hexagonal to bcc structure, a discontinuous increase of the T_c is observed at 30 GPa. For the bcc phase, a high T_c of 11 K has been developed. The result suggests that an electronic configuration similar to that of the bcc Nb is induced in the bcc phase as a result of an increase in valence d-electron numbers by the s-d electronic transformation. The observation of the high T_c is decisive experimental evidence for a pressure-induced transformation from group-IV transition metal to group-V transition metal.

superconductivity of zirconium, high pressure, s-d transition, pressure-induced phase transition, d transition metal

^{63}Cu NMR Study of Spin Dynamics in $La_{2-x}(Sr, Ba)_x CuO_y$ $(0.04 \leq x \leq 0.16, 3.99 \leq y \leq 4.03)$

Takashi IMAI, Kazuyoshi YOSHIMURA,[†] Takashi UEMURA,[†]
Hiroshi YASUOKA and Koji KOSUGE[†]

The Institute for Solid State Physics, The University of Tokyo,
7-22-1 Roppongi, Minato-ku, Tokyo 106
[†]Department of Chemistry, Faculty of Science, Kyoto University,
Sakyo-ku, Kyoto 606

The ^{63}Cu nuclear spin-lattice relaxation rate $1/T_1$ has been measured for oriented powders of $La_{2-x}(Sr, Ba)_x CuO_y$ in a wide concentration range. The spin dynamics in a lightly doped nonsuperconductor, $La_{1.96}Sr_{0.04}CuO_{4.02}$, is found to be qualitatively similar to that of a moderately doped high T_c superconductor, $La_{1.85}Sr_{0.15}CuO_{4.03}$. The antiferromagnetic correlation length in the latter is estimated to be reduced by a factor of ~ 2. The normal state spin dynamics has been successfully observed down to liquid helium temperature for $La_{1.88}Ba_{0.12}CuO_{4.00}$. The result showed a monotonous decrease of $1/T_1$ with somewhat sublinear temperature dependence below 100 K.

^{63}Cu, NMR, spin dynamics, high temperature superconductivity, $La_{2-x}Sr_x CuO_4$, $La_{2-x}Ba_x CuO_4$

Vacancy-Type Defects in As^+-Implanted SiO_2(43 nm)/Si Proved with Slow Positrons

Akira UEDONO*, Shoichiro TANIGAWA, Jun SUGIURA[†]
and Makoto OGASAWARA[†]

Institute of Materials Science, University of Tsukuba, Tsukuba, Ibaraki 305
[†]Device Development Center, Hitachi Ltd., 2326, Imai, Ome-shi, Tokyo 198

Variable-energy positron-beam studies have been made on 150-keV As^+-implanted SiO_2(43 nm)/Si specimens. From measurements of Doppler braodening profiles of the positron annihilation as a function of incident positron energy, it was found that the region of vacancy-type defects induced by As^+-implantation extends far beyond the As-stopping profile. The dominant defect species was identified as a divacancy from the characteristic value of the line-shape parameter. The defect concentration of the damaged region for the specimens with the doses of $5 \times 10^{14} \sim 5 \times 10^{15}$ As/cm^2 was estimated as 1×10^{21} cm^{-3}. The effect of isochronal annealing is also discussed.

KEYWORDS: positron, monoenergetic positron beam, silicon, defect, ion implantation, oxide semiconductor interface

*Present address: Department of Physics, Yokohama City University,
22-2, Seto Kanazawa-ku, Yokohama 236.

Critical Current Densities in Superconducting Y–Ba–Cu–O Prepared by Chelating Method

Tadashi FUJISAWA, Akira TAKAGI[†], Katsuro OKUYAMA
and Shigetoshi OHSHIMA

Faculty of Engineering, Yamagata University, 4-3-16, Johnan, Yonezawa 992
[†]Furukawa Electric Co. Ltd. 500, Kiyotaki, Nikko 321-14

The critical current of superconducting Y–Ba–Cu–O (YBCO) compounds prepared by the chelating method was investigated. The chelating agents used for this study were iminodiacetic acid (IDA), nitrilotriacetic acid (NTA), hydroxyethylethylenediaminetriacetic acid (HEDTA), ethylenediaminetetraacetic acid (EDTA), diethylenetriaminepentaacetic acid (DTPA) and triethylenetetraminehexaacetic acid (TTHA). The precursor YBCO obtained from metal complexes heving large stability constants, such as HEDTA, EDTA, DTPA, and TTHA, had very fine and homogeneous particles. The critical current density of YBCO in a block of $1 \times 4 \times 15$ mm^3 which was sintered at $880 \sim 910°C$ for 24 h, and then annealed at $500°C$ in O_2 flow was estimated to be 500 A/cm^2 at 77 K in zero applied magnetic field.

KEYWORDS: superconductor, critical current density, Y–Ba–Cu–O, evaluation, chelating method

Microstructure and Superconductivity in Bi–Sr–Ca–Cu–O System Doped with Pb and Sb

Qinlun Xu, Zhaojia Chen[†], Guangyao Meng
and Dingkun Peng

Department of Material Science and Engineering,
[†]*Department of Physics, University of Science and Technology of China,*
230026 Hefei, P.R. China

A series of samples $Bi_xPb_ySb_{0.1}Sr_2Ca_2Cu_zO_w$ has been produced by two methods. X-ray diffraction patterns revealed that there was a nearly single 2223 phase with a small amount of monoclinic phase in both two kinds of samples. The samples made by the oxalate coprecipitation technique had $T_{co} = 102$ K. The A.C. magnetic susceptibility showed only one sharp transition at 110 K. For samples prepared by a mixture of powders, the electrical resistance began to drop at 140 K, reaching zero at 92 K. Their A.C. magnetic susceptibility showed sharp transition at 135 K, and no transition at 110 K. The monoclinic particles were segregated on the surface of the samples. The intergrowth of 2223 and monoclinic phases at their boundaries caused the partial distortion of the 2223 phase. The distorted 2223 phase might be responsible for the 130 K superconductivity.

KEYWORDS: superconductivity, microstructure, intergrowth, distortion

pectroscopic Study on a Discharge Plasma of MOCVD Source Gases for High-T_c Superconducting Films

Hiroshi Harima, Hiroshi Ohnishi[†], Ken-ichi Hanaoka,
Kunihide Tachibana, Minoru Kobayashi[†] and Susumu Hoshinouchi[†]

Department of Electronics and Information Science,
Kyoto Institute of Technology Matsugasaki, Kyoto 606
[†]*Manufacturing Development Laboratory, Mitsubishi Electric Co.,*
Tsukaguchi, Amagasaki, Hyogo 661

Optical emission spectra from a glow-discharge plasma in the vapors of β-diketonate chelates of Ba, Y and Cu element have been measured. They show great changes depending on the temperature of the source-gas oven. In the case of $Ba(DPM)_2$, for example, intensity of the Ba^+ emission lines increases drastically at above 220°C, when compared to neutral lines. Referring to the data of thermal analysis and IR absorption experiment, this corresponds to the development of decomposition of the source material. The present experiment opens a future possibility of optical diagnostics to determine the optimum gas feeding condition in the preparation of high-T_c superconducting films by the MOCVD technique.

KEYWORDS: MOCVD, spectroscopy, plasma, IR absorption, superconductor, thin film, $Ba(DPM)_2$, $Y(DPM)_3$, $Cu(DPM)_2$

Influence of Deposition Parameters on Laser Damage Threshold of 355-nm Scandium Oxide-Magnesium Fluoride High-Reflector Coatings

Shigeharu Tamura, Saburo Kimura, Yoshiyuki Sato,
Shinji Motokoshi[†], Hidetsugu Yoshida[†] and Kunio Yoshida[†]

Government Industrial Research Institute, Osaka, Ikeda, Osaka 563
[†]*Institute of Laser Engineering, Osaka University, Suita, Osaka 565*

The experimental results of the laser-induced damage thresholds of Sc_2O_3/MgF_2 high-reflector (HR) coatings for an UV (355-nm, 0.4-ns) pulsed laser have been shown. The deposition parameters have been optimized by use of 5-layer semitransparent coatings, with the distribution of the standing-wave electric-field being similar to that of the HR coatings. For the 5-layer coatings, their threshold values were found to depend on the deposition parameters and the absorption; the coatings with low absorption had high damage threshold. Based on these results, the HR coatings were fabricated on fused silica, BK7 and sapphire substrates, and their thresholds have been measured. The highest average threshold on each substrate have been 3.5, 4.2 and 3.8 J/cm^2, respectively.

KEYWORDS: high-reflector coating, laser-induced damage, damage threshold, optical coating, dielectric multilayer, absoption

Luminescence and Energy Levels of Mn^{2+} in $LnMB_5O_{10}$ (Ln=La, Gd and Y; M=Mg, Zn and Cd)

R. Jagannathan, S. P. Manoharan, R. P. Rao
and T. R. N. Kutty[†]

Central Electrochemical Research Institute, Karaikudi-623 006, India
[†]*Indian Institute of Science, Bangalore-560 012, India*

Luminescence of Bi^{3+} or/and Mn^{2+} in $LnMB_5O_{10}$ system of phosphor has been studied. Bi^{3+} in $LnMB_5O_{10}$ leads to two types of emissions, viz. emission due to (i) Bi^{3+} isolated centres and (ii) Bi^{3+} clusters. In $LaMB_5O_{10}$, Bi^{3+} emission can cover longer distances (25 Å) for resonant transfer. In $LaMgB_5O_{10}$, replacement of Mg by Cd or Zn leads to considerable enhancement in Mn^{2+} emission intensity. In the case of $GdMB_5O_{10}$ system, this substitution leads to significant increase in $Gd^{3+} \rightarrow Mn^{2+}$ energy transfer rate. Energy levels of Mn^{2+} in $LaMB_5O_{10}$ and crystal field parameters (for the case of cubic field) have been calculated and the results based on these are discussed.

KEYWORDS: phosphor, pentaborates, luminescence, energy levels

Optical Properties of CdS Microcrystallite-Doped
SiO₂ Glass Thin Films

Ichiro TANAHASHI, Ayumu TSUJIMURA, Tsuneo MITSUYU
and Atsushi NISHINO[†]

Central Research Laboratories, Matsushita Electric Industrial Co., Ltd.
Yagumo-Nakamachi, Moriguchi, Osaka 570
[†]Living System Research Center, Matsushita Electric Industrial Co., Ltd.
Yagumo-Nakamachi, Moriguchi, Osaka 570

The optical properties of SiO_2 glass thin films containing CdS microcrystallites have been investigated. The thin films were deposited onto SiO_2 and GaAs substrates using an rf-sputtering technique. X-ray photoelectron spectroscopy and X-ray diffraction measurement indicated that the Cd and S atoms were doped as CdS with a hexagonal system in SiO_2 glass matrixes. In the optical absorption spectra, the absorption edge of the films with 18.5 at% of CdS clearly exhibited a blue shift by about 0.13 eV in comparison with that of the bulk CdS. In accordance with this result, the photolumines-cence spectra of the films exhibited a blue band-edge emission at a higher energy than that of the bulk CdS. The shift to higher energy seems to be a low-dimensional quantum size effect due to confinement of electrons and holes in CdS microcrystallites.

KEYWORDS: semiconductor-doped glass thin films, quantum size effect, optical absorption spectrum, photolu-minescence spectrum

Water Vapor Effects on Titanium Diffusion
into LiNbO₃ Substrates

Toshinori NOZAWA, Hiroshi MIYAZAWA and Shintaro MIYAZAWA[†]

Nippon Telegraph and Telephone Corporation, NTT Opto-electronics Laboratories
[†]NTT LSI Laboratories, 3-1, Morinosato Wakamiya, Atsugi-shi, Kanagawa 243-01

This paper describes experimental studies on titanium diffusion into Z-cut $LiNbO_3$ substrates as a function of water vapor content in the diffusion atmosphere of oxygen and argon. $LiNbO_3$ crystal characteristics were found to depend mainly on water vapor content, while Ti-diffusion characteristics were found to be affected not only by water vapor con-tent but also by the type of carrier gas. This study has important implications for the successful fabrication of Ti-diffused $LiNbO_3$ waveguides; for oxygen carrier gas, a small amount of water vapor should be introduced, while for argon carrier gas, a medium amount of water vapor should be introduced.

KEYWORDS: lithium niobate, diffusion, titanium, water vapor, optical device

Neutral-Beam-Assisted Etching of SiO₂
—A Charge-Free Etching Process—

Tatsumi MIZUTANI and Takashi YUNOGAMI

Central Research Laboratory, Hitachi Ltd. Kokubunji, Tokyo 185

Highly directional and low-damage dry etching of SiO_2 is realized by neutral-beam-assisted etching reactions. In this et-ching, low-energy neutral beams and neutral radicals are simultaneously supplied to the specimen, and the etching reac-tions are enhanced by the neutral beam bombardment. Low-energy (500 eV or less) Ar° neutral beams are generated from Ar^+ ion beams by charge exchange reactions. Neutral radicals are generated in a microwave plasma of CHF_3. The specimen surface is subjected only to these electrically neutral particles by eliminating charged particles with the retar-ding grids. The neutral-beam-assisted etching enables deep submicron pattern delineation without any serious radiation damage such as dielectric breakdown. It is a promising substitute for the current plasma etching as a future low-damage etching process.

KEYWORDS: neutral beam, low damage, etching, radical, plasma etching, radiation damage, dielectric breakdown, charge exchange

Roles of Ions and Radicals in Silicon Oxide Etching

Naokatsu IKEGAMI, Nobuo OZAWA, Yasuhiro MIYAKAWA,
Mamoru KONISHI and Jun KANAMORI

VLSI R & D Center, Electronic Devices Group, OKI Electric Industry Co., Ltd.
550-1, Higashiasakawa, Hachioji, Tokyo 193

Thermally stimulated desorption and X-ray photoelectron spectroscopy were used to study the adsorptive condition of reactive-ion-etched SiO_2 and PSG surfaces. Its relationship to the different reactivity between SiO_2 and PSG under the condition of highly polymerized fluorocarbon plasma was discussed. The reaction process of radicals under the thermal-ly excited condition was also investigated in a microwave-excited downstream reactor. The C, F molecules which covered the oxide surfaces as etching species during RIE were found to be chemisorbed, and as residues, they were adsorbed weakly. It was also found that oxygen atoms have the effect of decreasing the activation energy of the spontaneous reac-tion with the oxide surfaces in the fluorocarbon plasma.

KEYWORDS: TSD, XPS, fluorocarbon plasma, adsorptive condition, chemisorption, reactive ion etching, microwave excitation, downstream etching, activation energy

Low-Temperature Deposition of Hydrogen-Free Silicon Oxynitride without Stress by the Remote Plasma Technique

Takashi FUYUKI, Takashi SAITOH and Hiroyuki MATSUNAMI

Department of Electrical Engineering, Kyoto University,
Yoshidahonmachi, Sakyo, Kyoto 606

Hydrogen-free silicon oxynitride was deposited at 300°C through the reaction of Si from a solid source and neutral oxygen and nitrogen species activated in remote ECR plasma. The IR absorption measurement clearly showed that the composition of oxygen and nitrogen in the film was controlled by simply varying the flow ratio of the source gases of O_2 and N_2. Oxynitride films without internal stress could be realized by adjusting the film composition of oxygen and nitrogen. The deposited film had high resistivity and breakdown field, and the interface state density between the film and Si was in the lower range of 10^{10} cm^{-2}eV^{-1}, which were sufficient for device application.

KEYWORDS: silicon oxynitride, remote plasma

Ion Bombardment Enhanced Etching for Bi–Ca–Sr–Cu–O High-T_c Superconducting Thin Films

Shuji FUJIWARA, Ryokan YUASA, Kazuaki SHIKICHI,
Yuh MATSUTA, Masao NAKAO and Shigeo SUZUKI

Tsukuba Research Center, SANYO Electric Co., Ltd. 2-1 Koyadai, Tsukuba, Ibaraki 305

Ion bombardment enhanced etching (IBEE) has been first applied to Bi–Ca–Sr–Cu–O (BCSCO) high-T_c superconducting thin films. It was found out that the damaged region formed by the ion irradiation with a 200 keV Si^{++} focused ion beam was selectively dissolved in 1 normal KOH solution. The IBEE process resolves 0.1 μm patterns in the BCSCO films. Other strong alkaline solutions such as NaOH solution were also effective for the selective etching of the BCSCO films, but acid solutions did not give an enhanced etch rate at the irradiated region. The KOH treatment gave no effect on T_c of the BCSCO film. Bridge structures with the width of 1.5 μm were successfully fabricated with little degradation in T_c.

KEYWORDS: high-T_c superconducting thin film, Bi–Ca–Sr–Cu–O system, microfabrication, alkaline solutions, focused ion beam, ion bombardment enhanced etching

Oriented Structure and Superconducting Properties in Dense $Y_1Ba_2Cu_3$ Oxides Prepared by Press Forging

Kunio MATSUZAKI, Akishisa INOUE and Tsuyoshi MASUMOTO

Institute for Materials Research, Tohoku University, 2-1-1 Katahira Aobaku, Sendai 980

Dense $Y_1Ba_2Cu_3$ oxides with a highly oriented structure were prepared by press forging at temperatures above 1248 K in air. The c plane of the oxides is preferentially oriented perpendicular to the pressing direction, and the orientation factor (F) and density attained by press forging at 1273 K are 0.58 and 6.19 Mg/m^3, respectively. Subsequent annealing treatment for 36 h at 1173 K and for 200 h at 773 K in O_2 for the press forged oxides causes a high-T_c superconductivity with T_c of 90 K and J_c of 800 A/cm^2 at 77 K in zero field. The J_c value seems to be attributed to the highly oriented and densified structure.

KEYWORDS: $Y_1Ba_2Cu_3$ oxide, grain orientation, densification, press forging method, hot-working, high-T_c superconductor

Fracture Toughness of YBaCuO Prepared by MPMG Process

Hiroyuki FUJIMOTO, Masato MURAKAMI, Terutsugu OYAMA,
Yuh SHIOHARA, Naoki KOSHIZUKA and Shoji TANAKA

Superconductivity Research Laboratory, ISTEC, 1-10-13 Shinonome, Koto-ku, Tokyo 135

The fracture toughness of melt-powder-melt-growth(MPMG)-processed YBaCuO samples was measured and the beneficial effect of the dispersed 211 particles in the 123 superconducting phase on toughening the material was confirmed. Preferred fracture planes were (100), (010) and (001) planes, and the fracture toughness of the (001) plane was lower than that of the (100) and (010) planes.

KEYWORDS: superconductors, YBaCuO, fracture toughness, melt process

Crystal Structure of (Pb/Cu)SrLaCuO$_y$ Superconductor

Seiji ADACHI, Kentaro SETSUNE and Kiyotaka WASA

Central Research Laboratories, Matsushita Electric Industrial Co., Ltd.,
3-15 Yagumo-Nakamachi, Moriguchi, Osaka 570

The crystal structure of a new superconducting lead cuprate, (Pb/Cu)SrLaCuO$_y$, has been investigated. The Rietveld refinement for powder X-ray diffraction data of a ceramic sample was performed. It revealed that the structure is composed of (Pb/Cu)-O single layers and Cu-O$_6$ octahedrons. The properties of block layers between the apexes of two Cu-O$_6$ octahedrons in p-type cuprate superconductors are discussed.

KEYWORDS: oxide superconductor, high-T_c superconductor, lead cuprate, crystal structure, block layer, powder X-ray diffraction, Rietveld analysis

Nonstoichiometry and Mixed Pr Valency in $(Pr_{1-x}Sr_x)(Pr_{1-y}Ce_y)CuO_{4-z}$

Hijiri KITO, Hiroshi SAWA, Jun AKIMITSU,
Fujio IZUMI[†], Tōru ISHIGAKI[††] and Hajime ASANO[††]

Department of Physics, Aoyama-Gakuin University, 6-16-1 Chitosedai, Setagaya, Tokyo 157
[†]National Institute for Research in Inorganic Materials, 1-1 Namiki, Tsukuba, Ibaraki 305
[††]Institute of Materials Science, University of Tsukuba,
Tennodai, Tsukuba, Ibaraki 305

The structural parameters of a nonsuperconductor $(Pr_{0.6}Sr_{0.4})(Pr_{0.75}Ce_{0.25})CuO_{4-z}$ ($z=0.012$) were refined by the Rietveld analysis of TOF neutron powder diffraction data. It is isomorphous with a superconductor $(Nd_{1-x}Sr_x)$ $(Nd_{1-y}Ce_y)CuO_{4-z}$ and consists of K_2NiF_4- and Nd_2CuO_4-type units stacked alternately along the c-axis. An apical oxygen site in the K_2NiF_4 unit is 1.2% deficient. Pr atoms in the Nd_2CuO_4 unit are, at least partially, in the oxidation state +4. The origin of nonsuperconductivity in this compound is discussed from a crystal chemical point of view.

KEYWORDS: $(Pr_{1-x}Sr_x)(Pr_{1-y}Ce_y)CuO_{4-z}$, Rietveld analysis, neutron powder diffraction, mixed valency, nonstoichiometry

Single-Crystal Growth of $(LaSmSr)_2CuO_4$

Kunihiko OKA, Hiromi UNOKI, Kunihiko HAYASHI,
Yoshikazu NISHIHARA and Yasuo TAKEDA[†]

Electrotechnical Laboratory, Umezono 1-1-4, Tsukuba, Ibaraki 305
[†]Department of Chemistry, Faculty of Engineering, Mie University, 1515, Tsu, Mie 514

A superconducting crystal of $(LaSmSr)_2CuO_4$ with T*-phase structure has been grown by the travelling-solvent floating-zone (TSFZ) method. A phase diagram between $La_{0.8}Sm_{1.0}Sr_{0.2}CuO_4$ and CuO was produced to determine the constituent of the solvent. Single crystals with a maximum size of $3 \times 3 \times 6$ mm were obtained, which were annealed in a high-pressure oxygen atmosphere and exhibited superconductivity at about 17 K.

KEYWORDS: $(LaSmSr)_2CuO_4$, superconductivity, travelling-solvent floating-zone method

Effect of High-Energy Ion Irradiation on Current-Voltage Characteristics in the Oxide Superconductor $YBa_2Cu_3O_{7-x}$

Akihiro IWASE, Norio MASAKI, Tadao IWATA
and Takeshi NIHIRA[†]

Department of Physics, Japan Atomic Energy Research Institute,
Tokai-mura, Naka-gun, Ibaraki 319-11
[†]Faculty of Engineering, Ibaraki University, Hitachi, Ibaraki 316

The effect of 120 MeV ^{16}O ion irradiation on the current-voltage (I–V) characteristics in $YBa_2Cu_3O_{7-x}$ is examined at 77.3 K. Both the I–V characteristics and the dependence of V on the ion fluence Φ are found to show similar power-law behaviors in the form of $V \propto I^a$ for small current and $V \propto \Phi^b$, respectively. The experimental result is discussed in terms of current-induced unbinding of thermally excited vortex pairs.

KEYWORDS: $YBa_2Cu_3O_{7-x}$, I–V characteristics, 120 MeV O ion irradiation, unbinding of thermally excited vortex pairs

Properties of $Tl_2Ba_2Ca_2Cu_3O_x$ Thin Films with a Critical Temperature of 122 K Prepared by Excimer Laser Ablation

Toshihide NABATAME, Yukio SAITO, Katsuzo AIHARA,
Tomoichi KAMO and Shin-Pei MATSUDA

Hitachi Research Laboratory, Hitachi Ltd. 4026 Kuji-cho, Hitachi, Ibaraki 317

Superconducting thin films with a single $Tl_2Ba_2Ca_2Cu_3O_x(2223)$ phase were fabricated on MgO(100) substrates using excimer laser ablation and post annealing. The films had a highly c-axis-oriented structure and showed zero resistance at 122 K. Diamagnetism also appeared at 122 K and a 95% transition was achieved at 110 K. The critical current density of the film at 77 K was 1.5×10^5 A/cm^2 at 0 T.

KEYWORDS: $Tl_2Ba_2Ca_2Cu_3O_x$, thin film, excimer laser ablation, $T_c=122$ K, $J_c=1.5 \times 10^5$ A/cm^2 (77 K, 0 T)

$(11n)$-Oriented BiSrCaCuO Thin Film Formed on $SrTiO_3(110)$ Substrate by RF Magnetron Sputtering

Ken'ichi KURODA, Kazuyoshi KOJIMA, Osamu WADA[†],
Masami TANIOKU, Kazuo YOKOYAMA[†] and Koichi HAMANAKA

Central Research Laboratory, Mitsubishi Electric Corporation, Tsukaguchi-Honmachi, Amagasaki 661
[†]Materials and Electronic Devices Laboratory, Mitsubishi Electric Corporation,
Tsukaguchi-Honmachi, Amagasaki 661

A superconducting BiSrCaCuO thin film was grown on a $SrTiO_3(110)$ substrate at 660°C by sputtering a single target. The RHEED observation showed that the c-axis of the film meets at an angle of about 42° with the substrate surface. The XRD measurement showed that the film has a main peak at $2\theta=31.2°$. From these results, the film is considered to chiefly consist of a 2212 phase with (117) orientation and/or a 2212/2223 superlattice phase with (118) orientation. The film surface has a stripelike texture which probably corresponds to the film orientation. The zero-resistivity temperature of the film was lower by 20 K than that of the film formed on the $SrTiO_3(100)$ substrate.

KEYWORDS: BiSrCaCuO, superconductor, thin films, sputtering, preferential orientation, crystal structure, RHEED, XRD

The Influences of Ag Addition on Superconducting Properties and Tensile Strength for Bi–Sr–Ca–Cu–O Fibers Prepared by Pyrolysis of Organic Acid Salts

Hiroyuki NASU, Masashi SHOYAMA and Kanichi KAMIYA

Department of Chemistry for Materials, Faculty of Engineering, Mie University, Tsu 514

The influences of Ag addition on superconducting properties and tensile strength for Bi–Sr–Ca–Cu–O fibers prepared from the mixture of organic acid salts and oxide powders were investigated. The value of T_c(end) of fibers considerably increased to 72 K from 58 K for fibers without Ag_2O addition and the tensile strength slightly increased. These results are attributed to Ag addition enabling the annealing to 840°C.

KEYWORDS: superconducting fibers, Bi–Sr–Cu–Ca–O, T_c(end), tensile strength, Ag addition

Crystal Structure of a Pb-Based Copper Oxide $(Pb_{0.5}Cu_{0.5})(Sr_{1.1}La_{0.9})CuO_z$

Kiyotaka NAKAHIGASHI, Hiroyuki SASAKURA, Koji WATARI and Shinnosuke MINAMIGAWA

Department of Materials Science, University of Osaka Prefecture, Sakai, Osaka 591

The crystal structure of a Pb-based copper oxide superconductor $(Pb_{0.5}Cu_{0.5})(Sr_{1.1}La_{0.9})CuO_z$ (T_c=31.5 K) has been analyzed by the Rietveld method on the basis of the X-ray powder diffraction data. The material has a flat CuO_2 sheet and a flat (Pb/Cu)O sheet which were sandwiched between two zigzag (Sr/La)O sheets. The crystal has a tetragonal symmetry with a probable space group P4/mmm and its lattice parameters are a=3.7685(6) Å and c=8.6972(6) Å. The Cu atom on the CuO_2 sheet has sixfold octahedral coordination with the apexes reduced by about 3% along the c-axis.

KEYWORDS: crystal structure, superconductor, Pb–Sr–La–Cu–O system, X-ray diffraction, Rietveld method, $(Pb_{0.5}Cu_{0.5})(Sr_{1.1}La_{0.9})CuO_z$

Photo-CVD of Al_2O_3 Thin Films

Junji SARAIE and Sin-fat NGAN

*Department of Electronics and Information Science, Faculty of Engineering and Design,
Kyoto Institute of Technology, Matsugasaki, Sakyoku, Kyoto 606*

Al_2O_3 thin films have been prepared by photo-CVD under oxygen atmosphere for the first time using aluminum-tri-isopropoxide as a source material. The light source was a low-pressure Hg lamp. Without UV irradiation the deposition rate had a maximum at a particular oxygen-flow rate, which suggests the Langmuir-Hinshelwood surface-reaction mechanism. With UV irradiation, the deposition rate increased largely at a substrate temperature of less than 300°C. The activation energy of deposition reaction was as small as 1.5 kcal/mol. It was confirmed that the 185-nm light played an important role in the photodeposition. The dielectric dissipation factor (tan δ) decreased in the samples prepared by photo-CVD, especially at a low substrate temperature of less than 300°C; that is, the film quality was improved by photo-CVD.

KEYWORDS: Al_2O_3 thin films, photo-CVD, oxygen atmosphere, Hg-lamp light source, dielectric dissipation factor

Surface-treatment of the Ceramic Powders through Pulverization in a Reactive Atmosphere by Means of Ball Mill(2)
— Pulverization of Al_2O_3 in a Reactive Atmosphere by Means of Ball Mill —

Hiroshi UTSUGI[†], Atsushi ENDO[†], Noboru SUZUKI[†]
Yutaka GO[†] and Noriyuki BABA[†]

Al_2O_3 powder pulverized by a ball mill in an n-hexane, n-hexane solution of cetanol and octadecyltriethoxysilane was investigated using its dispersive property in water, its preferable dispersive property in immiscible mixed dispersive medium such as n-hexane and water, and using its carbon content, surface area, infrared spectra and pyrolysis. The following were recognized (1) Al_2O_3 pulverized in an n-hexane solution of cetanol after 8 hrs. was found to be more hydrophobic than that of unpulverized Al_2O_3 or Al_2O_3 after pulverization in an n-hexane. This is because the former dispersed in water, but dispersed in n-hexane for a mixed dispersive medium, n-hexane and water. Al_2O_3 pulverized in an n-hexane solution of octadecyltriethoxysilane after 32 hrs. or longer was shown to be hydrophobic; (2) From their infrared spectra and pyrolysis curves, the hydrophilic, but partially hydrophobic nature of the former was confirmed to be due to the surface cetoxy group and equi-molar hydroxyl group which was formed instantaneously. Also the surface property of the latter would be caused by the formation of an octadecyldiethoxysilyl group and an ethoxy group; (3) Accordingly, it was found that effective surface-treatment had been performed by pulverization in a reactive atmosphere.

Key Words : Pulverization in Reactive Atmosphere, Ball Mill, Alumina

Dielectric Properties of Ceramic Hydroxyapatite and Halogen-Substituted Apatite Solid Solutions

Kimihiro YAMASHITA, Hideo NAGASAWA, Takao UMEGAKI and Takafumi KANAZAWA
(Department of Industrial Chemistry, Faculty of Technology, Tokyo Metropolitan University,
Fukasawa 2-1-1, Setagaya-ku, Tokyo 158)

Ceramics of hydroxyapatite and its halogen-substituted solid solutions were found to exhibit dielectric characteristics at temperatures below *ca.* 500°C. Their dielectric constants, ε, and dielectric losses, tan δ, were dependent on both the sintering processing and the concentration of the substitutive halide ions.

The values of ε of the HAp and (X, H)Ap (X=F, Cl) ceramics sintered by hot-pressing (15 MPa) under reduced atmosphere (*ca.* 10^{-2} Pa) was smaller than those of the specimens sintered under conventional conditions (1200°C, 4 h in the air), while the tan δ was much larger in the former ceramics than in the latter. The activation energy for dielectric behavior was experimentally estimated as 0.4 *eV* to 0.5 *eV*.

The effects of halide ions were also found so distinct that the specimens with the composition of [F]=40% to 50% exhibited the maximum ε and the minimum tan δ.

Based on those results, it seems that the effects of vacancies are as important as substitutive halide ions.

Key words: Apatite ceramics, Halogen apatites, Dielectric properties, Dehydration

Bending Strength and Hydration Resistance of Sintered Lime Fired above 1750°C

Mitsuru WAKAMATSU, Satoshi SHIMIZU, Nobuyuki TAKEUCHI, Minoru TAKAO,
Yuiti ICHIRAKU* and Yoshitoshi TAGO*
(Department of Chemistry and Materials Technology, Faculty of Engineering and Design,
Kyoto Institute of Technology, *Osaka Gas Co., Ltd.)

Natural lime produced from limestone was used as the raw material for the present study. Three kinds of the sintered lime were made. The first sample was molded by cold isostatic pressing (CIP) and then fired for 6 h at 1800°C (sample A). The second sample was molded by uni-axial dust pressing followed by CIP and the fired for 6 h at 1800°C (sample B). The third sample was molded by CIP and then fired for 10 h at 1750°C (sample C). Effect of the conditions of pressing and firing on the bending strength and hydration resistance of sintered lime was investigated. The following results were obtained:

(1) The bulk density for the sintered bodies was from 2.81 to 2.88 g/cm³. The apparent porosity of the sample C was smaller than the other samples.

(2) The mean bending strength for the bodies was from 79 to 81 MPa. The Weibull parameter (18.4) of the sample B was higher than the other samples.

(3) The weight gain of the sample C under a saturated water vapor pressure at 8°C was less than 5% after fifty days, while the other showed as much as 5% of gain only after twenty days under same conditions.

Key words: Lime, Cold isostatic pressing, Hydration resistance, Weibull parameter

Journal of
Robotics and Mechatronics
Vol.2 No.4 August 1990
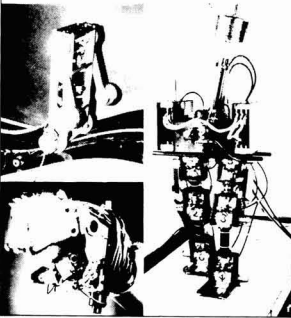
Special issue on Neural Networks